NTNU

Norwegian University of
Science and Technology

Shear strength of the rock-concrete interface at Kalhovd dam

Renate Musum Stangvik

Civil and Environmental Engineering
Submission date: June 2017
Supervisor: Leif Lia, IBM
Co-supervisor: Dipen Bista, NTNU/NORUT

Norwegian University of Science and Technology
Department of Civil and Environmental Engineering

NTNU
Norges teknisk-naturvitenskapelige universitet

Fakultet for ingeniørvitenskap og teknologi
Institutt for bygg- og miljøteknikk

MASTER THESIS

Student: ***RENATE MUSUM STANGVIK***

-

Title: SHEAR STRENGTH OF THE ROCK - CONCRETE INTERFACE AT KALHOVD DAM

1 BACKGROUND

Concrete dams are used for forming reservoirs for more than 300 years and still the mechanisms keeping them same are still not fully discovered. Research is still carried out for concrete dams and the current research is today mostly focused on ageing processes, shear resistance and refurbishing methods. Concrete dams for most research purposes divided into two groups; massive structures and light weight structures. The resistance against sliding is more significant for light weight structures and this thesis will focus on such structures.

Lightweight concrete dams like Ambursen dams (Platedam) and Buttress dams (Lamelldam) exposed to hydraulic pressure and ice loads require sufficient stability for safe operation during the lifetime. Global stability is normally considered as sliding stability and overturning. Criteria for sliding stability is continuously a research topic while new calculation tools and laboratory test methods are developed. Parallel research projects are currently ongoing in several institutions around Europe and many of those are coordinated through Stable Dams and other programs.

In the last two years the Research council funded program Stable Dams is hosted by NORUT in Narvik. In the program there are significant contribution in both state of the art review, laboratory tests, numerical modelling and field experiments. In this program several NTNU students have been involved so far where they are fully integrated in the research. In the winter 2017 a large laboratory test program will be carried out at COMPLAB at LTU in Luleå and this thesis work is integrated in this program.

2 MAIN ISSUES IN THE THESIS

Work to be done:

1. Review of models of shear failure. Analysis of such models by applying previous shear tests with respect to their capacity to address the roughness and direction of movement.
2. Evaluation of standard roughness profiles from existing criteria with models from 1 and comparison of the results.
3. Run an experimental test program hosted by the Stable Dams at LTU and compare the results with the estimated shear strength from different models.
4. Proposal of improvement to existing models.
5. Incorporate the results in the Kalhovd dam case.
6. Prepare a report.

The content may be adjusted during the work in accordance with the supervisors.

3 SUPERVISON, DATA AND INFORMATION

Main supervisor at NTNU will be Professor Leif Lia and the co-supervisor will be Dipen Bista, NROUT/NTNU. Further collaboration will be organized with LTU (Luleå), KTH (Stockholm), NORUT in Narvik and Statkraft.

The candidate is encouraged to search information through colleges and employees at NTNU, SINTEF, Energy Norway, NVE, consulting companies and other companies or organizations related to this topic. Contributions from other partners must always be referred in a legal way.

3 THESIS REPORT, FORMAT, REFERENCES AND DECLARATION

The report should be written with a text editing software, and figures, tables, photos etc. should be of good quality. The report should contain an executive summary, a table of content, a list of references and information about other relevant sources. The report should be submitted electronically in B5-format .pdf-file in DAIM within the date given in the master contract, and three paper copies would be handed in to the institute.

The executive summary should not exceed 450 words, and should be suitable for electronic reporting.

Trondheim 16. January 2017

_____

Leif Lia
Professor

Preface

This thesis has been written as a part of the final assessment of my 5-year Master´s degree at the department of Civil and Environmental Engineering at the Norwegian University of Science and Technology.

First of all, I would like to thank my supervisor Leif Lia for all his inspiring lectures that made me specialize in hydropower and concrete dams, and for all the good discussions and help with my master thesis this semester. A special thanks to my co-supervisor Dipen Bista for all the good discussions and feedback, for helping me with the shear tests and for motivating me through the semester.

I would also like to thank Gabriel Sas at NORUT/LTU for all the good supervision and for helping me with a finite element analysis of a buttress for my case study.

Additionally, I would like to express my gratitude to Thomas Forsberg at LTU for all the help with preparing the samples and conducting the shear tests, Kenneth Strand at Swerea Sicomp AB for scanning the samples and aligning the data clouds in a coordinate system, and to the program Stable Dams, hosted by NORUT, for the financial support.

Trondheim, 11th of June 2017

Renate Musum Stangvik

Abstract

The shear strength criteria Mohr-Coulomb is often used to calculate the shear capacity of rock-concrete interfaces due to its simplicity. However, the shear strength criterion does not consider all relevant aspects that contributes to shear strength in the rock-concrete interface, so it is believed that the criterion underestimates the shear capacity of concrete dams. Today, many concrete dams in Norway and the rest of the world do not fulfill the requirements to sliding stability. Dam owners are facing big investments to strengthening existing dams. Research on sliding stability of concrete dams is therefore still a hot topic. As new calculation tools and technology is developing, new shear strength criteria are developed.

The main objective of this thesis was to study the shear capacity of the rock-concrete interface at Kalhovd dam. In addition, existing shear strength criteria were analyzed with respect to their capacity to address relevant aspects that influence the shear capacity in rock-concrete interfaces. Four direct shear tests on drilled cores from Kalhovd dam was conducted to study the shear strength at the rock-concrete interface. The samples were scanned both before and after the shear tests with the optical scanner ATOS Compact Scan 5MP in order to calculate 3D roughness parameters that were needed as input parameters in several shear strength criteria. The obtained tests results were used to evaluate the accuracy of identified shear strength criteria. At last, a case study was performed to analyze the sliding stability of a buttress at Kalhovd dam based on the result from the shear tests and knowledge gained through this thesis.

The results from the shear tests on core samples from Kalhovd dam gave an average peak shear strength of 1.34 *MPa,* which corresponds to a peak friction angle of 69.5 °. Grasselli's shear strength criterion turned out to be best suited to estimate the peak shear strength of the conducted shear tests. Mohr-Coulomb's shear strength criterion underestimated the peak shear strength with more than 50 %, and was therefore the least suitable model due to high estimation errors. The sliding stability of a chosen buttress were analyzed with three different methods. When the factor of safety was calculated based on NVE's guidelines where the maximum allowable peak friction angle of 50 ° were used, the factor of safety was found to be 1.18, hence, the buttress is not considered stable. When assessing the sliding stability by using the peak friction angle obtained from shear tests or by using a combination of FE-analysis and shear test results, the factor of safety was found to be 2.57 and 2.96, respectively, and the buttress is considered stable.

Sammendrag

Skjærkapasiteten til grenseflaten mellom betong og fundament i betongdammer beregnes som oftest med skjærkriteriet Mohr-Coulomb på grunn av kriteriets enkle oppbygging. Det har imidlertid vist seg at kriteriet ikke fanger opp alle faktorer som bidrar til skjærkapasitet i grenseflaten. I dag finnes det flere betongdammer i Norge og resten av verden som ikke oppfyller kravene til glidestabilitet. Dameiere står dermed ovenfor store innvesteringer for å utbedre disse dammene, selv om det ikke er tegn til skader på dammen. Det er derfor stort fokus på forskning som omhandler glidestabiliteten til betongdammer. Etterhvert som nye beregningsverktøy og teknologi blir tilgjengelig, utvikles nye skjærkriterier.

Hensikten med denne oppgaven var å studere skjærkapasiteten til berg-betong grenseflaten til dam Kalhovd. I tillegg ble eksisterende skjærkriterier analysert med hensyn på kriterienes evne til å inkludere faktorer som påvirker skjærkapasiteten i berg-betong grenseflaten i betongdammer. Skjærforsøk med kjerneborprøver fra dam Kalhovd ble utført for å undersøke skjærstyrken i grensesnittet mellom fjell og betong. Prøvene ble skannet med en optisk skanner både før og etter skjærtestene, og resultatet fra skanningen ble brukt til å beregne 3D ruhetsparametere som ble brukt som inngangsparametere i flere av de eksisterende kriteriene. Noen av de identifiserte kriteriene ble brukt til å estimere skjærkapasiteten til prøvene, og testresultatene ble brukt til å vurdere nøyaktigheten av dem. Til slutt ble det gjennomført en casestudie der glidestabiliteten til utvalgt pilar ved dam Kalhovd ble analysert basert på testresultatene og kunnskap som ble opparbeidet i løpet av oppgaven.

Gjennomsnittlig skjærkapasitet til prøvene ble målt til 1,34 *MPa*, noe som tilsvarer en friksjonsvinkel på 69,5 grader. Grasselli's kriterium viste seg å være best egnet til å estimere skjærkapasiteten til prøvene. Mohr-Coulomb-kriteriet underestimerte skjærkapasiteten til prøvene med mer enn 50 %, og var derfor minst egnet til å estimere skjærkapasiteten på grunn av de store variasjonene mellom estimert og målt verdi. Glidestabiliteten til en utvalgt pilar ble analysert ved bruk av tre forskjellige metoder. Når sikkerhetsfaktoren ble beregnet på grunnlag av NVEs retningslinjer der høyeste tillatte friksjonsvinkel på 50 ° ble benyttet, ble sikkerhetsfaktoren beregnet til å være 1,18, og pilaren blir ikke ansett som stabil. Når glidestabiliteten ble analysert på grunnlag av testresultatene eller ved en kombinasjon av elementmetode og testresultat, ble sikkerhetsfaktoren beregnet til å være henholdsvis 2,57 og 2,96, og pilaren vil da anses som stabil.

Symbols and notifications

Roman letters

Symbol	*Description*
A	area of the sliding plane (m^2)
A_0	maximum potential contact area ratio (m^2)
A_{θ^*}	total potential contact area (m^2)
A_s	surface area where the asperities are sheared off (m^2)
c	cohesion (MPa)
c_i	internal cohesion of intact rock (MPa)
C	roughness parameter
C_m	maximum contact coefficient
E_{ave}	average estimation error (%)
FS	factor of safety
H	horizontal force (N) / Hurst exponent
h_{asp}	asperity height (m)
i	inclination angle of asperity/dilation angle (°)
i_g	dilation angle at grain scale (°)
JCS	joint compressive strength
JRC	joint roughness coefficient
$JRC_{,G}$	joint roughness coefficient calculated with Grasselli's expression
L_{asp}	asperity base length (m)
L_n	length of rock block in-situ (m)
L_0	length of the sample size in lab (m)
M_{stab}	stabilizing moment (Nm)
M_{over}	overturning moment (Nm)
N	normal load (N)
R	resistance/capacity (N)
S	applied load (N) / total shear force (N)
$S1$	component due to external work done in dilating against external force (N)
$S2$	component due to additional work in friction due to dilatancy (N)
$S3$	shear force for flat rough surfaces with no irregularities (N)

$S4$	shear force when all asperities are sheared off at the base (N)
T	resistance (N)
t	shear direction vector
V'	effective vertical force (N)
$tan^{-1}(Z_{2r})$	revised root-mean-square of the asperity angle (°)

Greek letters

Symbol	*Description*
α	inclination of the sliding plane (°) / azimuth angle (°)
β	the angle between schistosity plane the plane normal to the joint (°)
ϕ	friction angle (°)
ϕ_b	basic friction angle (°)
$\phi_{b,r\text{-}c}$	basic friction angle for rock-concrete interface (°)
ϕ_i	friction angle of intact rock / friction angle for well bonded contacts (°)
ϕ_r	residual friction angle (°)
ϕ_s	friction angle for unbonded contacts (°)
$\Delta\phi$	joint roughness angle (°)
η	the degree of interlocking / the ratio unbonded portion to total area
μ	coefficient of friction / mean value
μ_{max}	maximum allowable coefficient of friction
θ^*	apparent dip angle (°)
θ^*_{max}	maximum apparent dip angle (°)
σ_n	effective normal stress (MPa)
σ_c	compressive strength of intact rock(MPa)
σ_t	tensile strength of intact rock (MPa)
ρ_n	median angle pressure (MPa)
τ	shear stress (MPa)
τ_p	peak shear capacity (MPa)
$\dot{\upsilon}$	the rate of dilation at failure

Table of content

1 Introduction

1.1 Background

In Norway, there exists a big number of concrete dams related to hydro power. Due to the hydrostatical water pressure and uplifting forces, the dams can experience failure. There are three different failure modes for stability analysis described in literature; sliding failure, overturning failure and overstressing. These three failure modes are assumed to occur independently, but in a real case, it will most likely be a combination of these three failure modes (Fishman, 2009). The fact that these failure modes interact with each other, makes stability analysis a complex process. Concrete dams can be divided into two groups; massive structures and light weight structures. The resistance against sliding is more significant for light weight concrete dams like Ambursen dams, and this thesis will focus on such structures.

Today, numbers of light weight concrete dams do not fulfill the requirements for the safety factor against sliding stability given by the NVE´s guidelines. Dam owners are facing big investments to improve the dams so they fulfill the requirements for safety factor. Most of the dams have been standing for decades without any signs of sliding, so it is questioned if costly rehabilitations of all the dams is an unnecessary use of resources. The stability calculations are based on the well-known Mohr-Coulomb criterion, a criterion that may underestimate the shear capacity of concrete dams due to its simplicity.

The last decades, a lot of research on sliding stability for concrete dams have been carried out. As new calculation tools and technology is developing, new shear strength criteria are developed to consider more of the aspects that contribute to shear strength in concrete dams.
Stable Dams is a program hosted by NORUT, and the program is one of the research projects currently looking at shear strength in the foundation of concrete dams. The project is running a large laboratory test program at COMPLAB at LTU during the winter 2017, looking at both asperities in rock foundation and core samples from a dam site. The knowledge gained through this project will help engineers and dam owners to get a better understanding of the shear strength in concrete dams. This thesis will take part in the test program and conduct shear tests on core samples extracted from dam Kalhovd.

Dam Kalhovd is a 386 *m* long Ambursen dam owned by Statkraft in Norway. The dam does not fulfill the requirements for safety factor against sliding given by the Norwegian guidelines, and Statkraft are facing costly rehabilitations to get the dam "stable". The project Stable Dams has been involved in this dam to study the shear capacity of the dam, as it is believed that the dam is stable. The dam has been standing for almost 70 years without any signs of damages, and experts believes that there is no need to strengthen the dam.

1.2 Goal and objectives

The goal of this thesis is to study the shear capacity of the rock-concrete interface at Kalhovd dam, analyze existing shear strength models and evaluate how these models can be used to estimate the shear strength for concrete dams.

Objectives:

- Identify and review of existing models and their capacity to include properties that influence shear capacity.
- Perform shear tests on drilled cores from Kalhovd dam.
- Find and calculate three-dimensional roughness parameters based on surface scanning.
- Study the accuracy of different models by applying models on the test samples and compare the estimated shear strengths with the test results.
- Case study:
    - Calculate the factor of safety for one buttress at dam Kalhovd by using test results and the method proposed by NVE.

1.3 Method

- A literature study on sliding stability of concrete dams and existing shear strength criteria was conducted. The identified shear strength criteria were analyzed with respect to their capacity to address relevant aspects that influence the shear capacity in rock-concrete interfaces. The literature was found using Google Scholar and Oria, an online library from NTNU.

Keywords that were used when searching for literature online:
Shear strength · Concrete dams · Shear strength criterion · Sliding stability · Rock – concrete interface · Shear tests · 3D roughness · Grasselli

New literature was also found by following the references in the literature.

- Shear tests on core samples from the dam site at Kalhovd (rock-concrete interface) was conducted in laboratory. The samples were scanned and 3D roughness parameters were calculated based on surface scanning´s. The test results were compared with the estimated shear strengths from the analyzed models.

- Case study of Kalhovd dam: Sliding stability analysis of a chosen buttress were conducted with three different methods; a combination of finite element analysis and results from shear tests, by using the shear friction method as suggested by NVE along with the maximum allowable peak friction angle, and by using the shear friction method along with the peak friction angle obtained from the shear tests.

2 Sliding stability of concrete dams

Sliding of a dam occurs along the plane with lowest shear resistance. The failure can occur either in the concrete dam, in the interface between dam and foundation or in the foundation. The available shear strength in the concrete is normally known, as concrete is a man-made material where the mechanical properties can be controlled. The shear strength in the rock-concrete interface is more uncertain and mainly depending on the geometry of the interface and weather cohesive strength is present or not (Johansson, 2009). This thesis will focus on sliding in the rock-concrete interface.

In general, the stability analysis is based on a principle that the resistance or capacity, R, should be equal or greater than the applied load, S, to avoid sliding (Johansson, 2009). This is shown in Equation 1.

$$R \geq S \tag{1}$$

The most common way to express safety regarding sliding stability is with a factor of safety. The factor of safety, FS, is defined by dividing the resistance, R, with applied load, S, as shown in Equation 2.

$$FS = \frac{R}{S} \tag{2}$$

2.1 Methods used to analyze sliding stability

Several methods have been used to analyze the sliding stability over the last 100 years, Johansson (2009) presents the three most common methods; *the sliding resistance method, the shear friction method* and *the limit equilibrium method*.

2.1.1 The sliding resistance method

Johansson (2009) presents the sliding resistance method as the first criterion used to assess safety against sliding. The sliding resistance method calculates a coefficient of friction, μ, which is calculated by dividing the sum of horizontal forces, $\sum H$, by the sum of effective vertical forces normal to the sliding plane, $\sum V'$. To avoid sliding, the coefficient of friction,

should be smaller than the maximum allowable coefficient of friction, μ_{max}, as shown in Equation 3.

$$\mu = \frac{\Sigma H}{\Sigma V'} \leq \mu_{max} \tag{3}$$

2.1.2 The shear friction method

According to Nicholson (1983), *the shear friction method* was first presented by Henna in 1933. This method calculates a factor of safety based on the Mohr-Coulomb equation, which represents the shear capacity for a sliding plane (see subsection 3.1.1). By expressing the shear resistance by Mohr-Coulomb, the factor of safety, *FS*, can be expressed as shown in Equation 4.

$$FS = \frac{\dfrac{cA}{cos\alpha(1 - tan\phi \cdot tan\alpha)} + \Sigma V' \cdot \tan(\phi + \alpha)}{\Sigma H} \tag{4}$$

Where c is the cohesion of the sliding plane, A is the area of the sliding plane, ϕ is the friction angle, α is the inclination of the sliding plane along the horizontal plane, $\Sigma V'$ is the sum of the effective vertical forces and ΣH is the sum of the horizontal forces.

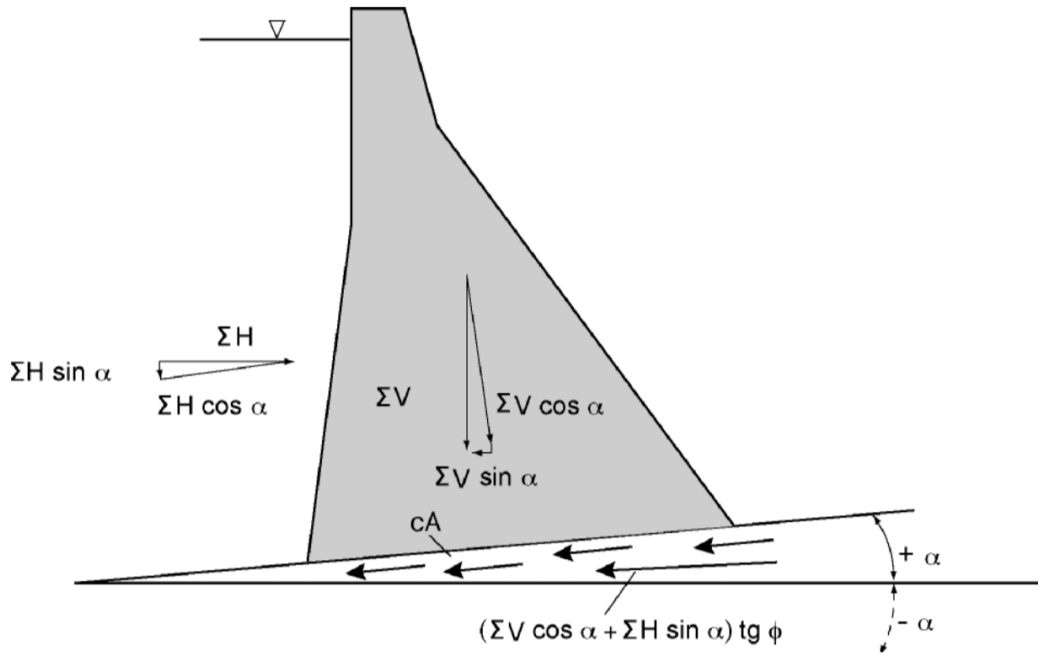

Figure 1: Sliding resistance at a sliding plane with angle α relative to the horizontal (NVE, 2005)

Equation 4 can be derived from Figure 1. If $\alpha = 0$ (horizontal sliding plane), the equation can be reduced to a simpler version as shown in Equation 5.

$$FS = \frac{cA + \Sigma V' \cdot \tan\phi}{\Sigma H} \tag{5}$$

2.1.3 The limit equilibrium method

The limit equilibrium method, presented by Nicholson (1983), defines the factor of safety, *FS,* against sliding as the relationship between maximum shear capacity, τ_p, and the shear stress required for equilibrium, τ, as shown in Equation 6.

$$FS = \frac{\tau_p}{\tau} \tag{6}$$

According to Nicholson (1983), there are some basic assumptions required to be fulfilled for this method to be valid.

1. The factor of safety is defined by Equation 6.
2. Impending failure occurs according to the requirements imposed by elastic-plastic failure theory.
3. The maximum shear strength that can be mobilized is adequately defined by the Mohr-Coulomb failure criteria.
4. Failure modes can be represented by two-dimensional, kinematically possible planes.
5. The factor of safety computed from the stability equations is the average factor of safety for the total potential failure surface.
6. To derive easy, simple-to-use equations, the vertical forces between wedges are assumed to be negligible.
7. The structural wedge must be defined by one wedge.

2.2 International regulations for sliding stability of concrete dams

There is no international standard for sliding stability analysis of concrete dams. How the sliding stability of concrete dams are analyzed, varies with country. In this section, the current guidelines for several countries, including Norway, are presented.

2.2.1 Norway

The Norwegian regulations for sliding stability analysis of concrete dams is controlled by the Norwegian Water Resources and Energy Directorate (NVE). The requirements regarding sliding stability of concrete dams can be found in *"Retningslinjer for betongdammer*" (NVE, 2005)

The factor of safety is used to assess if the dam is stable or not. The factor of safety is calculated by using the shear friction method presented in subsection 2.1.2. If the friction angles are not documented by tests, the following maximum values should be used:

- 50 ° for hard rocks, rough surfaces and favorable schistosity in the transition rock/concrete.
- 45 ° for hard rocks, small roughness and apparent schistosity and loos rocks without schistosity.
- 40 ° for loos rocks with clear schistosity.
- 45 ° for sliding planes in concrete.

Table 1 shows the minimum requirements for safety factor for the dam to be considered stable.

Table 1: Required factor of safety for sliding stability according to NVE

Loading combination	Minimum acceptable factor of safety		
	No cohesive strength	Cohesive strength from tests	Cohesive strength from literature
Design loads	$FS \geq 1.5$ (*$FS \geq 1.4$)	$FS \geq 2.5$	$FS \geq 3.0$
Accidental loads	$FS \geq 1.1$	$FS \geq 1.5$	$FS \geq 2$

*Applies for concrete dams where cracks will not increase the pore pressure (mainly Ambursen dams)

An additional control is required for concrete dams were rock bolts is included in the sliding stability analysis. The additional control is performed for the design flood water level and without the effect from rock bolts. The minimum requirements for factor of safety is then $FS \geq 1.1$ for both gravity dams and Ambursen dams.

2.2.2 Sweden

There are no official regulations concerning the sliding stability of concrete dams in Sweden, but Swedish dam owners who are members of Swedenergy AB (Svensk Energi) are committed to follow the guidelines "*RIDAS - Kraftföretagens riktlinjer for dammsäkerhet*", provided by Swedenergy AB (2012). Chapter 1-3 in the guideline was revised in 2016, and the rest of the guideline, including the chapter about stability for concrete dams, is currently under revision.

The sliding resistance method described in subsection 2.1.1 is used by the guideline to assess the sliding safety for concrete dams. The dam is considered stable if the calculated coefficient of friction is equal or less than the maximum allowable coefficient of friction, μ_{max}. The coefficient of friction is calculated for three load combinations:

- Normal loads (Highest regulated water level, HRWL, and ice pressure)
- Exceptional loads (Design flood water level)
- Accidental loads (Loads due to accidents, natural disasters, war and sabotage)

According to Swedenergy AB (2012) the horizontal ice load can be assumed to be 50-200 *kN/m,* depending on the geographic location. The contribution from cohesion is usually disregarded in sliding stability analysis in Sweden. The maximum allowable coefficient of friction for dams founded on rock with good quality is shown in Table 2.

Table 2: Maximum allowable coefficient of friction for dams in Sweden

Foundation type	Normal loads	Exceptional loads	Accidental loads
Rock	0.75	0.90	0.95

Sliding failure is assumed to occur when the coefficient of friction is 1.0, which equals a friction angle of 45 °. Minimum values for the factor of safety corresponding to the maximum allowable coefficient of frictions can be seen in Table 3.

Table 3: Minimum values for factor of safety according to the Swedish guidelines

Foundation type	Normal loads	Exceptional loads	Accidental loads
Rock	1.35	1.10	1.05

2.2.3 Canada

The Canadian Dam Association (CDA) developed the guideline, *"Dam Safety Guidelines"*, to assess the sliding stability of dams in Canada. No official regulations are developed in Canada, but the regulations of dams in Canada is a provincial/territorial responsibility. In provinces where no other restrictions are existing, the guidelines are used to assess the sliding stability (CDA, 2013).

CDA (2013) recommends assessing the sliding stability by calculating a factor of safety by using the shear friction method presented in subsection 2.1.2 Three load combinations are used in the analysis:

- Usual: Those who can be expected throughout much of the life of the facility and might also be defined as routine conditions.
- Unusual: Deviations from routine, including ice and debris blockage, seismic events or large floods.
- Extreme: Events that might lead to dam failure if actions is not taken and could include extreme floods, seismic events, failure of dam component, or equipment failure.

Minimum values for factor of safety recommended by CDA (2013) are found in Table 4.

Table 4: Minimum values for factor of safety according to (CDA, 2013)

Loading combination	Minimum acceptable factor of safety		
	No cohesive strength	Cohesive strength from tests	Cohesive strength from literature
Usual	$FS \geq 1.5$	$FS \geq 2.0$	$FS \geq 3.0$
Unusual	$FS \geq 1.3$	$FS \geq 1.5$	$FS \geq 2.0$
Extreme: Flood	$FS \geq 1.1$	$FS \geq 1.1$	$FS \geq 1.3$
Extreme: Earthquake	Used to establish post-earthquake condition of the dam		
Post-Earthquake	$FS \geq 1.1$	Note 1	

Note 1. Shear resistance based on friction and cohesion needs to be considered carefully, since the analysis surface may not remain in compression throughout the earthquake but may result in cracking, which will change resistance parameters.

2.2.4 USA

There are several agencies involved in dam safety in USA. The Federal Energy Regulatory Commission (FERC) has the largest dam safety program in USA, and it is therefore decided to present their guidelines presented in "*Engineering Guidelines for Evaluation of Hydropower Projects, Chapter III"(FERC, 2016)* in this thesis. Chapter III, Gravity Dams, consist of methods to analyze the sliding stability for gravity dams, which with minor changes also is valid for Ambursen dams.

The factor of safety is used to assess if the dam is stable or not. "The Shear Friction Factor of Safety" is calculated by using Equation 7:

$$FS = \frac{\tan(\phi_{actual})}{\tan(\phi_{required})} \tag{7}$$

Four different loading conditions is used when calculating the factor of safety:

- Usual loading – Normal operating condition
- Unusual loading – Flood Discharge Loading
- Unusual loading – Ice
- Extreme loading – Usual loading + Earthquake

Since it is hard to determine the cohesive strength in the interface of dams, FERC (2016) offers an alternative recommended factor of safety that can be used when cohesion is not considered. Recommended minimum factors for situations with and without cohesive forces are listed in Table 5.

Table 5: Recommended minimum values for factor of safety for dams in USA

Load condition	With cohesion		No cohesion
	High hazard potential	Low hazard potential	
Usual	$FS \geq 3.0$	$FS \geq 2.0$	$FS \geq 1.5$
Unusual	$FS \geq 2.0$	$FS \geq 1.25$	$FS \geq 1.3$
Post Earthquake	$FS \geq 1.3$	$FS \geq 1.0$	$FS \geq 1.3$

2.3 Factors influencing shear strength in rock-concrete interfaces

The shear capacity in the rock-concrete interface is important as it is essential to determine the sliding stability of a dam. There are several factors that influence the shear strength in rock-concrete interfaces. The shear strength of an interface is mainly coming from two main parts, bonding between the two surfaces and the surface roughness. If bonding is present, this will be mobilized first, and influence the shear strength significantly. If bonding is not present, the shear strength will mainly be determined by the surface roughness and topography in the interface. The following subsections presents the factors that can influence the results when estimating or testing the shear capacity of a rock-concrete interface.

2.3.1 Surface roughness

The surface roughness in the interface is an important factor when considering the shear capacity of a dam. Several authors (Liahagen, 2012, Colio Gutiérrez, 2013, Mouzannar, 2016) have found that an increased surface roughness in the interface gives a significant increase in shear capacity. The conclusions were based on several direct shear tests on rock-concrete samples with different degrees of surface roughness. Other research (Grasselli, 2001) has showed that the entire surface roughness must be considered when analyzing the shear strength, as not all of the total surface area are involved in shearing, and the contact area that contributes to shearing is scattered randomly. Since the contact area is scattered randomly, a linear surface profile will not capture all the contact area that contributes to shearing. Therefore, to capture all the surface roughness that contributes to shear capacity, the whole surface must be considered. A three-dimensional description of the surface is therefore preferable to a two-dimensional surface description.

2.3.2 Adhesive bond

When casting a concrete dam on a well-prepared rock surface, the interface will most likely be bonded. Several shear tests (Moradian et al., 2012, Liahagen, 2012, Tian et al., 2015) have showed that the bond strength increases the shear capacity of the dam significantly. If assuming that the bond is mobilized before the surface roughness for bonded interfaces, the bond will have to break before the surface roughness contributes to shear strength. The bond strength will most likely be stronger than the mobilized surface roughness, hence, the bond strength will determine the shear capacity for bonded rock-concrete interfaces.

However, it is hard to determine how much of the interface that is bonded, as the interface is not visible to inspect. A way to determine if bonding is present or not is to extract core samples from the dam and investigate the interface. There may be spatial variations in the bonding conditions in the interface, and a few core samples will not be enough to map the bonding conditions in the whole interface. Non-destructive mapping of the bonding is preferable, but no universal method to do this is developed yet.

2.3.3 Normal stress

The normal stress is important, as the shear capacity increases with increasing normal stress. In addition, the normal stress influence what failure mode that will occur for the asperities. If considering a unbonded interface with low normal stresses and low asperity inclinations, the govern failure mode will be sliding. For higher normal stresses and high asperity inclinations, the asperities will fail through shearing or tensile failure. The normal stress in the interface of a dam varies, with lowest normal stress occurring at the heel and the highest normal stress occurring at the toe of the dam. The shear strength of the interface will therefore vary through the cross section of the dam. As a result, the failure mode of asperities could be different through the dam. For low normal stresses, the asperities will slide over each other, and for higher normal stresses, the asperities can fail by tension failure or shearing at the base, resulting in a decrease in the amount of surface roughness. The influence from surface roughness on shear capacity will therefor decreases with increasing normal stress, as the asperities are sheared off or broken due to these high normal stresses. According to Grasselli (2001), breaking of asperities due to tensile failure is most likely to be the major failure mode for asperities under high normal stresses. This conclusion was based on observations of several surfaces of sheared rocks, where the failure plane tended to be rough, and intact fragments sheared from the roughness could be observed.

2.3.4 Shear direction

Shear tests have shown that different shearing directions on the same specimen results in different shear strengths (Ballivy et al., 2006, Grasselli, 2006). This is due to horizontally variations in the roughness (Ballivy et al., 2006) and the contribution in strength from roughness will therefore vary with different shear directions. Therefore, when considering the shear capacity of a concrete dam, it is not enough to map the entire surface roughness in the interface, the shear direction must also be specified.

2.3.5 Topography and location of big asperities

For many of the Ambursen dams in Norway, it is observed that there is a lot of variation in the topography at the interface. Often, there is one or several large asperities (1st order asperity) at the rock-concrete interface which will cause interlocking of the dam. These 1st order asperities will most likely influence the shear capacity of the interface to a large extent. How, and to what extent this will influence the shear capacity is uncertain, as there is not much research done on this topic. Today, the stabilizing effect from 1st order asperities are usually not considered when estimating the shear capacity of a dam, usually only the surface roughness (2nd order asperities) is considered, see Figure 2 for illustration.

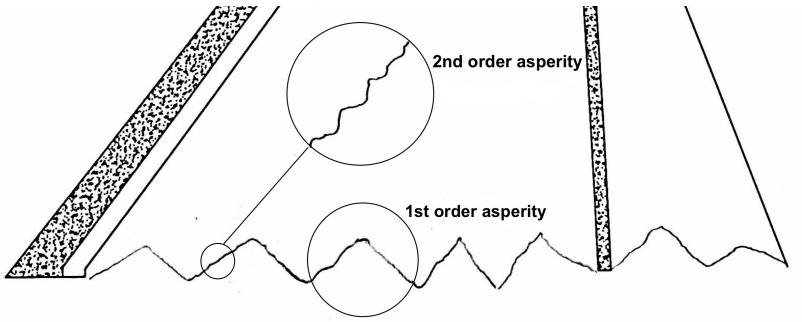

Figure 2: Illustration of 1st and 2nd order asperities at a dam foundation

The challenge is therefore to include the effect of the 1st order asperities found in the topography in shear strength calculations. The program Stable Dams conducted a series of shear test on rock-concrete specimens to study the effect of location on 1st order asperities. Shear tests conducted at LTU in 2017 by the program Stable Dams, studied how the location of these large asperities affects the shear capacity of the interface. The tests were carried out with pure shear in addition to a combination of shear and bending. For pure shear, the location of 1st order asperities had no effect on shear strength. However, for the shear tests conducted with a combination of shear and bending, the location of asperities affected the peak shear strength. In this case, the shear strength increased with increasing distance between the asperity and the front were the load was applied. The combination of shear and bending is illustrative for the forces acting on the interface of concrete dams. This means that the further away from the heel the asperity is located, the larger the peak shear strength will be.

In addition, the shear tests showed that the location of the asperities affects the failure path and which material that fails. For asperities located near the front (where the load is applied), the concrete casted on top of the asperity is most likely to fail. For 1st order asperities located near the back of the sample, the rock asperity is most likely to fail. The fact that the location of asperities in rock-concrete interfaces may affect if the failure path goes through rock or concrete, makes this a complex process. It can be hard to determine if the strength parameters from rock or concrete should be used in the models, as this may vary depending on if it is the rock or concrete that breaks. A conservative method would be to use the strength parameters for the weakest material, which in most cases are concrete.

2.3.6 Scale effects

When conducting shear tests, the size of the test sample may affect the test result. Therefore, the size of the sample should be considered carefully when results from shear tests are used to estimate the shear capacity of dams, as different sizes on the samples can result in different shear capacities. Earlier conducted shear tests on rock-concrete interfaces have shown that the shear capacity generally increases with decreasing size of the samples (Mouzannar, 2016). A large sample is more likely to include weak planes and joints compared to small samples. Therefore, samples tested at large scale is more likely to have lower shear strength compared to smaller samples, as illustrated in Figure 3.

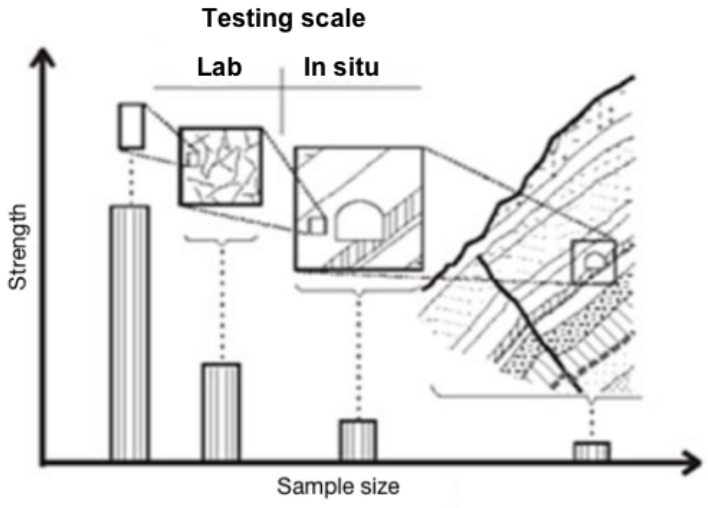

Figure 3: Scale effects illustrated by rock samples from a tunnel project (Nilsen, 2016)

Furthermore, when conducting shear tests in laboratory, the samples will be exposed to a moment when the load is applied. The moment will increase with decreasing sample size,

hence, small samples will be exposed to a bigger moment than larger samples. How this moment will affect the test results is not yet documented, but it is important to be aware of this. The scale effects should also be considered when determining input parameters for models based on extracted samples from a dam site, as it is not certain that a small sample will give values that is representative for the whole dam.

In the literature, contradictory results regarding the scale effects is presented. Both Johansson (2016) and Mouzannar (2016) studied the scale effects by conducting shear tests at different scales. Mouzannar (2016) conducted shear tests at rock-concrete interfaces at three different sizes; cored samples with a diameter of 80 *mm*, squared samples of 180 x 180 *mm* and rectangular surfaces of 1500 x 1000 *mm*. The conclusion was that there was no scale effect on residual strength, a negative effect on cohesion (decreasing strength with increasing scale) and a positive effect on the friction angle (increasing strength with increasing scale).

Johansson (2016) conducted shear tests on fresh, unweathered rock samples measuring 200 x 200 *mm* and 60 x 60 *mm*. No scale effects were observed for perfectly mated samples and samples with an initial displacement of 5 *mm*. According to Johansson (2016) it is unclear if the reported scale effects in literature is dependent on scale or a combination of scale and different degrees of matedness. The influence from scale and matedness could be a reason, but no conclusions were drawn since this study only consisted of two sample sizes.

It is hard to conclude weather there is scale effects or not with these contradictory results. Johansson (2016) observed no scale effects for samples with interfaces that is perfectly mated or have a small displacement of 5 *mm,* while Mouzannar (2016) observed scale effects on cohesion and friction angle. When casting concrete on top of rock, it is reasonable to assume that the interface is perfectly mated, hence, according to Johansson´s findings, no scale affects should be observed for the shear tests conducted by Mouzannar. However, as Johansson (2016) pointed out, no conclusions about the scale effect could be drawn as only two sizes were tested. In addition, Johansson conducted shear tests at unbonded rock joints, while Mouzannar conducted shear tests on bonded rock-concrete interfaces. This may be the reason why Johansson (2016) did not observe scale effects regarding the cohesive forces. As seen, there is still much uncertainty related to scale effects, and no conclusions can be drawn weather scale effects affect the shear strength or not, and if, to what extent.

3 Shear strength criteria

The last century, several criteria used to calculate the shear strength for sliding planes have been developed. The development of shear strength criteria, also called shear strength models, is important as a lot of dam owners are facing big investments to strengthening existing dams which do not fulfill the requirements given for safety factor against sliding. If some of these shear strength criteria can replace the old Mohr-Coulomb criteria, some of the dams may be considered stable according to the guidelines, thus, expensive rehabilitation may be avoided. In this chapter, existing shear strength criteria is presented.

3.1 Specific shear strength criteria

In this context, specific shear strength criteria mean shear strength criteria which do not incorporate the three-dimensional surface roughness.

3.1.1 Mohr-Coulomb

The Mohr-Coulomb criterion is based on the work by Coulomb 1776 and Mohr 1882 (Johansson, 2009). It was originally used by geotechnical engineers to calculate the shear capacity for soils, but has later been adopted to express the shear capacity of rock-concrete and rock-rock interfaces. The failure criterion calculates the shear capacity for a given joint/plane and can be expressed as shown in Equation 8.

$$\tau_p = c + \sigma_n \cdot tan\phi \tag{8}$$

Where τ_p is the shear capacity of the interface, c is the cohesion of the sliding plane, σ_n is the effective normal stress and ϕ is the friction angle of the failure plane.

It is difficult to measure values for cohesion, therefore, the values used in stability analysis are often back calculated from shear tests, taken from the literature or disregarded. The contribution from bonding, friction and roughness are not yet properly understood, but the Mohr-Coulomb criteria is still used in sliding analysis today due to its simplicity.

3.1.2 Patton's bilinear failure criterion (1966)

The Mohr-Coulomb criterion is only valid to represent the frictional behavior along a flat surface and it does not capture the fact that natural rock joints have roughness that contributes to the shear capacity. Patton (1966) was one of the first to consider the effect of the roughness on shear capacity, and made important contributions to the failure criterion. Patton conducted a series of shear tests on saw-tooth specimens to illustrate the contribution from roughness. The result was a bi-linear failure criterion. Under low effective normal stress, the shear capacity could be expressed as shown in Equation 9.

$$\tau_p = \sigma_n \cdot \tan(\phi_b + i) \tag{9}$$

Where τ_p is the shear capacity, σ_n is the effective normal stress, ϕ_b is the basic friction angle for a smooth, but rough surface and i is the inclination angle of the tooth. Patton observed that for a certain level of higher normal stress, the effect of the saw tooth asperities disappeared due to failure through the asperities by shearing. In this case, the expression of the shear capacity was changed to the following expression:

$$\tau_p = c_x + \sigma_n \cdot \tan(\phi_r) \tag{10}$$

Where ϕ_r is the residual friction angle of an initially intact material and c_x is the cohesion when the teeth are sheared of at their base. The principles of the failure envelope proposed by Patton is shown in Figure 4.

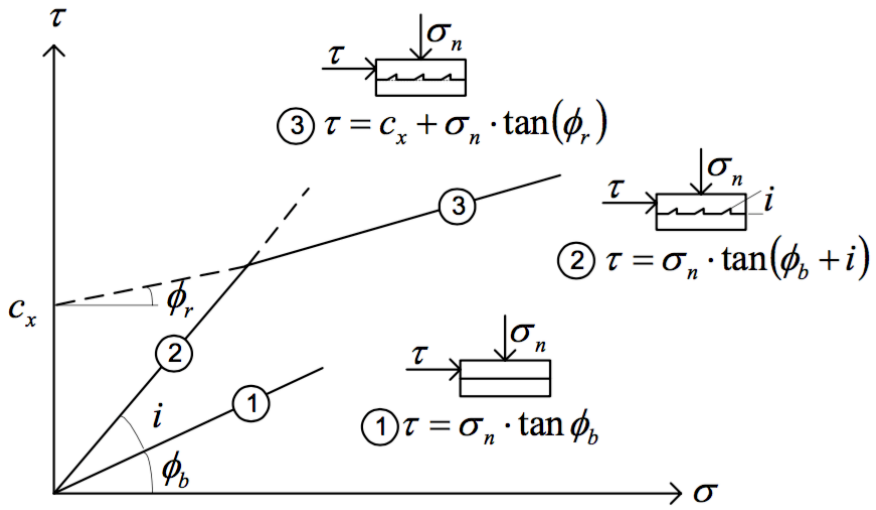

Figure 4: Bilinear failure envelope proposed by Patton (1996), (taken from Johansson (2009))

According to Grasselli (2001), the bilinear envelope developed by Patton shown in Figure 4, describes fairly well the shear strength for plane surfaces containing a number of regularly teeth with the same dimensions, but are not satisfying for irregular rock surfaces. However, Patton (1966) argued that the failure envelope for real rocks *"would not reflect a simple change in mode of failure but changes in the "intensities" of different failure modes of failure occurring simultaneously"* due to variations in size, inclinations, internal strengths and coefficients of frictions for asperities along the rock surface.

3.1.3 Ladanyi and Archambauly (1970)

As Patton's bilinear model could not describe the curved failure envelope for irregular surfaces, Ladanyi and Archambauly (1970) developed a new shear strength criterion based on energy considerations that is valid for irregular rock surfaces. If no shearing of the asperities occurred, the total shear force, *S*, could according to Ladanyi and Archambauly (1970) be expressed as a sum of three components, as shown in Equation 11.

$$S = S_1 + S_2 + S_3 \tag{11}$$

Where S_1 is the component due to external work done in dilating against the external force *N*, S_2 is the component due to additional internal work in friction due to dilatancy, and S_3 is the component due to work done in internal friction if sample did not change volume in shear.

The value of the component *S1* can be determined by using the following equation:

$$S_1 = N \cdot \frac{dy}{dx} = N \cdot \dot{\upsilon} \tag{12}$$

Where N is the external normal force on the rock and $\dot{\upsilon}$ is the rate of dilation at failure, defined as the ratio between the increments of the normal (dy) and the shear (dx) displacement of failure. For the component S_1, the parameter $\dot{\upsilon}$ becomes $\tan i$ for regular saw-tooth asperities, and zero for a flat sliding plane.

The component S_2 is due to additional internal work in friction due to dilatancy, and can be determined by Equation 13.

$$S_2 = S \cdot \dot{\upsilon} \cdot \tan(\phi_f) \tag{13}$$

Where ϕ_f is the statistical average value of friction angle when sliding occurs along the irregularities of different orientations and S is the external shearing force.

The component S_3 is the shear force for flat rough surfaces with no irregularities and can be expressed as shown in Equation 14.

$$S_3 = N \cdot \tan(\phi_\mu) \tag{14}$$

Where ϕ_μ is the frictional resistance along the contact surfaces of the teeth.

When all the asperities are sheared off at the base due to high normal stresses, the shear strength should be equal to the component S_4, which can be expressed as showed in Equation 15.

$$S_4 = A \cdot c_i + N \cdot \tan(\phi_i) \tag{15}$$

Where c_i is the internal cohesion of intact rock, ϕ_i is the friction angle of intact rock, and A is the total surface area.

However, when shearing along an irregular rock surface, both shearing of the asperities and sliding over asperities can occur simultaneously. The part of surface area where the asperities are sheared off, A_s, will then be a portion of the total surface area, A, while sliding over asperities will occur on the remaining area (A-A_s). The total shear force can then be expressed as:

$$S = (S_1 + S_2 + S_3) \cdot (1 - a_s) + S_4 \cdot a_s \tag{16}$$

Where a_s is the shear ratio defined as A_s/A.

By inserting Equation 12 to 15 into Equation 16 and dividing with the surface area, A, and taking into account the degree of interlocking, η, the shear strength, τ, can be expressed as:

$$\tau = \frac{\sigma(1 - a_s)\left(\dot{v} + \tan\phi_\mu\right) + a_s(\sigma \tan\phi_i + c_i\eta)}{1 - (1 - as)\dot{v}\tan\phi_f} \tag{17}$$

Where the degree of interlocking is given by:

$$\eta = 1 - \Delta x/\Delta l \tag{18}$$

Where Δx is the length of the shear displacement and Δl is the projected length of the asperities in the shear direction. The definition of the degree of interlocking is illustrated in Figure 5 a).

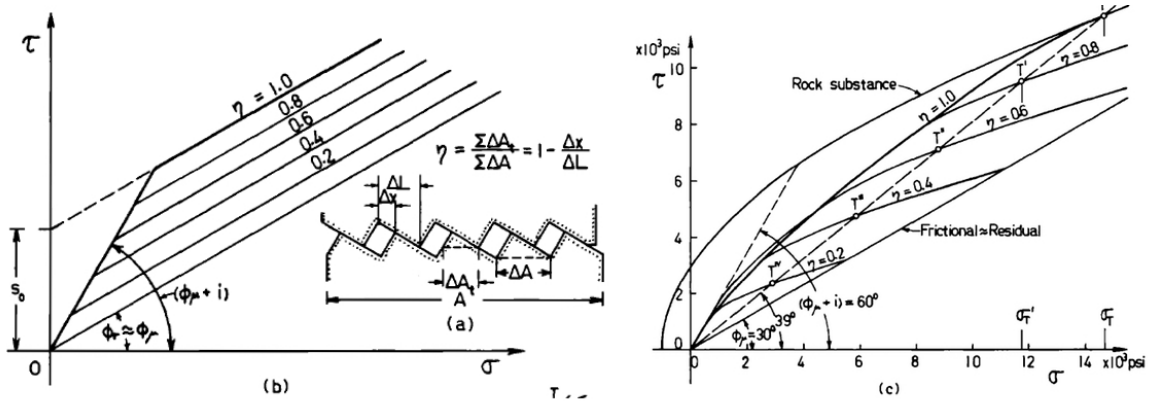

Figure 5: a) Defenition of degree of interlocking. b) Results according to the bilinear model. c) Results according to the proposed model. (Ladanyi and Archambauly, 1970)

Ladanyi and Archambauly (1970) suggested two approximations to express the shear ratio, a_s, and the rate of dilation at failure, $\dot{v}$, within the interval of normal stress $0 < \sigma_n < \sigma_t$. Equation

19 and 20 shows the proposed approximations for the shear ratio, a_s, and the rate of dilation at failure, $\dot{v}$, respectively.

$$a_s \approx 1 - \left(1 - \frac{\sigma}{\sigma_T}\right)^{k_1} \tag{19}$$

$$\dot{v} \approx \left(1 - \frac{\sigma}{\sigma_T}\right)^{k_2} \tan i \tag{20}$$

Where the exponents k_1 and k_2, according to the available experimental information, have values of about $k_1 \approx 3/2$ and $k_2 \approx 4$. Ladanyi and Archambauly (1970) pointed out that these equations should only be considered as help for visualizing probable variations in the two parameters, as they are not directly connected to the failure model.

Based on an experimental study, Ladanyi and Archambauly (1970) found that the proposed model could correctly represent the shear behavior of irregular rock surfaces. However, more experimental result is necessary to validate the model, especially concerning the parameters a_s and $\dot{v}$, which are only approximations.

3.1.4 JRC-JCS Model by Barton and Choubey (1977)

Barton and Choubey (1977) presented an empirical failure criterion that could be used to estimate the peak shear strength for natural surfaces. The criterion was based on extensive test results, and included the effects from roughness and the compressive strength of the joint surface. To describe the surface roughness, an expression which could be substituted with the dilatancy angle, *i,* in Patton´s criterion was proposed. The failure criterion, also known as the JRC-JCS model, can be expressed as shown in Equation 21.

$$\tau_p = \sigma_n \cdot \tan\left[JRC \cdot log_{10}\left(\frac{JCS}{\sigma_n}\right) + \phi_b\right] \tag{21}$$

Where τ_p is the peak shear strength, σ_n is the effective normal stress, *JRC* is the joint roughness coefficient, *JCS* is the joint compressive strength and ϕ_b is the basic friction angle. If the joint was weathered or altered, Barton and Choubey (1977) suggested that the residual friction angle, ϕ_r, should been used instead of the basic friction angle.

The joint compressive strength can according to Barton and Choubey (1977) be measured by using a Schmidt hammer on the joint surface. For weathered surfaces, the *JCS* will be lower than the compressive strength of intact rock.

The *JRC* values varies between 0 and 20, where 0 represents a completely smooth surface and 20 represents a very rough surface. Two different ways to determine the *JRC* value was suggested. The first method, suggested by Barton and Choubey (1977), is to visually inspect the roughness of the surface plane and then compare it to ten standard profiles given in Figure 6.

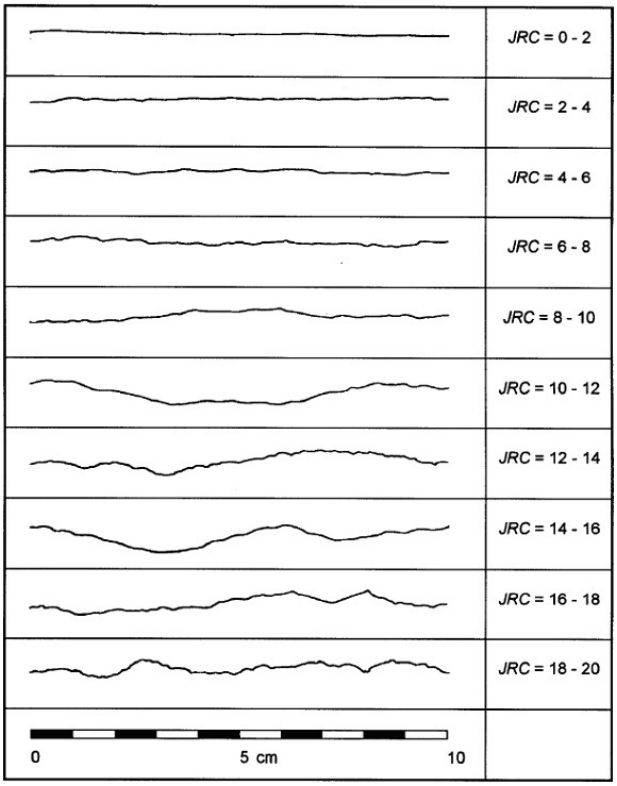

Figure 6: Standard profiles used for visual estimation of JRC (Barton & Choubey 1977

Visual inspections can be an unreliable method, as it depends on subjective judgements from the person preforming the inspection. The second method to estimate the *JRC* value was developed by Barton and Bandis (1982). They suggested to back-calculate the *JRC* value from laboratory tilt tests. The friction angle obtained from tilt test, ϕ', can be expressed in terms of the residual friction angle of a smooth surface, ϕ_r, and a roughness component, i, as shown in Equation 22.

$$\phi' = \phi_r + i \tag{22}$$

The roughness component, *i*, can be broken down and expressed in terms of the effective normal stress, σ_n, the joint compressive strength, *JCS,* and the joint roughness coefficient, *JRC,* as shown in Equation 23.

$$i = JRC \cdot \log\left(\frac{JCS}{\sigma_n}\right) \tag{23}$$

By combining Equation 22 and 23, an expression to calculate *JRC* was found, as shown in Equation 24.

$$JRC = \frac{\phi' - \phi_r}{\log\left(JCS/\sigma_n\right)} \tag{24}$$

Barton and Bandis (1982) studied the scale effects by performing shear tests over a range of block sizes. They found that the value of *JRC* and *JCS* values obtained for small samples would not be representable for in-situ conditions, as the joint roughness and asperity strength will decrease with increasing scale. To include the scale effects in the proposed criterion, they proposed equations for the correlation between the values obtained in laboratory and the corresponding value for in situ conditions. Equation 25 and 26 shows the proposed equations for scale effects for *JRC* and *JCS*, respectively.

$$JRC_n = JRC_0 \cdot \left(\frac{L_n}{L_0}\right)^{-0{,}02JRC_0} \tag{25}$$

$$JCS_n = JCS_0 \cdot \left(\frac{L_n}{L_0}\right)^{-0{,}03JRC_0} \tag{26}$$

Where the subscripts (0) and (n) means lab and in situ respectively, L_n is the length of the rock block being shared (in situ), L_0 is the length of the sample size (lab).

The JRC_n and JRS_n values calculated with Equation 25 and 26 can be inserted in Equation 21 to calculate the shear capacity for in-situ conditions.

3.1.5 Lo et al. (1990)

Lo et al. (1990) developed a shear strength criterion for partially bonded sliding planes. Under the assumption that the strengths from both bonded and unbonded contacts is mobilized on the same time, the following shear strength criterion was proposed:

$$\tau_p = c\left[1-\eta\left(1-\frac{c_s}{c}\right)\right]+\sigma_n \tan\phi_i\left[1-\eta\left(1-\frac{\tan\phi_s}{\tan\phi_i}\right)\right] \quad (27)$$

Where τ_p is the shear capacity of the sliding plane, σ_n is the effective normal stress, η is the ratio of area of unbonded portion to the total area, c and ϕ_i is the cohesion and friction angle for well bonded contacts respectively, and c_s and ϕ_s is the cohesion and friction angle for unbonded contacts, respectively.

In general, the value of c_s equal zero, as no cohesive forces are present when there is no bond in the interface. For unbonded contacts, the friction angle ϕ_s is the sum of the basic friction angle, ϕ_b, the roughness component from major surface asperities, i, and overall inclination of the sliding plane, α. The values of $tan\phi_i$, $\tan\phi_s$ and c should according to Lo et al. (1990) be determined by laboratory tests or in-situ tests.

3.1.6 Maksimović (1992)

Maksimović (1992) wanted to improve existing criteria that had shortcomings like limited stress ranges and lack of physical meaning. According to Maksimović (1992), the total shearing resistance could be expressed as the sum of the three components friction, dilatancy and failure of asperities. Based on this knowledge, he proposed a non-linear hyperbolic relation to describe the shear strength of rough rock joints, as shown in Equation 28.

$$\tau_p = \sigma_n \cdot \tan\left(\phi_b + \frac{\Delta\phi}{1+\frac{\sigma_n}{\rho_n}}\right) \quad (28)$$

Where τ_p is the shear capacity of the rock joint, σ_n is the effective normal stress, ϕ_b is the basic friction angle, $\Delta\phi$ is the joint roughness angle which can be described as the angle of maximum dilatancy for an undamaged rugged surface at zero normal stress and ρ_n is the median angle

pressure, which is equal to the value of the normal stress at which the contribution of dilation and the breakage of asperities is equal to half of $\Delta\phi$ at zero normal stress. The description of parameters in the criterion is illustrated in Figure 7.

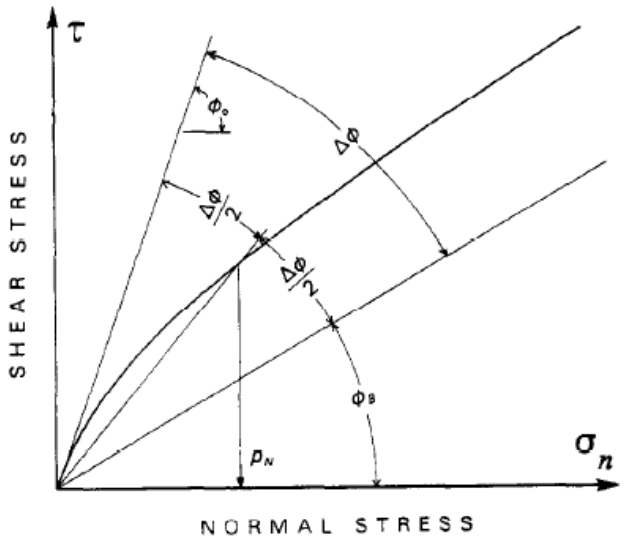

Figure 7: Description of parameters of the nonlinear failure envelope (Maksimović, 1992)

Several experimental results were used for verification of the proposed criterion. According to Maksimović (1996), this method have several advantages; the method is valid from zero to infinity normal stress, it is a simple mathematic calculation with only a couple of additions and divisions and the parameters have physical meanings. However, according to Grasselli (2001) there is a technical problem when trying to use this criterion, as it is necessary to perform at least three shear tests on the same surface to calculate the parameter ρ_n. In addition, it is not clear how to obtain these parameters in laboratory.

Furthermore, Maksimović (1996) proposed a link between his criterion and the well-known JRC-JCS model. A relationship between the joint roughness angle, $\Delta\phi$, and the joint roughness coefficient, *JRC*, were proposed, as shown in Equation 29.

$$\Delta\phi = 2 \cdot JRC \tag{29}$$

To make a link between the median angle pressure, ρ_n, and the joint compressive strength, *JCS*, the following equation were proposed:

$$\rho_n = 0{,}1 \cdot JCS \tag{30}$$

Based on the relationships in Equation 29 and 30, the non-linear failure criterion in Equation 28 can be rewritten in terms of *JRC* and *JCS*, as shown in Equation 31.

$$\tau_p = \sigma_n \cdot \tan\left(\phi_b + \frac{2 \cdot JRC}{1 + 10 \cdot \frac{\sigma_n}{JCS}}\right) \tag{31}$$

This simple conversation of from the proposed parameters to *JRC* and *JCS* can be a useful tool, as Barton´s model is widely used among geologists working with rock.

3.1.7 Dawson et al. (1998)

Based on the work of Lo et al. (1990), Dawson et al. (1998) proposed a more conservative shear strength criterion for the shear capacity for partially bonded sliding planes. Only the frictional contribution for a smooth surface was considered for the unbonded parts when estimating the shear capacity, the contribution from surface roughness due to mobilizes asperities were disregarded. Thus, Dawson et al. (1998) proposed the following shear strength criterion:

$$\tau_p = A_b \cdot (c + \sigma_n \tan \phi_i) + (1 - A_b) \cdot (\sigma_n \tan \phi_b) \tag{32}$$

Where τ_p is the peak shear strength, A_b is the ratio of bonded area to total area, c is the cohesive force in the bonded contacts, σ_n is the effective normal stress, ϕ_i is the internal friction angle for bonded contacts and ϕ_b is the basic friction angle.

The only difference from this criterion and the criterion proposed by Lo et al. (1990), is that this criterion does not include the effect from mobilized asperities in the unbonded contacts when estimating the shear capacity, while the criterion proposed by Lo et al. (1990) do. The peak friction angle, ϕ_p can be expressed as the sum of the basic friction angle ϕ_b and a roughness component i. The effect from mobilized asperities which is not included in Dawson's criterion corresponds to the roughness component, i, in the expression for peak friction angle.

3.1.8 Zhang et al. (2016)

Zhang et al. (2016) developed an expression for the peak dilatancy angle on the basis of shear mechanism and quantitative roughness assessment which was substituted into Patton's criterion to establish a new shear strength criterion for rock joints. Two quantitative roughness parameters, the revised root-mean-square of asperity angle, $tan^{-1}(Z_{2,r})$, and the maximum contact coefficient, C_m, were used to express the anisotropic surface characteristics joint surfaces. The revised root-mean-square of asperity angle, which accounts for the shear direction, can be expressed as shown in Equation 33.

$$\tan^{-1}(Z_{2r}) = \tan^{-1}\sqrt{\frac{1}{N+(\Delta x)^2}\sum_{i=1}^{N}[\max(0, y_{i+1}-y_i)]^2} \tag{33}$$

Where N is the number sampling points along the whole joint profile and x_i and y_i are the coordinates of equally spaced sampling points.

The maximum contact coefficient, which accounts for the asperity degradation, can be expressed as shown in Equation 34.

$$C_m = \frac{\sum_{i=1}^{N}\sqrt{\Delta x^2 + [\max(0, y_{i+1}-y_i)]^2}}{L_o} \tag{34}$$

Where L_0 is the projected length of profile in the joint plane.

Based on test results from conducted shear tests on artificial rock joints, the following peak shear strength criterion was proposed by Zhang et al. (2016):

$$\tau_p = \sigma_n \cdot \tan\left(\phi_b + \frac{tan^{-1}(Z_{2r})}{(1-C_m)^{0.64}}\left[1 - e^{-3.36C_m\frac{\sigma_t}{\sigma_n}}\right]\right) \tag{35}$$

Where τ_p is the peak shear strength, ϕ_b is the basic friction angle, σ_n is the effective normal stress, σ_t is the tensile stress and 0.64 and 3.36 are fitting parameters.

According to Zhang et al. (2016), there is a good correlation between the estimated shear strengths and test results obtained from shear tests conducted on artificial rock joints. However, the applicability on natural rock joints, the three-dimensional roughness characteristics and scale effects was not studied, so further research is needed to get a better understanding of the shear behavior of natural rock joints.

3.2 Shear strength criteria that can incorporate the 3D surface roughness

The last years, several authors have tried to incorporate the three-dimensional surface roughness to shear strength criteria, as new technology have made it possible to measure and characterize the three-dimensional roughness. This subsection presents the shear strength criteria that are developed to incorporate three-dimensional surface geometry.

3.2.1 Grasselli (2001)

Grasselli (2001) was the first to consider three-dimensional surface roughness of an interface in a shear strength criterion. During his work, Grasselli (2001) observed that only some of the contact surface were damaged during shearing and the area were scattered randomly. The scattered damaged areas indicated that the real contact area is only a small portion of the total surface area. Hence, Grasselli concluded that the whole surface area should be considered for analysis, since linear surface profiles (e.g *JRC* profiles) are not sufficient to capture all the scattered contact area that contribute to shear strength.

To obtain the three-dimensional parameters, a special optical measurement system is used to digitize the entire rock surface in 3D. After scanning, the rock surface is depicted as point clouds. The point clouds are then used to reconstruct the rough surface by using a specially triangulation algorithm (Grasselli, 2006). The triangles are created with a point spacing of 0.3 mm. For each triangle, the orientation can be uniquely identified by its azimuth angle, α, and dip angle, θ, as shown in Figure 8. The azimuth is the angle between true dip vector ($\boldsymbol{d}$) projected at the shear plane (called best-fit plane in Figure 8) and the shear vector ($\boldsymbol{t}$), measured clockwise from ($\boldsymbol{t}$). The dip angle, θ, is the angle between the triangle surface and the shear plane.

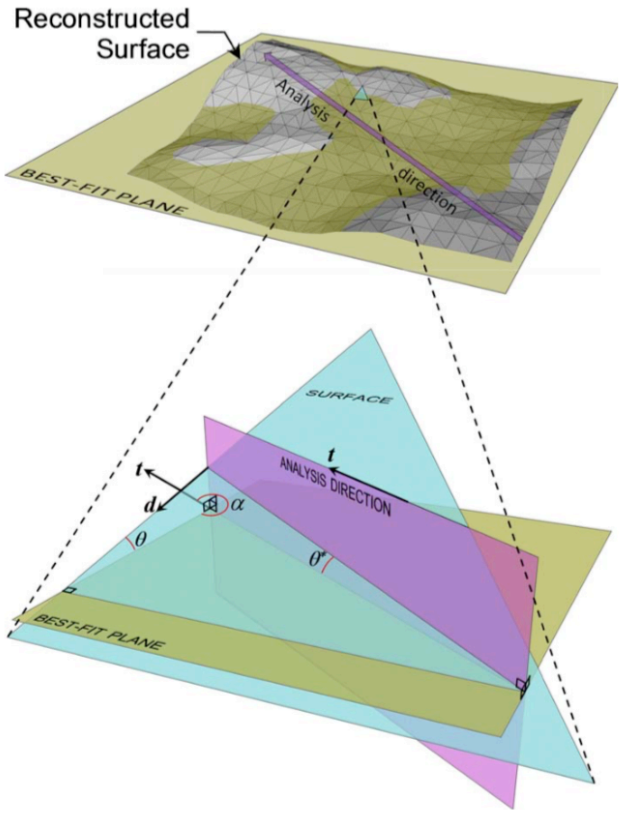

Figure 8: (Color outline) Schematic diagram illustrating the geometric definition of azimuth, dip and apparent dip in relation to the selected analysis direction (Tatone and Grasselli, 2009)

The apparent dip angle, θ^*, describes how steep each triangle is in respect to the chosen shear direction, and is related to the true dip angle as shown in Equation 36.

$$tan\theta^* = -tan\theta \cdot cos\alpha \tag{36}$$

According to Grasselli (2001), only the triangles facing the shear direction and is steeper than the threshold apparent dip angle, θ^*_{cr}, contribute to shear resistance. The triangles with apparent dip angles greater than the threshold angle will deform, shear or crush depending on how the applied normal load is redistributed, while the triangles with apparent dip angle equal to the threshold angle will just be in contact. The total potential contact area, A_{θ^*}, is the sum of all contact area that is in contact or damaged during shearing, normalized with respect to the total area. A cumulative distribution of the total potential contact area, A_{θ^*}, for different threshold angles is shown in Figure 9. This cumulative distribution is only valid for the specific shear direction, another shear direction could lead to a different distribution.

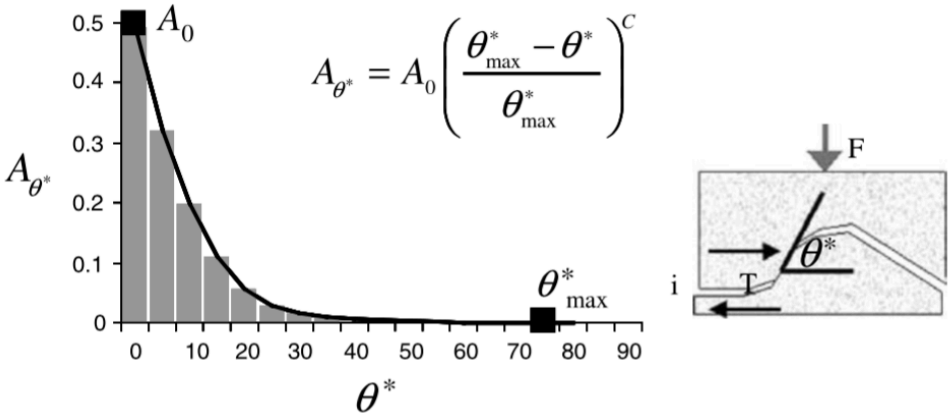

Figure 9: This plot describes, for a given shear direction, the distribution of the cumulative area of the surface A having a minimum inclination with respect to the average plane of the joint (Grasselli, 2006)

The relationship between total potential contact area, A_{θ^*}, and the apparent dip angle, θ^*, can be expressed as shown in Equation 37.

$$A_{\theta^*} = A_0 \left(\frac{\theta^*_{max} - \theta^*}{\theta^*_{max}} \right)^c \tag{37}$$

Where A_0 is the maximum possible contact area ratio in the shear direction calculated for a threshold angle of 0°, θ^*_{max} is the maximum apparent dip angle in the shear direction, and C is the roughness parameter which characterizes the distribution of the apparent dip angles over the surface, calculated using a best-fit regression function.

The parameters A_0, C and θ^*_{max} describes the contribution from the surface morphology to the frictional behavior, and are all dependent on the specific shear direction (Grasselli et al., 2002b). The parameters can be found by scanning the surface and then use the triangular algorithm to regenerate the surface.

To estimate the maximum possible contact area, A_0, it is first necessary to specify the shear direction, since contact can only occur on those triangles facing the shear vector (***t***). Then, Equation 38 can be used to calculate the maximum possible contact area.

$$A_0 = \frac{A_l}{A_m} \tag{38}$$

Where A_l is the sum of area facing the shear direction and A_m is the actual area of the whole joint surface. The maximum possible contact area ratio is almost always close to 0.5 (Grasselli et al., 2002b).

The roughness parameter C is calculated using a best-fit regression function (Equation 37), which characterizes the distribution of the apparent dip angles over the surface. C is a fitting parameter that describes the shape of the cumulative distribution. The roughness parameter decreases with shearing, as the distribution of angularity is smoothed out. The value of C can range from 0 to infinity, where a value of 0 characterizes a saw tooth profile, and a value approaching infinity represents a smooth surface (Grasselli et al., 2002a). A surface with a high amount of steep inclinations will have a lower C, as the fitting line will be less concave. A surface with high amount of non-steep inclinations will have a higher value of C, as the fitting line will be more concave (Tatone and Grasselli, 2009). The maximum apparent dip angle, $\theta^*_{max,}$ is equal to the steepest apparent dip angle with respect to the shear direction.

The shear strength criterion proposed by Grasselli (2001), was a new constitutive model that relates stress and displacement in order to model the shear resistance of joints under constant normal load. The challenge was to include the morphology of the joint into a shear strength criterion. The method is based on more than fifty shear tests with constant normal load and on the empirical surface description with three-dimensional roughness parameters. The first expression he proposed is shown in the following expression:

$$\tau_p = \sigma_n \cdot \tan(\phi_r') \cdot \left[1 + e^{\frac{-\theta^*_{max}}{A_0 \cdot C} \cdot \frac{\sigma_n}{\sigma_c}}\right] \tag{39}$$

Where τ_p is the peak shear strength, σ_n is the applied average normal stress, ϕ_r' is the residual friction angle (after a standard displacement of 5 mm), θ^*_{max} is the maximum apparent dip angle with respect of the shear direction, A_0 is the maximum potential contact area, C is the roughness parameter and σ_c is the compressive strength of intact rock material.

According to Grasselli (2001), the tensile strength is a more important parameter than the compressive strength when quantifying the peak shear strength for rock joints, as tensile failure of asperities were the major failure mode for asperities. Therefore, a more general expression

was derived that holds for both mortar replicas and rock joints. The tensile strength, σ_t, was substituted for compressive strength and a parameter P was introduced in the denominator of the argument to the exponential expression. The parameter P was found to be 9.0 by performing multiple least-squares regression using the data obtained by conducted shear tests. Thus, Grasselli (2001) proposed the following expression:

$$\tau_p = \sigma_n \cdot \tan(\phi_r') \cdot \left[1 + e^{\frac{-\theta^*_{max}}{9 \cdot A_0 \cdot C} \frac{\sigma_n}{\sigma_t}}\right] \quad (40)$$

Considering that the friction is dependent on the basic friction angle, surface roughness, load condition and the internal structure of the rock like the schistosity, the following expression for peak shear strength were proposed:

$$\tau_p = D\sigma_n \cdot \tan(\phi_b + i) = \left[1 + e^{-\left(\frac{\theta^*_{max}}{9 \cdot A_0 \cdot C} \frac{\sigma_n}{\sigma_t}\right)}\right] \cdot \sigma_n \cdot tan\left[\phi_b + \left(\frac{\theta^*_{max}}{C}\right)^{1{,}18 \cdot \cos\beta}\right] \quad (41)$$

Where ϕ_b is the basic friction angle, i is the dilation angle, and β is the angle between schistosity plane the plane normal to the joint (if no schistosity, assume 0). D is a factor that accounts for the decrease in "influence" of roughness in shear strength value due to the normal stress.

This shear strength criterion can estimate the real contact area involved in shearing. This was confirmed by comparing the empirical results with the tests results (Grasselli, 2001). As the contact area is sheared off or damaged during shearing, it can be said that shearing modifies the surface morphology. To understand how the parameters changed with shearing, Grasselli (2006) measured several surfaces before and after shearing. The asperities with the steepest inclinations was expected to shear, and this behavior was captured by the parameters as the maximum apparent dip angle, θ^*_{max}, decreased after shearing due to smoothening of the damaged asperities.

An advantage with this method is that all the needed parameters can easily obtained through standard laboratory tests and scanning of surfaces. However, the scale effects have not been investigated, and the criterion is only valid within the test range (σ_n/σ_c = 0.01 – 0.04 and σ_c/σ_t = 5 – 46). In addition, the criterion can be hard to understand from an engineering point of view,

as the criterion is not intuitive and cannot be written on a Mohr-Coulomb type of form. Another limitation with this method is that the method cannot be used for smooth joints, as the criterion is then simplified to $\tau_p = 2\sigma_n \tan(\phi_b)$, and this do not correspond to the criteria for smooth joints proposed by Patton and Mohr-Coulomb.

The proposed model can also be used to estimate the *JRC* value. Today, *JRC* values are normally estimated by comparing the surface roughness to ten standard profiles, which is a subjective method. The goal is to calculate the shear resistance using known parameters and not to calculate the shear resistance by subjective methods. Therefore, Grasselli and Egger (2003) presented an expression for *JRC* based on quantitative surface description as shown in Equation 42.

$$JRC = \frac{\arctan\left\{\tan\left[\phi_b + \left(\frac{\theta^*_{max}}{C}\right)^{1.18\beta}\right]\left[1 + e^{-(\theta^*_{max}/9A_0C)(\sigma_n/\sigma_t)}\right]\right\} - \phi_b}{\log_{10}(\sigma_c/\sigma_n)} \tag{42}$$

This expression makes it possible to quantify *JRC* by considering the whole surface, and not only a single profile.

3.2.2 Xia et al. (2014)

A new empirical shear strength criterion for rock joints was proposed by Xia et al. (2014). They wanted to create a more intuitive criterion from an engineering point of view, as the criterion proposed by Grasselli (2001) can be hard to understand. Based on the three-dimensional roughness parameters developed by Grasselli, Xia et al. (2014) proposed a shear strength criterion with a formulation that can be related to the well-known Mohr-Coulomb criterion in addition to an explicit description of the dilatancy angle.

A function for peak dilatancy angle, $d_{n,peak}$, was developed by Xia et al. (2014) based on the equation for potential contact area, A_{θ^*}, (Equation 37) and the dilatancy angle boundary conditions under zero and critical normal stress levels, as shown in Equation 43.

$$d_{n,peak} = \frac{4A_0\theta^*_{max}}{C+1} \cdot \left[1 + exp\left(-\frac{1}{9A_0} \cdot \frac{\theta^*_{max}}{C+1} \cdot \frac{\sigma_n}{\sigma_t}\right)\right] \tag{43}$$

By substituting the proposed function Equation 43 in a Mohr-Coulomb type of formulation like the criterion proposed by Patton in Equation 9, Xia et al. (2014) proposed the following shear strength criterion:

$$\tau_{peak} = \sigma_n \tan\left\{\phi_b + \frac{4A_0\theta^*_{max}}{C+1} \cdot \left[1 + exp\left(-\frac{1}{9A_0} \cdot \frac{\theta^*_{max}}{C+1} \cdot \frac{\sigma_n}{\sigma_t}\right)\right]\right\} \quad (44)$$

It was observed that values calculated by using this criterion agrees well with test results from conducted shear tests, hence, the criterion can estimate the shear strength at laboratory scale. Comparison between this criterion and the Grasselli criterion showed that both criteria can estimate the shear strength for rock joints in an accurate way (Xia et al., 2014). The advantage of this criteria is that is it easier to understand than the proposed model from Grasselli, and can easily be adopted by consultants using Mohr-coulomb type of functions. The relationship between peak dilatancy angle and the three-dimensional roughness characteristics was connected in the proposed expression for dilatancy angle in Equation 43. However, as pointed out by Hou et al. (2015), the fitting constants in this model is not dimensionless and has no physical meaning, which makes it hard to understand. It was noted that the new shear strength criterion tends to overestimate the shear strength at high normal stresses, but according to Xia et al. (2014) this may be due to weak materials used in the casted replicas.

Tang and Wong (2015) were aware that the shear capacity of rock joints was not only affected by the surface roughness, but also degree of matching between the joints. Therefore, Tang and Wong (2015) extended the criterion proposed by Xia et al. (2014) to include the degree of matching between the joint surface. However, concrete dams are often assumed to be perfectly mated with no dislocation between the rock and concrete surfaces. The criterion proposed by Xia et al. (2014) will then be a better alternative, as that criterion is simpler than the criterion proposed by Tang and Wong and the degree of dislocation is not so relevant for concrete dams. As a result, the criterion was not considered in this thesis.

3.2.3 Johansson and Stille (2014)

Based on the work of Johansson (2009), Johansson and Stille (2014) proposed a new conceptual model to describe the dilation angle for joints. The model was based on adhesion and fractal theory, measurement of surface roughness, and the understanding of the different failure modes

for a single asperity. In addition, the model considers how the size of the contact points changes as a function of scale and matedness, and how dilation angle changes at grain scale.

In their work, Johansson and Stille (2014) analyzed how a single idealized asperity could fail. In the analysis, they assumed that only the side of the asperity facing the shear direction was loaded, as shown in Figure 10. The height of the idealized asperity, h_{asp}, can be expressed as shown in Equation 45.

$$h_{asp} = \frac{L_{asp}}{2} \tan i \tag{45}$$

Where L_{asp} is the length of asperity base and i is the angle of inclination.

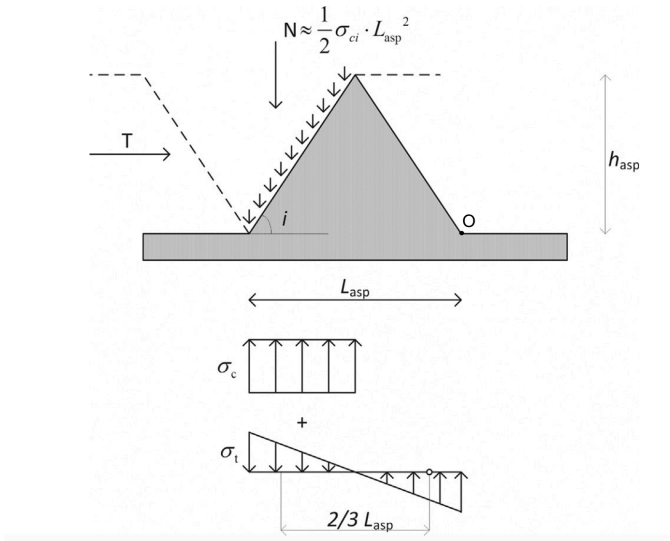

Figure 10: Two-dimensional idealized asperity used in the calculation with a base area equal to L^2_{asp}, height, h, and inclination, i (Johansson and Stille, 2014)

According to Johansson and Stille (2014) a single asperity can fail through sliding, shearing or tensile failure depending on the present normal stress. They presented the ratio between the resistance, T, and the normal load, N, for all the failure modes. For sliding failure, the relationship between resistance and normal load could be calculated by using Patton´s criterion, as shown in Equation 46.

$$\frac{T}{N} = \tan(\phi_b + i) \tag{46}$$

Where ϕ_b is the basic friction angle and i is the dilation angle which equals the asperity inclination.

For shearing failure at the base of the asperity, the relationship between resistance and normal load can be expressed by using Mohr-Coulomb or Patton´s equation for residual strength, as shown in Equation 47.

$$\frac{T}{N} = \frac{2c_i}{\sigma_{ci}} + \tan(\phi_i) \tag{47}$$

Where c_i is cohesion for intact rock, σ_{ci} is the uniaxial compressive strength for rock, ϕ_i internal friction angle for intact rock.

Tensile failure of rock is assumed to occur when the maximum tensile stress, due to loads acting on the asperity, exceeds the tensile strength of the rock. Moment equilibrium at point O in Figure 10 were used to find the ratio between resistance and normal load for tensile failure, and the ratio can be expressed as shown in Equation 48.

$$\frac{T}{N} = \frac{4(c_i + \sigma_{ti})}{3\sigma_{ci} \cdot \tan(i)} \tag{48}$$

Where σ_{ti} is the tensile strength of intact rock.

The asperity inclination determines which of the abovementioned failure modes that will occur. For different asperity inclinations, the smallest shear resistance of Equation 46, 47 and 48 determines what kind of failure mode that will occur. According to Johansson and Stille (2014), sliding failure will govern the shear strength for low values of asperity inclinations, while higher values of asperity inclinations will lead to shearing of asperities. If the inclination increases even further, tensile failure of the intact rock will occur. The value of asperity inclination where changes between failure modes occur is not constant, as it changes with type of rock. For hard rocks, sliding failure can be the governing failure mode for higher asperity inclinations than for soft rocks.

Johansson and Stille (2014) used a self-affine fractal model to describe the surface roughness. Based on self-affine fractal models, a scaling relation between the asperity height, $h_{asp,}$ and the asperity base length, L_{asp}, exist, as presented in Equation 49.

$$h_{asp} = aL_{asp}^{H} \tag{49}$$

Where a is an amplitude constant and H is the Hurst exponent.

According to Johansson and Stille (2014), the adhesion theory states that the contact area ratio, $A_{c,r}$, can be expressed as the ratio between the effective normal stress, σ_n, and the yield strength, which can be approximated with the uniaxial compressive strength, σ_{ci}, as shown in Equation 50.

$$A_{c,r} = \frac{\sigma_n}{\sigma_{ci}} \tag{50}$$

Grasselli (2001) also proposed an expression for the contact area ratio, which he called the potential contact area, $A_{\theta*}$. This was an empirical relation, and can be expressed as shown in Equation 51.

$$A_{\theta^*} = A_0 \left(\frac{\theta^*_{max} - \theta^*}{\theta^*_{max}} \right)^c \tag{51}$$

Where A_0 is the maximum possible contact area ratio in the shear direction, θ^*_{max} is the maximum apparent dip angle in the shear direction, and C is the roughness parameter.

When applying normal load on perfectly mated rock joints, the smallest asperities facing the shear direction were assumed to crush, since the contact areas are too small to carry the whole load. If sliding is the failure mode, the asperities will continue to crush until the contact area becomes equal to the contact area associated with plastic flow at grain size, and the measured dip angle at for asperities in contact, θ^*, becomes equal to the dilation angle for the surface at grain scale, i. Under these assumptions, Johansson and Stille (2014) combined Equation 50 and 51 and proposed the following expression for the dilation angle for a perfectly mated joint at grain scale, $i_{g,}$:

$$i_g = \theta^*_{max} - \theta^*_{max} \cdot 10^{\frac{\log\left(\frac{\sigma'_n}{\sigma_{ci}}\right) - \log A_0}{C}} \tag{52}$$

Based on the scaling relationship in Equation 49, the expression for asperity height in Equation 45, and the expression for dilation angle at grain size in Equation 52, an expression for the length of the asperities in contact at grain scale can be found:

$$L_{asp,g} = \left[\frac{0.5}{a}\left[\tan(\theta^*_{max} - \theta^*_{max} \cdot 10^{\frac{\log\left(\frac{\sigma'_n}{\sigma_{ci}}\right) - \log A_0}{C}}\right]\right]^{\frac{1}{H-1}} \tag{53}$$

To express the length of a full-size asperities, they combined two expressions for the ratio between the number of contact points at sample size and grain size. The length of a full-size asperity, $L_{asp,n}$, can then be expressed as shown in Equation 54.

$$L_{asp,n} = L_{asp,g}\left(\frac{L_n}{L_g}\right)^k \tag{54}$$

Where L_n is the sample size, L_g is the grain size, k is an empirical constant that reflects the degree of matedness that varies from 0 for a perfectly mated joint to 1 for a maximal unmated joint.

By combining the expressions for the length of asperities at grain scale and the in Equation 53, the length of full-sized asperities in Equation 54, the scaling relationship in Equation 49 and the expression for asperity height in Equation 45, an expression for the dilation angle for full size joints, i_n, was proposed as shown in Equation 55.

$$i_n = tan^{-1}\left[tan\left(\theta^*_{max} - \theta^*_{max} \cdot 10^{\frac{\log\left(\frac{\sigma'_n}{\sigma_{ci}}\right) - \log A_0}{C}}\right)\left(\frac{L_n}{L_g}\right)^{kH-k}\right] \tag{55}$$

The mobilized friction angle, ϕ_p, can then be expressed as a sum of the dilation angle for full size joints and the basic friction angle, ϕ_b, as shown in Equation 56.

$$\phi_p = \phi_b + i_n \tag{56}$$

In order to use this shear strength criterion, it is necessary to scan the surface to obtain the 3D roughness parameters which was developed by Grasselli (2001), and adopted by Johansson and Stille (2014) in this criterion. When investigating the ability to estimate the shear strength with this model, Johansson (2016) used a point spacing of 0.5 *mm* when regenerating the surface to obtain the parameters.

This conceptual model is based on several assumptions which must be considered before using the model. According to Johansson and Stille (2014) some of the limitations with this model is that the grain size is assumed, and the maximal asperity length of the joint is assumed to be equal the sample length, even though it can be smaller. Further studies are necessary to see how, or if, the actual grain size affects the shear displacement at peak shear strength. In addition, the model was developed under the assumption that the normal stress increases monotonically and changes in the dilation angle are not considered. Furthermore, this proposed criterion is based on the single asperity failure model, which is a simplified description of a complex process. Another limitation mentioned is that the model does not consider any elastic deformation of the asperities. However, according to Johansson and Stille (2014) this is acceptable for hard rocks, but for soft rocks this limitation will increase as elastic deformation can enable contact with several asperities with different inclinations. If considering rock-concrete interfaces, concrete is a "soft" material with some elastic deformation which may result in increased contact in the interface. However, this elastic deformation will probably not influence the shear strength significantly.

An interesting thought by Johansson and Stille (2014) is that there is no scale effects for perfectly mated joints, however, this has not been verified yet. As a result, the criterion only considers scale effects for unmated joints, while no scale effects are assumed to occur for perfectly mated joints.

3.2.4 Hou, Rong, Yang, Zhou, Peng & Wang (2015)

Hou et al. (2015) developed a new shear strength criterion for rock joints based on shear tests of several tensile rock joint samples. The shear tests were conducted in order to relate the peak

shear strength to the three-dimensional surface morphology. The purpose of the new shear strength criterion was to improve the existing shear strength criteria (Grasselli, 2001, Xia et al., 2014) by creating a shear strength criterion that could be related to Mohr-Coulomb. The criterion proposed by Xia et al. (2014) can be formulated like Mohr-Coulomb, but according to Hou et al. (2015), the fitting constants in these criteria was hard to understand as they were not dimensionless.

Considering the decrease in dilation angle with increasing normal stress, the importance of tensile strength of rock joints on the shear properties and the influence of the 3D average inclination angle, $\bar{\theta}^*$ and maximum contact area ratio, A_0 on peak dilatancy angle, Hou et al. (2015) proposed a new dimensionless expression for the peak dilation angle based on cyclic shear tests as shown in Equation 57.

$$i_p = \frac{\bar{\theta}^*}{a \cdot \frac{\sigma_n}{\sigma_t} + b \cdot A_0} \tag{57}$$

Where i_p is the peak dilation angle, A_0 is the maximum contact area ratio, $\bar{\theta}^*$ is the 3D average inclination angle, σ_n is the normal stress, σ_t is the tensile strength and a and b are fitting constants.

By inserting the expression for peak dilation angle in Equation 57 into Patton's shear strength criterion in Equation 9, the new shear strength criterion can be expressed as shown in Equation 58.

$$\tau_p = \sigma_n \tan\left(\phi_b + \frac{\bar{\theta}^*}{a \cdot \frac{\sigma_n}{\sigma_t} + b \cdot A_0}\right) \tag{58}$$

According to Hou et al. (2015), one of the limitations with this criterion is that the 3D parameters are the averaged values of the joint surface. Thus, the scale effects should be considered when using this criterion. In addition, the relationship between roughness scale effects and shear strength scale effects should be investigated.

According to Hou et al. (2015) this criterion is more intuitive than Xia's and Grasselli's criteria from an engineering point of view. By creating an expression for the dilatancy angle with 3D roughness parameters, the criterion could be formed like the well-known Mohr-Coulomb

criterion. In addition, the fitting parameters were dimensionless, which makes it easier to understand. Hou et al. (2015) did not investigate the relationship between roughness scale and shear strength scale effects, so further work was recommended to obtain a better understanding of the shear mechanisms.

3.3 Analysis and comparison of existing shear strength criteria

In this following discussion, the studied shear strength models will be compared and analyzed with respect to their capacity to address the factors that influence the shear strength discussed in section 2.3.

Table 6 presents an overview of existing shear strength models and their capacity of incorporate different aspects that can influence the estimated shear strength. The criteria are analyzed with respect to their capacity to address the surface roughness (2nd order asperities), the adhesive bond between rock and concrete, the changes in failure modes and degradation of dilatancy angle due to the level of normal stress, the shear direction, location of big asperities and how they influence the failure path, and scale effects.

Table 6: Analysis of shear strength models and their capacity to address factors that influence the predicted peak shear strength

Criterion	Equation	Roughness	Adhesive bond	Normal stress	Shear direction	Location of asperities	Scale effect
M-C	Eq. 8	× ϕ	✓	×	×	×	×
Patton	Eq. 9 Eq. 10	✓ saw tooth	× ✓	×	×	×	×
Ladanyi et. al	Eq. 17	✓ *S1 & S2*	×	✓	×	×	×
Barton	Eq. 21	✓ 2D (*JRC*)	×	✓	×	×	✓*
Lo et al.	Eq. 27	✓ ϕ_s & ϕ_i	✓	×	×	×	×
Maksimović	Eq. 28	✓ $\Delta\phi$	×	✓	×	×	×
Dawson et al.	Eq. 32	× Only ϕ_b	✓	×	×	×	×
Zhang et al.	Eq. 35	✓ 2D ($tan^{-1}(Z_{2r})$ & C_m)	×	✓	✓	×	×
Grasselli	Eq. 41	✓ 3D	×	✓	✓	×	×
Xia et al.	Eq. 44	✓ 3D	×	✓	✓	×	×
Johansson	Eq. 55	✓ 3D	×	✓	✓	×	✓**
Hou et al.	Eq. 58	✓ 3D	×	✓	✓	×	×

* The scaling criteria may not be applicable to dam foundations (Donnelly and Rigbey, 2003).

** The assumption that there is no scale effects for perfectly mated joints is not verified (Johansson, 2016)

The surface roughness is important, as it increases the shear strength considerably. Even though the surface roughness is not included as an own term in Mohr-Coulomb and Lo et al., the effect from surface roughness can be said to be included in the friction angles. For Mohr-Coulomb, the friction angle can be chosen based on the Norwegian guidelines (NVE, 2005), found from shear test or from literature, and the friction angle will increase with increasing surface roughness in the interface. Lo et al. included the effect from roughness in the friction angles ϕ_s and ϕ_i, which are the friction angles for bonded and unbonded parts, respectively. Dawson et al. chose a more conservative approach than Lo. et al. by only including the basic friction angle for the unbonded areas. The contribution from surface roughness of these areas is therefore not considered. Patton (1966) included the effect from roughness by using saw-tooth asperities. However, this is not sufficient to describe the natural surface roughness found in dam foundations, as natural surfaces consist of irregular asperities and Patton's criterion is only applicable on surfaces with saw-tooth asperities with same size. Barton's criterion was one of the first to include the natural surface roughness in a shear strength criterion. The joint roughness coefficient, *JRC*, is used to expresses the surface roughness, where a smooth surface will result in a low *JRC* and a rough surface results in a higher *JRC* value. In the criterion proposed by Ladanyi and Archambauly (1970), the effect from surface roughness is included in the components *S1* and *S2*, while Maksimović (1992) included the surface roughness in terms of a joint roughness angle, $\Delta\phi$, which also can be expressed in terms of *JRC*. Zhang et al. (2016) described the two-dimensional surface roughness with the two roughness parameters $\tan^{-1}(Z_{2r})$ and C_m, which together are able to capture the anisotropic roughness characteristics. The criterion presented by Grasselli (2001) was the first to include the effect of three-dimensional surface roughness. This method address the surface roughness in a very accurate way, as the surface is scanned and represented by multiple triangles that describes the morphology of the surface (2^{nd} order asperity). The contribution from roughness is captured by the surface parameters that are calculated from the entire surface, and not only a single profile, as in Barton´s criterion. The three-dimensional surface morphology parameters, A_0, C and θ^*_{max} has later been adopted by several authors (Johansson and Stille, 2014, Xia et al., 2014, Hou et al., 2015) to describe the three-dimension surface roughness of the considered specimen.

The cohesive forces due to adhesive bond between the rock-concrete interface is included in the models presented by Mohr-Coulomb, Lo et al. and Dawson. The reason why only a few

models include the bond strength, is because most of the models are developed for rock joints, where bonding is not present. Lo et al. and Dawson´s models are both developed to consider partially bonded interfaces. This may be useful as the interface of concrete dams are not always completely bonded due to weathering and/or the bond strength could be weak. In this case, the full bond strength should only be applied on those parts where bonding is documented.

Changes in failure modes and degradation of asperities due to increase in normal stress is not considered by all models. Patton developed two different equations for shear strength, one for low normal stresses and one for high normal stresses. Hence, the criterion is unable to describe different failure modes occurring simultaneously, as his bilinear model can only describe sliding or shearing one at a time. However, Ladanyi and Archambauly (1970) considers the change in failure mode from sliding to shearing of asperities due to increasing normal stress. For higher normal stresses, the asperities are shared off at base instead of sliding over each other. The criterion makes it possible to considering these two failure modes simultaneously, where some of the surface asperities will slide over each other, and some will break at the base due to high normal stresses. Barton expressed the surface roughness with the term $JRC \cdot log(JCS/\sigma_n)$, which decreases with increasing normal stress. The term also includes the joint compressive strength which influences how much the effect from roughness will decrease, as a stronger material can be exposed for higher normal stresses before the asperity is sheared off. Maksimović's model describes a non-linear failure envelope which is valid for all values of normal stresses. This model is therefore able to consider the degradation of asperity angles under high normal stresses, and as a result, the amount of surface roughness that contributes to shear strength will decrease. Zhang et al. (2016) used the maximum contact coefficient, C_m, as a degradation parameter to describe the asperity degradation due to increasing normal stress. Grasselli´s criterion captures the decrease in influence from surface roughness with increasing normal stress by introducing the factor D, which decreases when the normal stress increases. However, Grasselli´s criterion is not valid for all ranges of normal stress, this criterion is only verified within the test range $\sigma_n/\sigma_c = 0.01 – 0.04$. Hou et al. (2015) and Xia et al. (2014) also includes the effect of decrease in influence of roughness with increasing normal stress in their expressions for dilatancy. Johansson and Stille (2014) considered the different failure modes with three different equations. However, the expression for dilation angle alone, is not able to consider the decrease in influence from surface roughness with increasing normal stress.

The shear direction is important as the contact area that contributes to shearing varies with shear direction. Barton´s shear criterion will not capture the difference if shearing in different directions in the same profile, since the linear surface profile used to determine the *JRC* will result in the same *JRC*, even if the surface profiles are mirror facing. However, if shearing in another direction that results in a different linear profile, the *JRC* may change and result in a different estimated shear strength. In Zhang et al. (2016)'s criterion, the two roughness parameters $\tan^{-1}(Z_{2r})$ and C_m is able to capture the different surface roughness in forward and reversed direction along a single profile, as both parameters changes with the shear direction. The 3D roughness parameters A_0, C and θ^*_{max}, which describes the contribution from the surface morphology, is found by an algorithm that is dependent on the direction of movement. The parameters will change with shear direction, since the roughness and contact area will vary for different shear directions. Therefore, all the criteria that contains these parameters (Johansson and Stille, 2014, Xia et al., 2014, Hou et al., 2015, Grasselli, 2001) will include the effect from shear direction on shear strength.

It is common agreement that 1st order asperities are likely to influence the shear strength on concrete dams. As discussed in subsection 2.3.5, effect from location of asperities was only observed for shear test conducted with a combination of shear and moment. This combination resulted in non-uniform normal stresses in the samples, which is representable for real concrete dams. However, all the considered shear strength criteria are developed for uniform normal stresses, and no effect on location of asperities were observed for shear tests with uniform normal stress. None of the existing criteria considers the location of 1st order asperities in their expression for peak shear strength. When visually comparing the surface roughness to the ten standard profiles in Barton's criterion, it does not matter if the largest asperities are located in the middle or at one of the sides of the shear profile, the *JRC* value will remain the same. This is because the profiles in Figure 6 just illustrates the amount of roughness and size of the asperities, not where the large asperities should be located. In addition, *JRC* values may not be suitable to describe the 1st order asperities, but is more applicable on 2nd order asperities, like the surface roughness. Grasselli's criterion is based on a cumulative description of the amount of asperities with different apparent dip angles, and this cumulative description does not consider if the asperities are placed in the front, back or in the middle of the surface. Hence, a surface with all the asperities placed in the back will give same calculated shear strength as a surface with the asperities placed in the middle, if the contact area is the same (shearing in same direction). Likewise, the criteria do not consider if the contact area is divided over several small

asperities (2^{nd} order roughness) or if the contact area comes from one big asperity (1^{st} order asperity). However, Grasselli's criterion was developed to describe the 2^{nd} order asperities, not 1^{st} order asperities. Neither of the other shear strength models studied the effect from location of asperities, thus, none of the identified shear strength criteria includes the effect from location of asperities. If there is one or several 1^{st} order asperities in the dam foundation which is likely to influence the shear strength, none of the existing criteria will be able to include when estimating the shear capacity. In order to include the effect from 1^{st} order asperities, methods were the non-uniform normal stress distribution can be proven and determined, and the effect from location of asperities due to non-uniform normal stress can be included, must be developed.

Barton's equations for scale effect reduces the values for *JRC* and *JCS* when the sample size is increased. As discussed earlier, bigger samples are more likely to include weak zones which will reduce the strength, and the *JCS* is therefore reduced with increasing size. The reason why the *JRC* decreased with increasing sample size, is because the term went from expressing the 2^{nd} order roughness for small samples, to express 1^{st} order roughness for samples at in-situ scale. However, according to Donnelly and Rigbey (2003), Barton recommended that the scaling criterion should only be used at dams with average block size less than 1.0 *m*. As a result, this scaling criterion will most likely not be applicable on rock-concrete interfaces in dams, as the length of the interface often exceeds this limit. Johansson proposed a shear strength criterion which expressed the length of a full-size asperities by combining two expressions for the ratio between the number of contact points at sample size and grain size. According to the criterion, there is no scale effects for perfectly mated joints, while scale effect for joints with dislocation can be observed.

4 Laboratory shear tests

4.1 Introduction

Four direct shear tests with constant normal load (CNL) has been conducted on core samples from dam Kalhovd. The shear tests were conducted to study the shear capacity of the dam and study the accuracy of shear strength models by comparing estimated shear strengths with shear test results. The tests were carried out at the COMPLAB at Luleå Tekniska Universitet (LTU), where they have previous experience with similar shear tests (Johansson, 2009, Liahagen, 2012, Krounis et al., 2016). In the following sections, the test procedure and the results from the shear tests is presented.

4.2 Shear test apparatus

The shearing apparatus consists of a highly-reinforced steel frame of 2.5 x 2.5 *m* with a sample holder in the lower part of the frame, as shown in Figure 11.

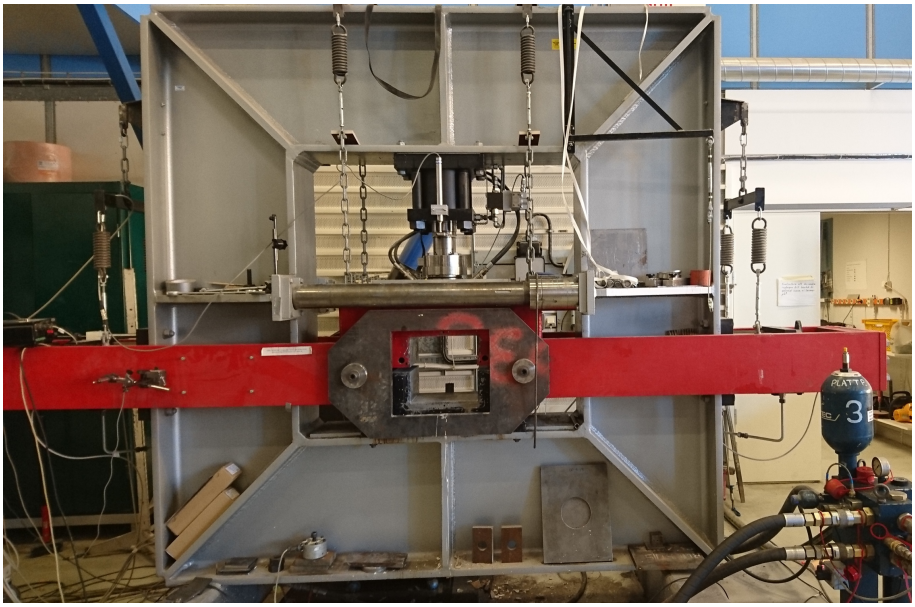

Figure 11: Direct shear test apparatus at LTU.

Shearing is performed by two hydraulic 500 *kN* actuators, which are responsible for shearing in one direction each. Two arms are connected to the upper part of the sample holder of steel. Normal load is applied on the sample by a 500 *kN* hydraulic actuator mounted inside of the upper part of the load frame. The normal force is transferred on the sample through a spherical

bearing and by an oil lubricated flat slide bearing down to the upper part of the sample. The oil lubricated flat slide bearing works as a frictionless joint surface.

Two heavy steel rods are applied on each side of the opening to stiffen the frame in order to prevent horizontal deformation. The entire shearing system (red part) is freely attached to the frame with springs. The spring system allows the moving parts in the shearing system to rotate approximately ± 10 degrees in the line of shearing.

The sample holder consists of an upper and lower part, as seen in Figure 12. The test specimen is placed in the sample holder and the top part of the sample is clamped with bolts to the upper part of the sample holder, while the lower part of the test specimen is clamped to the lower part of the sample holder. The sample holder determines the maximum size of the test samples.

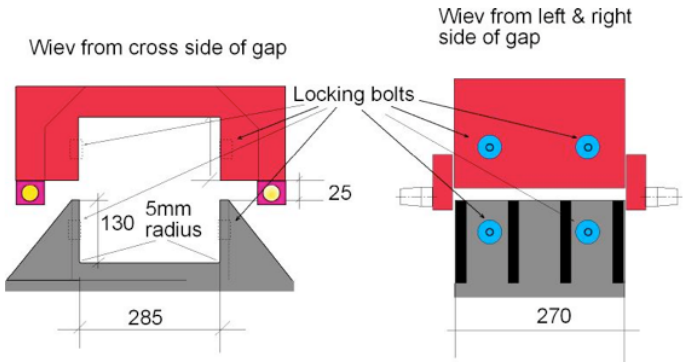

Figure 12: Illustration of sample holder with dimensions

Horizontal and vertical displacement were recorded during the shear tests by LVDT´s, while horizontal and vertical loads were measured by a load cell.

4.3 Preparation of samples

Drilled cores with a diameter of 94 *mm* were extracted from Kalhovd dam, an Ambursen dam owned by Statkraft. The extracted core samples went through both concrete and rock in order to capture the rock-concrete interface, where sliding normally is assumed to occur. The core samples are assumed to represent the rock-concrete interface in the dam. The core samples were extracted from different buttresses of the dam, Sample 1 to 4 is extracted from buttress number 23, 7, 4 and 6, respectively. See Appendix G for drawings of the dam. The samples have different surface roughness, as the surface roughness is natural and not manipulated. During

drilling, some of the bond between rock and concrete broke, and it could be seen on some samples that bonding was not present due to weathering. Therefore, to be able to have similar test conditions, the rock and concrete was separated such that none of the samples had bonding in the interface.

To obtain their wet natural condition, the core samples were stored in water until the samples were prepared for shear testing. Not all the samples were suitable for shear testing, as some of the core samples were broken or had bad interfaces. The core samples which had good enough interface and enough rock/concrete length, were chosen as test specimens. As a result, four of the core samples were chosen and prepared for shear tests. Not all the interfaces of the samples were perfectly mated, as seen in Figure 17. This is due to weathering or that the samples were damaged during extraction or preparation.

The core samples did not have horizontal interfaces, but an inclined interface as seen in Figure 13.

Figure 13: A typical inclined surface (this is the rock part from one core)

Therefore, to align the interface in the horizontal shear plane, the samples were cut in the same angle *a* as the interface, as illustrated in Figure 14.

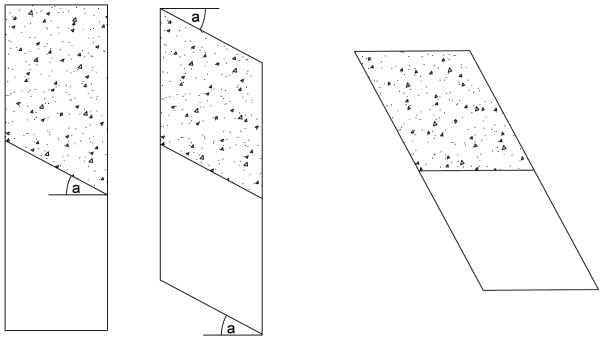

Figure 14: Illustration of how the samples were cut to make the joint horizontal

The angle *a* between the interface and horizontal plane was different for the test samples, which resulted in different surface areas where the normal load was applied, as seen in Table 7.

Table 7: Interface angle a, and corresponding surface area

Sample	Angle, *a* (°)	Surface area (mm^2)
1	32.65	8240
2	27.79	7840
3	20.50	7400
4	26.90	7780

This surface areas were calculated based on assumptions that the whole surface of the interface was intact.

Tree sticks were glued to both the rock and concrete part of the samples to keep them together during the preparation, and to align the joint in the middle of the test sample. After the joints were aligned horizontally, the samples were encapsulated with rapid hardening concrete inside steel boxes with the same size as the sample holder in the test apparatus, as seen in Figure 15.

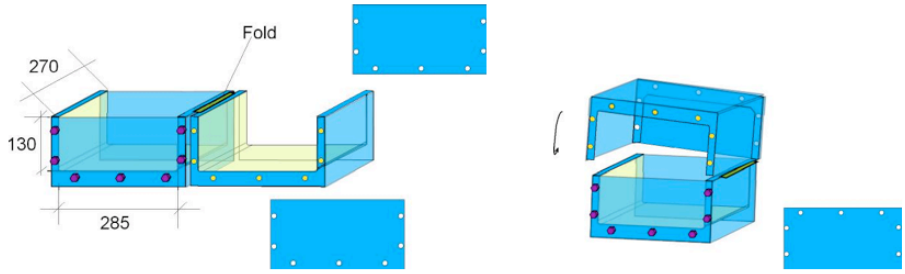

Figure 15: Illustration of steel frames used to encapsulate the core samples

Fist, the rock parts of the samples were encapsulated and left to harden for one day before the concrete part was encapsulated and the steel box was closed. The concrete cured for another five days before the samples were taken out of the steel frames, ready for testing. See Figure 16.

Figure 16: A sample during encapsulation of the rock part, and a sample that is ready for testing

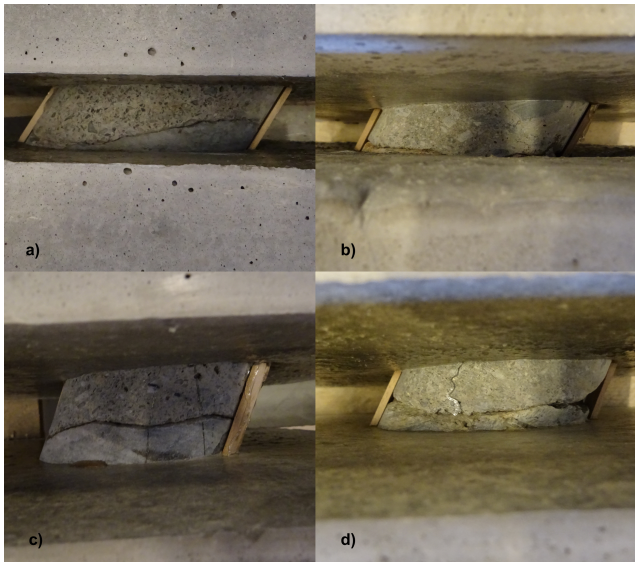

Figure 17: The interface of a) Sample 1 b) Sample 2 c) Sample 3 and d) Sample 4

4.3.1 Material properties

Splitting tests were performed to obtain the tensile strength of the samples. The tests were performed by NORUT in Narvik, according to the ASTM standard D3967-16 (ASTM, 2016). Three tests were carried out for concrete and nine tests were carried out for rock. Two of the tests for concrete, and one of the tests for rock were not performed correctly, therefore, these values were excluded. An average value for the correctly performed tests are used in this thesis.

The compressive strength and basic friction angle were tested in the COMPLAB at LTU. Uniaxial compressive tests on cylinders were performed to find the compressive strength for the core samples. Three tests were carried out for both rock and concrete. The uniaxial compressive strength for rock was performed according to the ASTM standard D3148-02 (ASTM, 2002), while the tests for concrete was performed according to the ASTM standard C39/C39M-03 (ASTM, 2003). One of the compressive tests on rock were not performed correctly, and is therefore not considered. There were big variations between the two values for the compressive strength for rock, so the average value may not be a reliable value. The compressive strength for concrete is normally tested on cubes, not cylinders. Therefore, the uniaxial compressive strength obtained from concrete cylinders is converted to the uniaxial compressive strength for cubes. The uniaxial compressive strength from cylinders is 0.8 times the strength from cubes. An average of the cube strengths is used as the compressive strength for concrete.

The basic friction angle for both rock and concrete were found by performing tilt tests on dry disk samples. The tilt test were performed according to the procedure for disk samples as described by Alejano et al. (2012). The basic friction angle represents the friction angle on smooth surfaces without roughness.

The density for both rock and concrete was calculated by using the area and weight of the samples that were used for the uniaxial compressive tests.

Test results and photos from the splitting test, uniaxial compressive test and tilt tests can be found in Appendix A, along with calculations of elastic moduli for rock and concrete. The properties of the rock and concrete is presented in Table 8.

Table 8: Rock and concrete properties for core samples

	Compressive strength (MPa)	Tensile strength (MPa)	Basic friction angle (°)	Density (kg/m^3)
Rock	86.7	10.4	29	2695
Concrete	41.2	4.0	36	2354

4.4 Procedure for shear tests

All shear tests were performed with a shear rate of 0.5 *mm/s* and a maximum shear displacement of 15 *mm*. A normal stress of 0.5 *MPa* was chosen for all four samples, as this normal stress is a typical level of normal stress found in the buttresses of the dam of 5.0 – 6.0 *m* height. Since only four samples were available, the same normal stress were applied on all samples to be able to compare the different test results. The applied normal load was calculated for each sample based on the areas in Table 7. One shear test was performed for each sample. The reason for this is that the shear capacity for dam Kalhovd is investigated, and the shear capacity for the samples will decrease for each performed shear test, as the surface is crushed and damaged during the tests.

After the samples were placed in the sample holder, the tree sticks were removed from the interface by using a saw. The upper part of the sample holder was lowered until the upper surface of the sample was just in contact with the sample holder. The sample was then clamped with bolts from the side to ensure that the sample could not move inside the sample holder.

The shear tests were monitored by ARAMIS measuring system, which provided accurate measurements of the deformation, displacements and surface strain of the samples during the shear tests. The ARAMIS system can track the movement of any points on the surface with a resolution up to 100^{th} of a millimeter. Thus, this system can be used to check the correctness of the LVDT's measuring the stroke on the shear test apparatus. The test set up and ARAMIS monitoring set up can be seen in Figure 18.

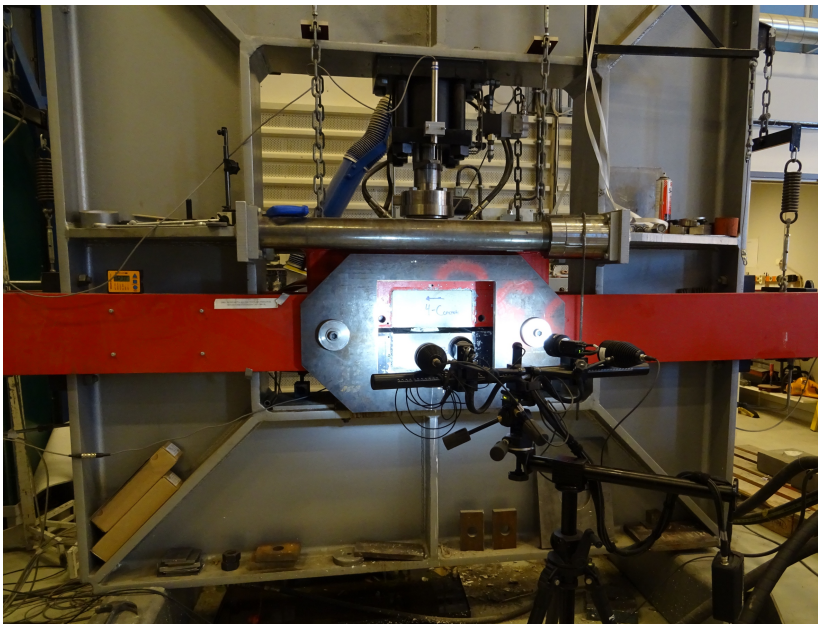

Figure 18: Test set up during shearing and ARAMIS monitoring system

4.5 3D scanning of surface roughness

The surface roughness can vary a lot between the different samples, therefore, to quantify the roughness, optical scanning was applied on the samples. The surfaces were scanned both before and after tests with optical scanning. As mentioned in Chapter 2, Grasselli states the importance of three-dimensional surface roughness when considering the shear capacity of an interface. To be able to apply the models based on three-dimensional surface roughness characteristics, the surfaces must be scanned before the shear tests to be able calculate the 3D roughness parameters that is needed as input. In addition, the samples were scanned after shearing to be able to compare the surfaces before and after shearing to see how much of the surface that were damaged and crushed during the shear test.

The scanning was performed with the system ATOS Compact Scan 5MP, which makes it possible to digitize the entire surface in 3D. The scanning was performed by the company Swerea Seacomp. Four markers were placed on each sample to organize the point clouds in a global coordinate system after scanning. Both the upper and lower part of the samples, concrete and rock, respectively, were scanned. After scanning, the surfaces were depicted as point clouds. The density of the point clouds made it possible to get an accuracy of 0.2 – 0.3 mm of the measured objects. The set up for scanning can be seen in Figure 19.

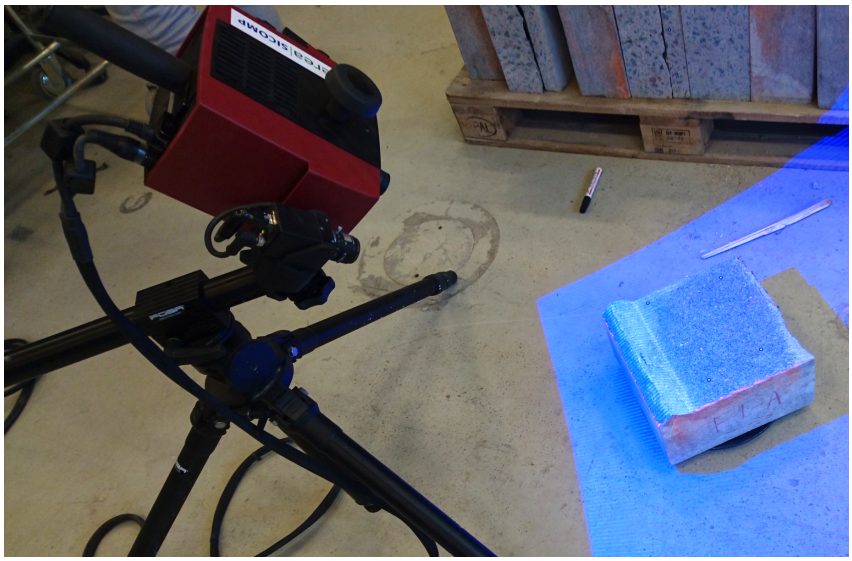

Figure 19: Scanning of surface with ATOS 5MP. (this is a sample from another test series that were conducted at LTU in the same period)

The data clouds were aligned so that the shear plane was in the horizontal plane and the shear direction was along the x-axis. The data clouds were then used to calculate the quantitative three-dimensional roughness parameters developed by Grasselli (2001) and used by others in several models presented in section 3.2.

4.6 Quantification of 3D roughness parameters

The data clouds from the scanning were used to obtain the 3D roughness parameters A_0, C *and* θ^*_{max}. This was done by using the program MATLAB (The Mathworks Inc., 2016) and the codes that were used to quantify the 3D roughness parameters in the program was provided by Fredrik Johansson. See Appendix E for the original MATLAB codes and a more detailed explanation of the changes made on the code. First, the codes were adjusted to fit the Kalhovd samples. The first step was to regenerate the surfaces from the data clouds with a resolution of 0.3 by 0.3 *mm*. Originally, Johansson (2009) regenerated the surfaces with a resolution of 0.5 *mm* by 0.5 *mm*, but an accuracy of 0.3 *mm* by 0.3 *mm* was chosen instead, as the scanner resolution makes this possible, and this is the accuracy used by Grasselli (2001). The grain scale is assumed to be 0.3 *mm*, which is the resolution of the regenerated surface. Then, normal vectors, $\mathbf{n}_i$ for each element in the 0.3 mm by 0.3 mm grid were generated and the shear direction vector, **t**, was defined. The shear direction was along the x-axis as described in section 4.5, hence, **t** = [1 0 0] or [-1 0 0], depending on how the samples were orientated during scanning. The apparent dip angle, θ^*, was calculated for each element with Equation 59.

$$\cos(90 - \theta_i^*) = \frac{|n_i \cdot t|}{|n_i| \cdot |t|} \tag{59}$$

The apparent dip angles were then sorted in descending order in a vector. The area for each element in the grid facing the shear direction was calculated, and a vector that described the cumulative area for the grid based in the shear direction, was created. The apparent dip angles on the x-axis were plotted against the contact area on the y-axis. This is the red curve named "Scanned" in Figure 20.

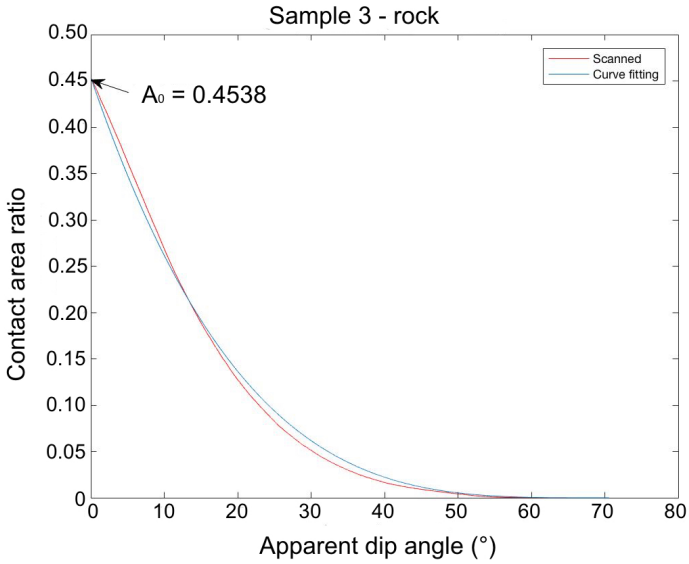

Figure 20: Relation between contact area ratio and apparent dip angle

The maximum possible contact area ratio, A_0, is the sum of the contact areas with an apparent dip angle greater than 0 °, and is found by reading the curve as shown in Figure 20. The maximum apparent dip angle, θ^*_{max}, can easily be found in the vector where the angles are sorted with a descending order, or it can be found by reading the curve. The data from the red curve were used as an input for regression analysis in Microsoft Excel to obtain the roughness parameter, *C*. Nonlinear least-squares regression was performed by using the Solver add-inn in Excel. As suggested by Tatone and Grasselli (2009), the value of *C* was altered in Equation 37 to minimize the sum of squares of residuals, given by Equation 60.

$$SS_{residuals} = \sum \left(A_{\theta^*_{calc.}} - A_{\theta^*_{measured}}\right)^2 \tag{60}$$

The blue curve in Figure 20 named "Curve fitting" is the contact area calculated with Equation 37 with the obtained parameters, plotted against the apparent dip angles. A good match between the curves indicates that the obtained parameters are well suited to describe the surface roughness of the samples. See Appendix D for the curves used to determine the parameters for the samples. The "Curve fitting" curve corresponds to the curve in Figure 21.

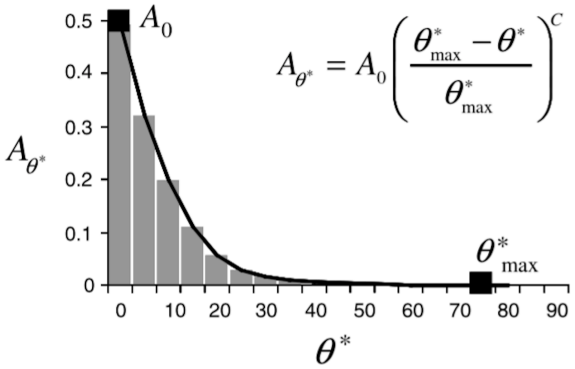

Figure 21: Curve based on calculations with Equation 37.

The area under the curve in Figure 21 was given by Tatone and Grasselli (2009) as shown in Equation 61.

$$\int_0^{\theta^*_{max}} A_0\left[\frac{\theta^*_{max} - \theta^*}{\theta^*_{max}}\right]^C d\theta^* = -A_0\left(\frac{\theta^*_{max}}{C+1}\right) \times \left(1 - \frac{\theta^*}{\theta^*_{max}}\right)^{C+1}\Bigg|_0^{\theta^*_{max}} = A_0\left(\frac{\theta^*_{max}}{C+1}\right) \quad (61)$$

As described by Tatone and Grasselli (2009), the roughness parameter, C, is not suitable to describe the surface roughness. However, a strong correlation between the ratio θ^*_{max}/C and the surface roughness were found by Grasselli et al. (2002a). As the parameter $\theta^*_{max}/(C+1)$ found in Equation 61 is very similar to the ratio θ^*_{max}/C, it was proposed by Tatone and Grasselli (2009) that $\theta^*_{max}/(C+1)$ could replace the ratio θ^*_{max}/C as the parameter used to express the surface roughness. In some cases, the parameter A_0 could vary in different directions (not close to 0.5), and should then be included to describe the surface anisotropy. In this case, Tatone and Grasselli (2009) proposed that $2A_0(\theta^*_{max}/(C+1))$ is used to express the surface roughness. This is simplified to $\theta^*_{max}/(C+1)$ when A_0 equals 0.5.

For the Kalhovd samples, the expression $2A_0(\theta^*_{max}/(C+1))$ were chosen to represent the surface roughness, since some of the contact area ratios were closer to 0.4. The results obtained from

the scanning's of concrete and rock surfaces can be found in Table 9. All the parameters are calculated based on the scanning's before the shear tests, except the maximum apparent dip angle after the tests, $\theta^*_{max,post}$, and the average apparent dip angle after shear tests, $\overline{\theta^*}_{post}$, which are calculated based on the scanning's conducted after the shear tests.

Table 9: The results from 3D roughness analysis of the Kalhovd samples with 0.3 mm accuracy

Sample	A_0 [-]	C [-]	θ^*_{max} [°]	$\theta^*_{max,post}$ [°]	$\overline{\theta^*}$ [°]	$\overline{\theta^*}_{post}$ [°]	$2A_0\left(\frac{\theta^*_{max}}{C+1}\right)$ [-]
1-R	0.445	4.889	76.27	69.62	12.19	12.11	11.53
1-C	0.434	4.685	71.37	71.19	11.78	10.89	10.90
2-R	0.415	6.347	77.68	79.09	10.56	9.41	8.77
2-C	0.429	6.821	81.87	67.91	10.19	9.58	8.98
3-R	0.454	3.601	70.53	71.58	15.01	14.74	13.89
3-C	0.459	4.315	84.43	80.63	15.49	10.47	14.60
4-R	0.485	3.904	68.48	73.76	12.84	12.74	13.53
4-C	0.495	3.457	69.00	71.06	14.59	13.52	15.00

Ideally, the 3D roughness parameters for rock and concrete for each sample should be equal if they were perfectly mated before the tests. However, as seen in Table 9, there are some variations in the parameters calculated for the rock surface and the concrete surface for each sample. There may be various reasons for this. First, the samples may not be perfectly mated. It was observed that some of the surface on the samples were damaged, especially at Sample 4 (see Appendix C). In this case, the rock and concrete surfaces will have a different surface roughness and produce different parameters. For further analysis of the results, an average of the parameters calculated for rock and concrete are used, as presented in Table 10. As seen in Table 9, only half of the maximum apparent dip angles decreases, and the rest of them increases after shearing. The reason for this is most likely that for some of the samples, the surface broke and parts fell off. This broken surface might have asperities that are steeper than the asperities on the surface before shearing.

Table 10: Average values of 3D parameters between rock and concrete surfaces used in calculations

Sample	A_0 [-]	C [-]	θ^*_{max} [°]	$\theta^*_{max,post}$ [°]	$\overline{\theta^*}$ [°]	$\overline{\theta^*}_{post}$ [°]	$2A_0\left(\frac{\theta^*_{max}}{C+1}\right)$ [-]
1	0.440	4.787	73.82	70.41	11.99	11.50	11.22
2	0.422	6.584	79.76	73.50	10.38	9.50	8.88
3	0.457	3.958	77.48	76.11	15.25	12.61	14.25
4	0.490	3.681	68.74	72.41	13.72	13.13	14.27

4.7 Test results

A summary of the results obtained from direct shear tests is shown in Table 11. The table shows the applied normal load, N, the applied shear force at peak shear strength, V_{max}, the total shear displacement, δ_{tot}, the applied normal stress, σ_n, the peak shear strength, τ_{peak}, the shear displacement at peak shear strength, δ_{peak} and the peak friction angle, ϕ_{peak}. All the graphs obtained from the shear tests are found in Appendix B, while photos from the shear tests are found in Appendix C.

Table 11: A summary of the results obtained from direct shear tests

Sample	N (kN)	V_{max} (kN)	δ_{tot} (mm)	σ_n (MPa)	τ_{peak} (MPa)	δ_{peak} (mm)	ϕ_{peak} (°)
1	4.12	12.22	15	0.5	1.48	0.61	71.33
2	3.92	8.91	15	0.5	1.13	0.79	66.13
3	3.70	10.48	15	0.5	1.42	0.76	70.60
4	3.89	9.24	15	0.5	1.12	0.50	65.75

The peak shear strength is consequently found from the first peak in the graph, even though the shear stress is higher for Sample 2 and 4 later in the diagram, as seen in Figure 22.

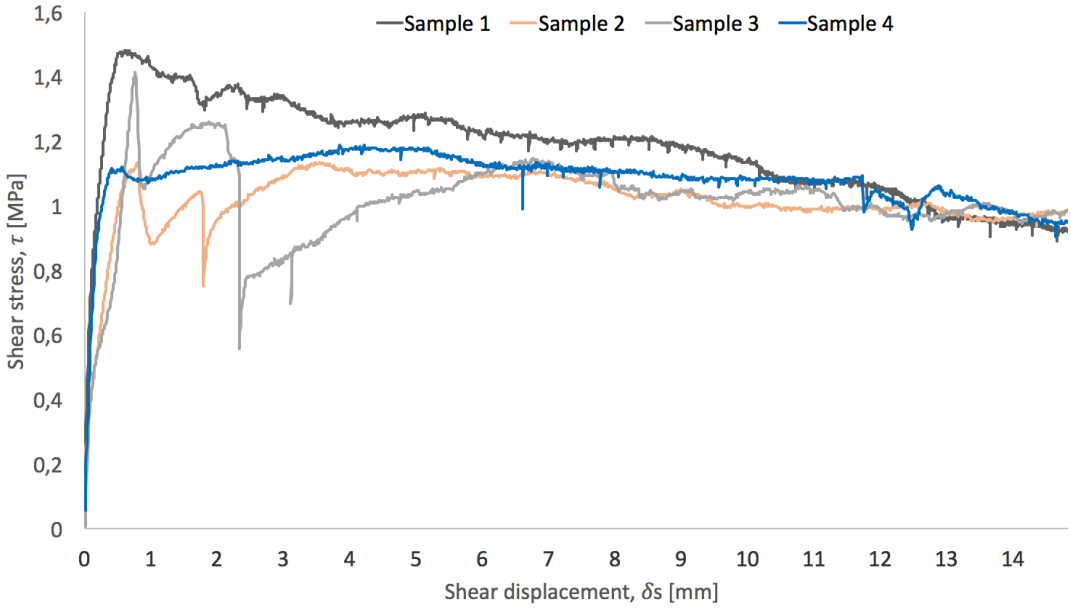

Figure 22: Shear stress - shear displacement curves for all samples

The reason for selecting the first peak in the graph as the peak shear strength, is that the dam already has been sliding some millimeters when the maximum shear strength in these shear tests are reached, and that is not acceptable when looking at the sliding stability of a dam. However, the dam will always have some small movements before the whole surface roughness is contributing to shear strength, therefore, a small displacement will always be present before the first peak is reached. Some of the shear displacement may also be due to displacement of the sample inside the test apparatus or movements in the apparatus.

4.8 Analysis of test results

Two of the samples resulted in a higher peak shear strength than the other two, this may be due to rougher surfaces on the samples which had the highest shear strength. As mentioned in section 4.6, the expression $2A_0(\theta^*_{max}/(C+1))$ could be used to express the surface roughness of the samples. One would expect Sample 1 and 3 to have a higher amount of surface roughness than Sample 2 and 4, since Sample 1 and 3 had the highest values of peak shear strength. However, by comparing the values in Table 9 with the shear test results, one can see that Sample 4 is not following this trend, as Sample 4 have the lowest peak shear strength, but the highest amount of surface roughness according to the expression for surface roughness. The reason for this is most likely because the sample had a broken interface which was not in contact. Visual inspection showed that Sample 4 had a broken surface and the sample was not perfectly mated.

The edges of the sample were broken and not in contact, see Appendix C for photos. As a result, only the part in the middle of the surface contributed to shear strength, and this surface was not as rough as the broken edges. Hence, the rough, broken edges resulted in a high amount of surface roughness according to the expression, but did not contribute to shearing since the surface was not in contact at all places. If just considering the surface that were in contact, the expression would most likely result in a lower value for Sample 4, which indicates a smoother surface and lower shear strength. According to the expression for surface roughness, Sample 3 had higher amount of surface roughness than Sample 1, but the peak shear strength for Sample 3 was somewhat lower. One reason for this could be that Sample 3 had a greater gap between the concrete used to encapsulate the samples, as seen by the photos and illustrations in Appendix C and Appendix D. As a result, a smaller part of the sample was encapsulated and the force were applied in a greater distance from the interface for Sample 3. This may have caused a greater moment acting on the sample, which in turn leads to a reduction in peak shear strength. It is therefore important that the samples are encapsulated to the same extent, as different degrees of encapsulation can affect the test results.

As seen in Figure 22, Sample 1 to 3 have a small peak on the graph which indicates where all the surface roughness is mobilized and the sample have started to slide. Sample 4 have a flat curve and looks more like a sample with a smooth interface without any surface roughness. As Sample 4 seems to differ from the other samples in several ways, the result might not be as reliable as the other tests results.

The asperities with the steepest inclinations in the shearing direction was expected to shear or crush, therefore, the maximum apparent dip angle, θ^*_{max}, was expected to decrease after shearing due to smoothening of the damaged asperities. As seen in Table 9, only half of the maximum apparent dip angles decreases, and the rest of them increases after shearing. However, by looking at the average apparent dip angles in Table 9, the average asperity angle decreases after shearing. This verifies that the steepest asperities facing the shear direction shears or crushes during the shear tests, and that the surface is smoothed out. The maximum apparent dip angle may increase due to locally broken surfaces, but when looking at the whole surface, the surface is smoother than before the test. This indicates that the average apparent dip angle may be better to illustrate that the steepest asperities are involved in shearing, thus, sheared off or crushed. A rough surface after shearing indicates that tensile failure plays an important role in the shear behavior (Grasselli, 2001, Zhang et al., 2016). Thus, the increase in

maximum apparent dip angle for some of the surfaces, indicates that tensile failure was one of the failure modes occurring during the shear tests.

If comparing the amount of steep asperities on the surfaces in Figure 23, Sample 1 and 3, which had higher values of peak shear strength, has a larger amount of steep asperities than Sample 2, which had lower peak shear strength. This shows that the larger amount of steep asperities, the larger amount of the surface contributes to shearing, and higher shear capacity is obtained. Sample 4 has a large amount of steep asperities, but as discussed earlier, they are not in contact and the area will therefore not contribute to shear strength.

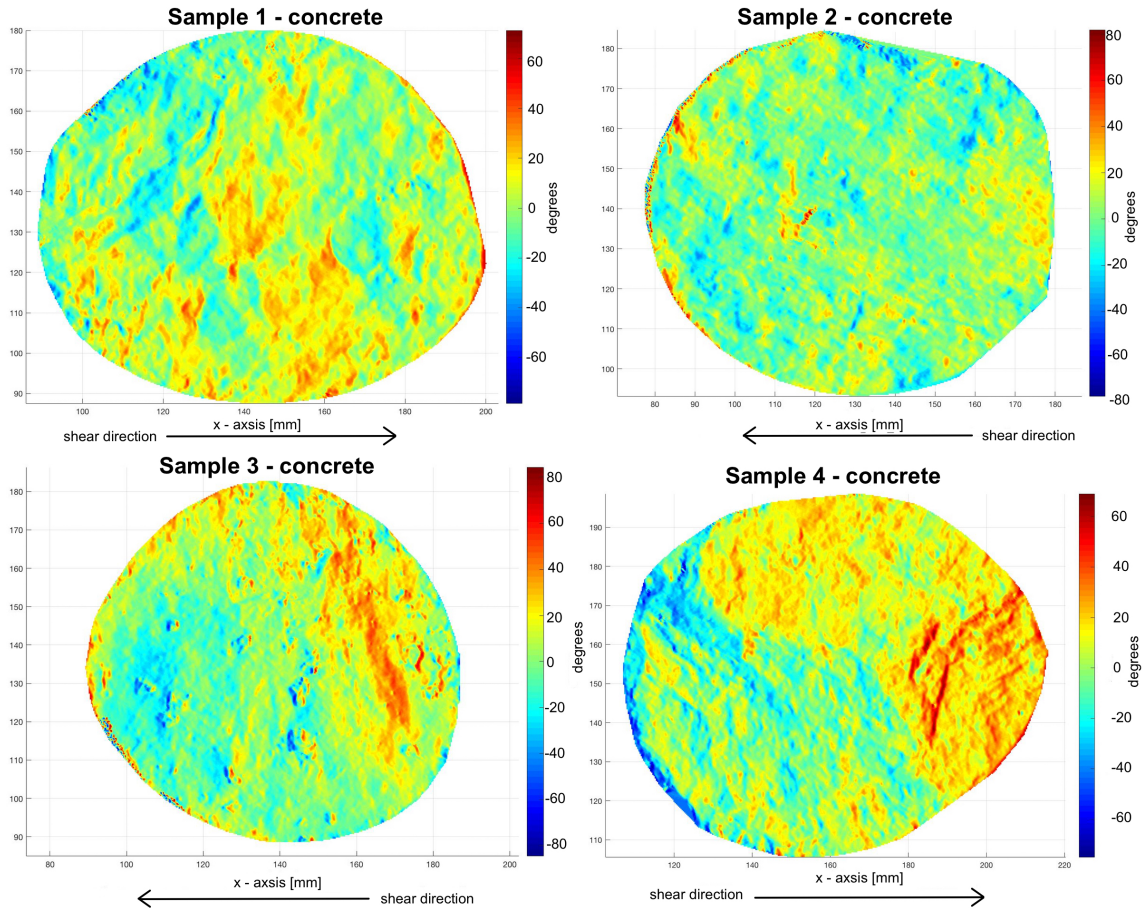

Figure 23: Inclination of asperities in shearing direction (apparent dip angles in degrees) of Sample 1 to 4

During the shear tests, the load cannot be applied in the interface, but must be applied higher up on the sample. This results in a moment that will act on the samples. Due to the moment, the asperities can fail due to tensile failure instead of shear failure, and more of the surface roughness will be crushed or damaged. This can reduce the peak shear strength of the samples. The moment will decrease with increasing size of the test sample, and will not affect the results

that much for bigger samples. However, it is uncertain how much the moment will affect the results when conducting shear tests on samples with a diameter of 94 *mm*, but the obtained results might be higher than the shear capacity of the dam. General scale effects can also be a source of error in these shear tests. As discussed in subsection 2.3.6, small samples will not always capture the weak zones. Hence, the results obtained from the shear tests may be too high compared to the real shear capacity of the dam. However, there are uncertainties regarding the scale effect and further research is necessary to understand the scale effects.

5 Study of the accuracy of shear strength models

By applying existing shear strength models on the Kalhovd samples to estimate the shear strength, and study the results from the shear tests, the accuracy and applicability of different models can be studied. When applying different models on the samples, Sample 4 is excluded. As discussed, the surface is rough, but not all the surface was in contact during under shearing. Thus, it is excepted that the estimated shear strength values would be higher than the shear strength values obtained from the test and it would be wrong to include Sample 4 when studying the accuracy.

5.1 Applying shear strength criteria on Kalhovd samples

A selection of the existing models presented in Chapter 3 are applied on the Kalhovd samples. Three of the most known criteria, Mohr-Coulomb, Patton and Barton, in addition to three of the models that can incorporate the 3D surface roughness; Grasselli, Johansson and Xia, are applied on the samples. The goal is to study their applicability on natural surfaces and compare their capability to estimate the shear strength in an accurate way. The reason for not including all the proposed models is due to lack of necessary input parameters and time limitations.

The basic friction angle for both rock and concrete were found by performing tilt tests. The basic friction angle for rock is usually used as an input parameter since all the models originally were developed for rock joints. The basic friction angle for rock-concrete interfaces will be somewhere between the value for rock and the value for concrete, but there are no standardized methods for determining the basic friction angle for rock-concrete interfaces based on the basic friction angles from rock and concrete. One way can be to use the average value between rock and concrete. However, according to Westberg and Johansson (2016), the basic friction angle for rock-concrete interfaces, $\phi_{b,r\text{-}c}$, can be assumed to have a mean value of 35 ° with a standard deviation of 1.75 °. Therefore, the mean value of 35 ° is used as the basic friction angle for the rock-concrete interface at Kalhovd instead of the average basic friction angle between rock and concrete obtained from tilt tests.

5.1.1 Mohr-Coulomb

Since the rock and concrete part of the samples were separated, no bonding was present in the interface. Hence, no cohesive forces were present. The best option to determine the value for friction angle is to conduct shear tests on samples extracted from the rock-concrete interface in dams, as this will give the most realistic values. The peak friction angle can be back-calculated from the shear tests by using Mohr-Coulomb, but the estimated shear strength will then be the same as the test result. For now, the peak shear strength will be estimated without using the test results, to see how this criterion works if no samples are available. One possibility is to use a value for the rock type found in the literature. According to the bedrock map at NGU (NGU, 2017), the rock-type at Kalhovd dam is "*Kataklasite, mylonite, formed essentially by the rocks of Gøystkomplekset, locally with rust zones, the rocks are rocky*". This is not one of the typical rock types like granite or gneiss which are found in literature. However, when studying the rock visually, the rock looks like gneiss, as seen Figure 13, and the material properties of the samples presented in Table 8 are in accordance with typical values for gneiss (SINTEF). By assuming that the rock is similar to gneiss, a typical value for the peak friction angle for gneiss in sound conditions is $\phi_p = 59.5$ ° (Novák, 2007). Sound conditions is when there is no significant degree of discontinuities or weathering of the rock. When concrete dams are built, the rock foundation is normally prepared, and weathered rock or rock with discontinuities are removed in order to obtain sound conditions.

If the friction angles are not documented by tests, NVE (2005) gives values for the maximum allowable friction angle that can be used in the calculations. The value can be 40-50 °, depending on the conditions in the sliding plane. For hard rocks, with a rocky surface, the maximum allowable friction angle is 50 °, and this is assumed to be the case at dam Kalhovd.

The peak shear strength is estimated by using both the value recommended by NVE and the value found in literature. The calculations are done with Equation 8, and the results are found in Table 12.

Table 12: Estimated peak shear strengths with Mohr-Coulomb

Sample	σ_n [*MPa*]	*c [MPa]*	ϕ_p [°]	$\tau_{calc.}$ [*MPa*]	Comments
1-3	0.5	0	59.5	0.85	Literature
1-3	0.5	0	50.0	0.59	NVE

5.1.2 Patton

Patton's model is based on asperities with saw-tooth profiles. The roughness on natural surfaces are irregular, and not formed like saw-tooth profiles. As a result, Patton's model is not suitable to apply on natural surfaces. One possible solution could be to use the average apparent dip angle, $\overline{\theta^*}$, to express the angle, i, of the saw-tooth profile. However, $tan\phi$ is not a linear function and will therefore not capture the effect on shear strength from steep inclined asperities if using an average value of the apparent dip angle. Since the steepest asperities are the one that are involved in shearing and contributes to shear strength, Patton's model will estimate wrong peak shear strengths if the average apparent dip value are used. If considering Sample 1, the average apparent dip angle is approximately 12 °, and if inserting this in the model along with the basic friction angle, the estimated shear strength will only be around 40 % of the peak shear strength obtained from the tests. Both Johansson and Stille (2014) and Xia et al. (2014) have developed models based on Patton's formulation, and created an expression for the dilation angle, *i,* based on the 3D roughness parameters obtained from the scanning's. Thus, Patton's model is more applicable on lab samples with manipulated roughness, and when considering natural surfaces, the models developed by Johansson and Stille (2014) and Xia et al. (2014) would be a better choice if scanning of the surfaces is possible. As a result, Patton's model was not used to estimate the peak shear strength on the Kalhovd samples, since the model only is applicable on saw-tooth asperities. See section 5.1.5 and 5.1.6 for the Johansson's and Xia's models.

5.1.3 Barton's JRC-JCS model

Linear roughness profiles parallel to the shear direction were extracted for each of the samples. The profiles were extracted from the middle of the surface, where the diameter was approximately 10 *cm*, see Figure 24 for example.

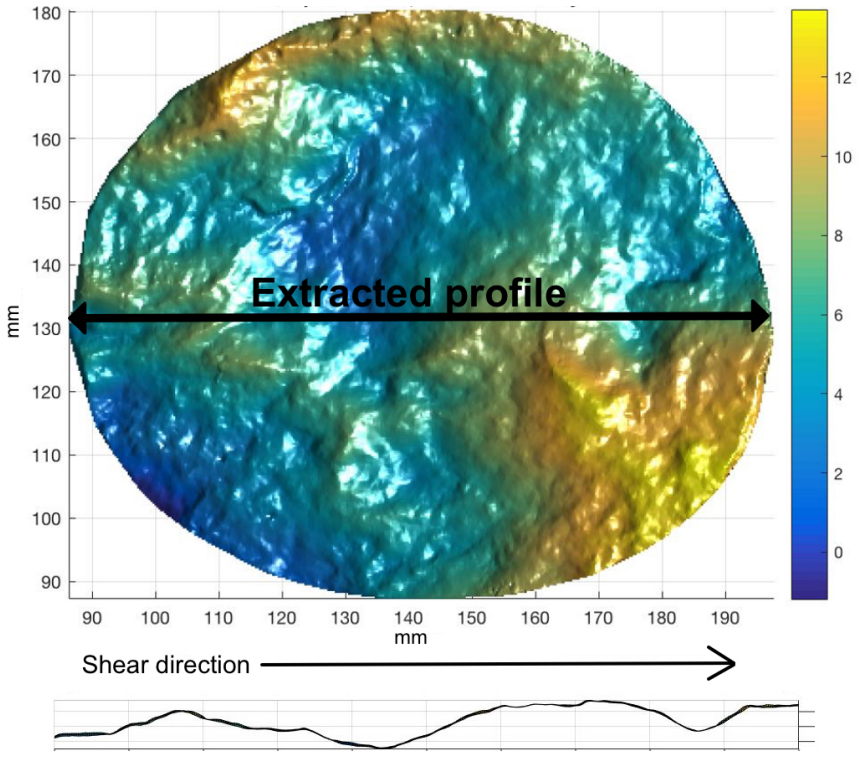

Figure 24: Illustration of where the profiles used for JRC were extracted

The reason for extracting roughness profiles with a length of 10 *cm*, is that the profiles can then be directly compared with the roughness profiles in Figure 6, which are also 10 *cm*. The extracted profiles can be seen in Appendix D. The *JRC* values are found for both rock and concrete surfaces by visual comparison, and an average value between these two surfaces were used in the calculations, as shown in Table 13.

Table 13: JRC values found by visual comparison

Sample	JRC - rock	JRC - concrete	JRC, average
1	16	15	15.5
2	13	13	13
3	16	16	16

Visual comparison is a subjective method where the values are chosen by the author. This can result in different estimated shear strengths, as another person can choose different *JRC* values. In addition, the *JRC* values are based on a single profile, and will not capture the anisotropy in surface roughness. To eliminate the limitation with subjective comparison, the *JRC* was also found by using Grasselli's quantitative expression in Equation 42. The *JRC* values obtained from Grasselli's expression, $JRC_{,G}$, were calculated based on the 3D roughness parameters in Table 16.

If the joints are completely unweathered, the *JCS* will be equal to the unconfined compressive strength, σ_c, of the unweathered rock (Grøneng and Nilsen, 2009). For weathered surfaces, the *JCS* will be lower than the compressive strength of the surface, and a Schmidt hammer can be used to determine the *JCS*. The recommended L-type Schmidt hammer was not available at LTU, and the *JCS* was therefore determined by the compressive strength of the materials. The rock-concrete interface of the samples may not be completely unweathered, but are in these calculations assumed to be unweathered. Since this criterion was developed for rock joints, the criterion does not consider the fact that rock and concrete have different compressive strengths. It would be preferable to estimate the models with the compressive strength for both rock and concrete to see which of the estimated values are the closest to the test results, as surface damage was observed for both rock and concrete after the shear tests. However, due to large uncertainties in the compressive strength for rock, the value is not reliable. Therefore, the lowest compressive strength, which in this case was concrete, was chosen as input parameter, as it is assumed that this material will break first. The values for uniaxial compressive strength for the samples are found in Table 8, and the *JCS* values used to estimate the shear strength are found in Table 14.

Table 14: Compressive strength for rock and concrete, and values for JCS

Sample	$\sigma_{c,rock}$ [*MPa*]	$\sigma_{c,\ concrete}$ [*MPa*]	JCS [*MPa*]
1-3	86.7	41.2	41.2

The estimated shear strength is calculated by using Equation 21 and the estimated values are presented in Table 15.

Table 15: Estimated peak shear strengths with Barton´s JRC-JCS model

Sample	σ_n [*MPa*]	*JRC* [-]	$JRC_{,G}$ [-]	*JCS* [-]	ϕ_b [°]	$\tau_{calc.}$ [*MPa*]	$\tau_{calc,G}$ [*MPa*]	τ_{test} [*MPa*]
1	0.5	15.5	18.5	41.2	35	1.06	1.41	1.48
2	0.5	13.0	16.5	41.2	35	0.86	1.16	1.13
3	0.5	16.0	21.3	41.2	35	1.11	1.98	1.42

5.1.4 Grasselli

One of the challenges using Grasselli's model is that the model originally was developed for rock-rock interfaces. It is therefore a challenge to know if the parameters for rock or for concrete should be used as input parameters. The 3D roughness parameters used in the calculations are average values for both the rock and concrete surfaces, and are found in Table 10. The reason for using an average value is because the surfaces may vary a little and the scanning's may produce different data clouds, and by using the average value, the roughness from both surfaces are considered. The lowest value for tensile strength were used, which in this case was the value for concrete. The reason for this is that the weakest material will most likely be the first to break when the interface starts sliding.

The samples were assumed to have no schistosity, as no schistosity was observed. According to Grasselli (2006), β is 0 if no schistosity is present. This model is only valid within the test range σ_n/σ_c = 0.01 – 0.04 and σ_c/σ_t = 5 – 46. When using the values from concrete for compressive and tensile strength, the following values were obtained: σ_n/σ_c = 0.01 and σ_c/σ_t = 10.2. Both ratios are within the valid range, thus, the model is applicable on the Kalhovd samples.

The peak shear strength is calculated with Equation 41, and the estimated shear strengths can be found in Table 16.

Table 16: Estimated peak shear strengths with Grasselli´s model

Sample	β [°]	A_0 [-]	C [-]	θ^*_{max} [°]	σ_t [MPa]	ϕ_b [°]	$\tau_{calc.}$ [MPa]	τ_{test} [MPa]
1 - $\sigma_{t,conc}$	0	0.440	4.787	73.82	4.04	35	1.41	1.48
2 - $\sigma_{t,conc}$	0	0.422	6.584	79.76	4.04	35	1.15	1.13
3 - $\sigma_{t,conc}$	0	0.457	3.958	77.48	4.04	35	1.98	1.42

5.1.5 Xia

The model proposed by Xia et al. (2014) uses the same input parameters as Grasselli's criterion. The average values between rock and concrete are used for the 3D roughness parameters, and the lowest value, concrete, is used for the tensile strength. See section 5.1.4 for more information about the input parameters. The estimated shear strengths are calculated by using Equation 44, and the results are found in Table 17.

Table 17: Estimated peak shear strength values with Xia's model

Sample	A_0 [-]	C [-]	θ^*_{max} [°]	σ_t [MPa]	ϕ_b [°]	$\tau_{calc.}$ [MPa]	τ_{test} [MPa]
1 - $\sigma_{t,conc}$	0.440	4.787	73.82	4.04	35	1.59	1.48
2 - $\sigma_{t,conc}$	0.422	6.584	79.76	4.04	35	1.09	1.13
3 - $\sigma_{t,conc}$	0.457	3.958	77.48	4.04	35	3.31	1.42

5.1.6 Johansson

The 3D roughness parameters θ^*_{max}, C and A_0 are average values for rock and concrete, same as used in both Grasselli´s and Xia´s models. For the uniaxial compressive strength, the value for the weakest material, concrete, is used. The samples are assumed to be perfectly mated, which is a reasonable assumption since concrete is casted on top of the rock foundation. However, not all the samples were perfectly mated, as some of them had broken surfaces. The degree of matedness was hard to determine, and the samples were therefore assumed to be perfectly mated. For perfectly mated samples, the empirical constant that reflects the degree of matedness, k, is 0. As a result, the last term $(L_n/L_g)^{kH-k}$ becomes 1.

The estimated shear strengths are calculated by using inserting Equation 55 into Equation 46, and the results are found in Table 18.

Table 18: Estimated shear strength values with Johansson´s model

Sample	A_0 [-]	C [-]	θ^*_{max} [°]	σ_{ci} [MPa]	ϕ_b [°]	$\tau_{calc.}$ [MPa]	τ_{test} [MPa]
1 - $\sigma_{ci,conc}$	0.440	4.787	73.82	41.2	35	1.74	1.48
2 - $\sigma_{ci,conc}$	0.422	6.584	79.76	41.2	35	1.25	1.13
3 - $\sigma_{ci,conc}$	0.457	3.958	77.48	41.2	35	3.35	1.42

5.1.7 Comparison of models

Different models were used to estimate the peak shear strength of the three samples. A comparison between the estimated values and the measured peak shear strength can be found in Figure 25.

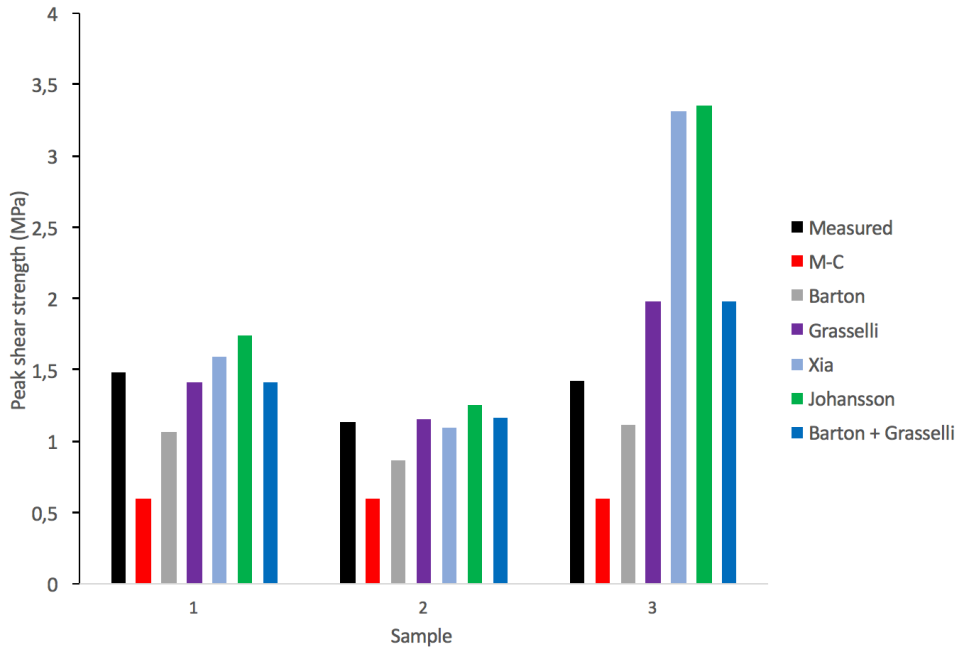

Figure 25: Estimated peak shear strengths using the properties of concrete as input parameters

To compare how good the different models can estimate the peak shear strength for the tested samples, the average estimation error, E_{ave}, was used:

$$E_{ave} = \frac{1}{m}\sum_{i=1}^{m}\left|\frac{\tau_{test} - \tau_{estimated}}{\tau_{test}}\right| \times 100\ \% \qquad (62)$$

Where τ_{test} is the peak shear strength from shear test, $\tau_{estimated}$, is the estimated peak shear strength, and m is the number of direct shear tests.

Table 19 summarizes the estimated peak shear strength and the corresponding estimation errors for the three samples.

Table 19: Comparison among the different peak shear strength criteria

Sample	Measured	M-C (NVE)		Barton		Grasselli		Xia		Johansson		Barton + Grasselli	
	τ_p *(MPa)*	τ_p	*E (%)*	τ_p	*E (%)*	τ_p	*E (%)*	τ_p	*E (%)*	τ_p	*E (%)*	τ_p	*E (%)*
1	1.48	0.59	60.1	1.06	28.4	1.41	4.7	1.59	7.4	1.74	17.6	1.41	4.7
2	1.13	0.59	47.8	0.86	23.9	1.15	1.2	1.09	3.5	1.25	10.6	1.16	2.7
3	1.42	0.59	58.5	1.11	21.8	1.98	39.4	3.31	133.1	3.35	134.9	1.98	39.4
E_{ave} (%)	-		55.5		24.7		15.3		48.0		54.7		15.6

As seen in Table 19, Grasselli's model has the smallest value of average estimation error, while Mohr-Coulomb has the biggest value. This indicates that Grasselli's model is the most suited to predict the peak shear strength for the tested samples, while Mohr-Coulomb is the least suited. Johansson's and Xia's models have almost as high estimation error as Mohr-Coulomb. However, for Sample 3, all the 3D roughness models overestimate the peak shear strength, especially Xia's and Johansson's models. For Sample 1 and 2, the estimation error for these models is relative small compared to the estimation error in Sample 3. The reason for this could be that some of the calculated roughness parameters is not a good fit for Sample 3. Especially the low value of the roughness parameter *C* for Sample 3, seems to influence the estimated shear capacity in Xia's and Johansson's model. Because of the big errors in Sample 3, Xia's and Johansson's models have the biggest average estimated errors among all the 3D roughness models. Mohr-Coulomb's criterion has large estimation errors compared to Grasselli´s model. The guidelines from NVE (2005) gives values for maximum allowable peak friction angle to use in Mohr-Coulomb, if the friction angle is not documented. In this case, the maximum allowable peak friction angle, $\phi_p = 50\ ^\circ$, result in estimated peak shear strengths that are approximately 50 % less than the peak shear strengths obtained from the tests. This makes Mohr-Coulomb's criterion the least suitable to predict the peak shear strengths for the samples. The reason for this is that the peak friction angle obtained from the shear tests, $\phi_p = 69.5\ ^\circ$, is significantly higher than the maximum allowable friction angle. As seen in Figure 25, Barton's model underestimate the peak shear strength for the samples. This corresponds to the findings made by Hong et al. (2008) and Hou et al. (2015). According to Hong et al. (2008), the surface roughness can be underestimated in relative rough profiles, which is the case for the Kalhovd samples. As observed, the two-dimensional roughness profiles are not suitable to describe the contribution from surface roughness on shear capacity, as the profiles underestimates the peak

shear strength. However, if using the $JRC_{,G}$ which is calculated based on 3D roughness parameters, the accuracy of the estimated shear strengths are good. A combination of Grasselli´s expression for *JRC* and Barton's criteria gives approximately the same estimation error as Grasselli´s criterion. This method is therefore as good as Grasselli´s criterion when it comes to estimating the peak shear strength. By using the expression for $JRC_{,G}$, the 3D surface roughness can easily be implemented in Barton's criterion. This might be useful for Ambursen dams, as the buttresses of the dam are so thin that a single roughness profile could be representative for the roughness in the interface of the considered buttress. The surface could be scanned at both side of the buttress to obtain average 3D roughness parameters that represents the roughness in the interface, which can be used to calculate the $JRC_{,G.}$ However, the calculated $JRC_{,G}$ values may not be able to capture the effect from topography, so the method will be most applicable for flat foundations. Overall, the 3D roughness models are generally more accurate than the 2D roughness model, except for Sample 3, where all the 3D roughness models overestimated the shear strength. Hence, the 3D roughness parameters are more suitable to describe the surface morphology and contact area compared to linear surface profiles, which is in accordance with Grasselli's findings. However, the 3D roughness models are more complex and time consuming than models like Mohr-Coulomb, as scanning is required to use the 3D roughness models.

The shear strength models were all developed for rock joints. As a result, the models are not adjusted to consider two different materials like rock and concrete. There are no existing guidelines for how to use the models for the rock-concrete interface for dam foundations. What parameters to use depends on which of the material that fails. This is not always the weakest material, as this depends on the location and angle of the asperities, and the normal stress. For the interfaces of the Kalhovd samples, the failure is often on both rock and concrete. In such cases, it is hard to determine what value to use. In this thesis, the weakest material, concrete, was used to determine the values for compressive and tensile strength. However, the lowest value may not always be correct to use, as the failure will not always happen in the weakest material. For concrete dams, the failure plane can go through both rock and concrete, as this is dependent on the angle and location of asperities and the acting normal stress. It is recommended to make a guideline for how to determine the input parameters when considering rock-concrete interfaces, but more research is necessary to do that.

5.2 Sensitivity analysis of the basic friction angle

Due to the uncertainties regarding the basic friction angle in rock-concrete interfaces, a sensitivity analysis of the basic friction angle was performed to see how the basic friction angle influences the different shear strength models. When estimating the shear strengths in the previous section, the proposed value of 35 ° was used. The basic friction angles for rock and concrete was 29 and 36 degrees, respectively. The basic friction angle for the rock-concrete interface will most likely be somewhere in-between the value for rock and concrete. To see how the basic friction value influences the shear capacity in different models, the shear capacity was estimated with four different models with basic friction values varying from 29 to 36 degrees. The following figures shows the estimated shear strengths as a function of basic friction value for Sample 1 to 3.

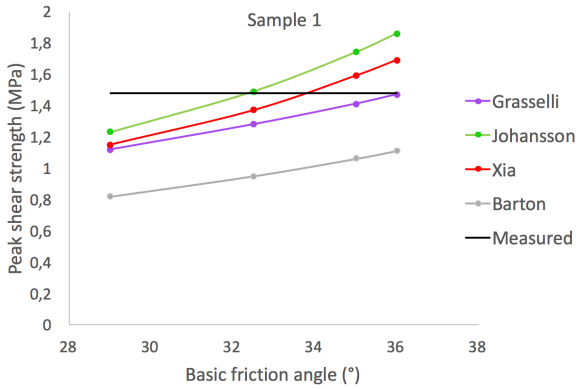

Figure 26: Estimated shear strengths as a function of the basic friction angle for Sample 1

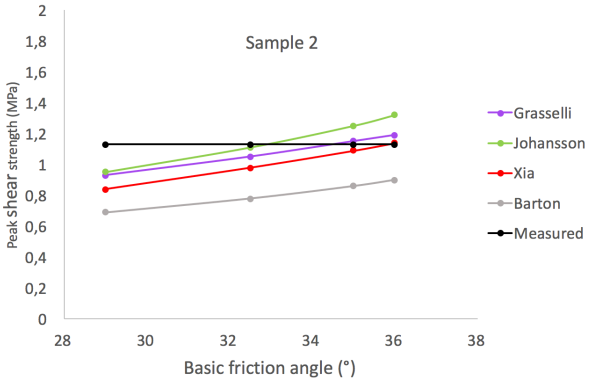

Figure 27: Estimated shear strengths as a function of the basic friction angle for Sample 2

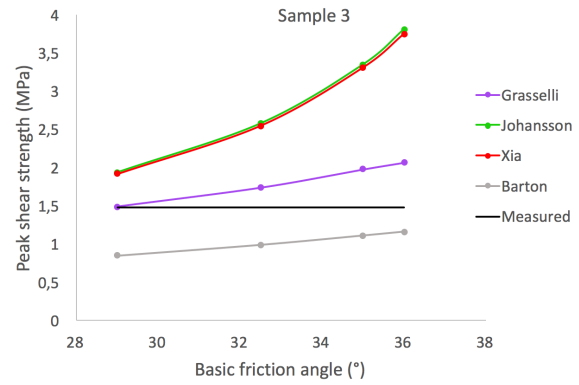

Figure 28: Estimated shear strengths as a function of the basic friction angle for Sample 3

As shown in Figure 26, 27 and 28, there are big variations in the estimated shear strengths for different basic friction angles. The estimated shear strengths with Barton's and Grasselli´s models have almost a linear increase, while the estimated shear strengths with Johansson's and Xia's models increases more rapidly. The reason for this is that the expression for the dilation angle give higher values in Johansson's and Xia's models than for Barton's and Grasselli's models for the same sample. Since the function of tangent increases more rapidly for high values, the same increase in the basic friction angle will cause a higher value of shear strength for Johansson´s and Xia´s models than for Barton's and Grasselli's models. The basic friction angle will therefore be more important in Johansson's and Xia's models, as a wrong basic friction angle could affect the result more than for Barton´s and Grasselli´s models. If considering Sample 3 in Figure 28, a change in the basic friction angle from 29 degrees to 36 degrees will increase the estimated shear strengths with 95 % for Johansson's and Xia's models, while Grasselli and Barton's models only increases the estimated values about 40 %. Hence, Xia's and Johansson's models are more sensitive for changes in the basic friction angle. In addition, samples with a high amount of surface roughness will be more sensitive for changes in the basic friction angle than smooth surfaces, due to higher values of dilation angle.

As seen in the sensitivity analysis based on the test samples, the basic friction angle is an important input parameter when estimating the peak shear strength with models. Rough surfaces, and models where the expression for dilation angle calculates high values, are more sensitive for changes in the basic friction angle. The estimated shear strengths can both underestimated and overestimated the test results within the range of basic friction angles, thus, it is important to determine the correct input value. However, no standard method to determine the basic friction angle in rock-concrete interfaces is developed. If the basic friction angle for the rock-concrete interface is unknown, a conservative approach will be to use the lowest basic friction angle of rock and concrete.

5.3 Accuracy of 3D roughness models based on shear tests conducted by Grasselli

When studying the accuracy of different models in section 5.1, only three samples were considered. If there was a bad match between measured and estimated shear strengths for one of the samples, it may have affected the average estimation error significantly. Therefore, it was decided to apply the models on previous conducted shear tests to verify the accuracy. Grasselli (2001) conducted 37 shear tests on different types of rock joints. These tests have been used by several authors to verify and study the accuracy of proposed shear strength models. Linear surface profiles from the samples are not available, so Barton's JRC-JCS model will not be applied on the samples.

Both Grasselli and Egger (2003) and Xia et al. (2014) estimated the peak shear strengths of the samples by using Grasselli's model. Due to differences in the estimated shear strengths presented by the authors, the shear strengths were estimated again. In addition, Johansson and Stille (2014) estimated the peak shear strength of the samples by using Johansson's model. Some of the 3D roughness parameters used to estimate the peak shear strength with Johansson's model was not the same as used by Grasselli and Egger (2003) and Xia et al. (2014). Therefore, in order to compare the models on the same basis, all the shear strengths were estimated all over by using the input parameters provided by Grasselli and Egger (2003). The shear strengths were estimated by using Grasselli's, Xia's and Johansson's models and were calculated with Equation 41, 44 and 55, respectively. The estimated shear strengths can be found in Appendix F. The average estimation error presented in Table 20 was calculated by using Equation 62.

Table 20: Average estimation errors for 3D roughness models applied on Grasselli (2001)'s samples

Considered samples	Grasselli	Xia	Johansson
All samples	11.2 %	20.3 %	35.2 %
Samples with β=90° excluded	10.5 %	14.4 %	32.2 %

Xia's and Johansson's models do not include the effect from schistosity and the samples with β =90 ° seems to increase the average estimated error for these two models. Therefore, an additional average estimated error was calculated by just considering samples with β=0 °. As seen in Table 20, is the error less for all the models, especially for Xia's model, which indicates

that all models will predict the peak shear strength for samples without schistosity more accurate. Grasselli's model gives the best estimated shear strengths, followed by Xia's and Johansson's models. This is in accordance with the results in section 5.1. One of the reasons for the high estimation error for Johansson´s model, is because the estimated values for the two serpentine samples are three and four times as high as the measured values, which increases the average estimation error. Several authors observed that the tensile strength was an important parameter when considering asperity failure (Grasselli, 2001, Xia et al., 2014, Zhang et al., 2016). The shear strength criterion presented by Johansson and Stille (2014) considers the compressive strength of rock instead of the tensile strength. So, another reason for the large estimation errors in Johansson's criteria may be that the tensile strength is not considered in his criterion.

6 Case study: Sliding stability analysis of Kalhovd dam

6.1 Introduction

Kalhovd dam is a part of the reservoir Kalhovdfjorden, which is one of five reservoirs for Mår hydro power plant. The dam was completed in 1948 and is 386 meters long, of which 140 meters of them are free spillway, and 15 meters high at the most.

Figure 29: Dam Kalhovd (Photo: Gabriel Sas, LTU/NORUT)

Kalhovd dam does not fulfill the requirements for safety factor against sliding given by the Norwegian guidelines, and Statkraft are facing costly rehabilitations to get the dam "stable". The original stability calculations are based on information from site visits and the Norwegian guideline for concrete dams, where maximum allowed values for friction angles are given. In this case study, stability calculations will be performed based on the information from the shear tests on core samples from Kalhovd dam and a finite element analysis of a buttress, in addition to the method required by NVE.

6.2 General geometry of the dam

The dam consists of 65 buttresses with a distance from center to center (c/c) of 5.0 *m*. The flat slab has an inclination of 1:0.8. The thickness of the flat slab is 0.3 *m* at top, with an increasing thickness of 0.03 meter per vertical meter. The air side of the buttresses has an inclination of 1:0.33, and the thickness of the buttress is 0.3 *m* at top, increasing by 0.022 *m* per vertical meter. The dam has a vertical isolation wall, which is 0.15 *m* thick. Each buttress has an opening, which makes it possible to walk inside the dam. There is a pathway across the dam, with a width

of 1.0 *m*. There is a free spillway over 28 sections of 5.0 *m*, which gives a total length of 140 *m*. The height from the spillway up to the pathway is 1.12 *m*. Downstream the spillway, the water is dropped into the old river lane and then into the operation road to Strengen dam. The abutment on each side of the dam consist of concrete gravity dams with a length of approximately 20.0 *m* and maximum heights of 4.0 *m*.

6.3 Selection of buttress to use in stability analysis

To use the results from the shear tests in the stability analysis, the chosen buttress should have the same surface roughness as the samples that were used for shear tests. Sample 1 to 4 were extracted from buttress number 23, 7, 4 and 6, respectively. See Appendix G. Thus, the chosen buttress should preferably be from this area of the dam. In addition, the buttress must be exposed to the same normal stress as used in the shear tests. The applied normal stress was 0.5 *MPa*. The effect on shear capacity from topography and 1st order asperities is still not properly understood. Therefore, to avoid uncertainties regarding the effect from topography, a buttress with a flat foundation is preferable. Based on these preferences, buttress number 8 is chosen. Based on the construction drawings in Appendix G, the height of the buttress is estimated to be 6.5 *m*. This buttress is from the section of the dam without a spillway.

Figure 30: A photo from buttress number 8, taken inside dam Kalhovd. Photo: Dipen Bista, NTNU/NORUT

Figure 30 shows a photo of the buttress used for the case study. The photo is taken inside the dam. As seen on the photo, the interface between rock and concrete is not completely horizontal, as there is some formation in the topography. However, in this case study the foundation is assumed horizontal to avoid the uncertainties regarding the effect from asperities. The shear strength might be underestimated when the topography is disregarded.

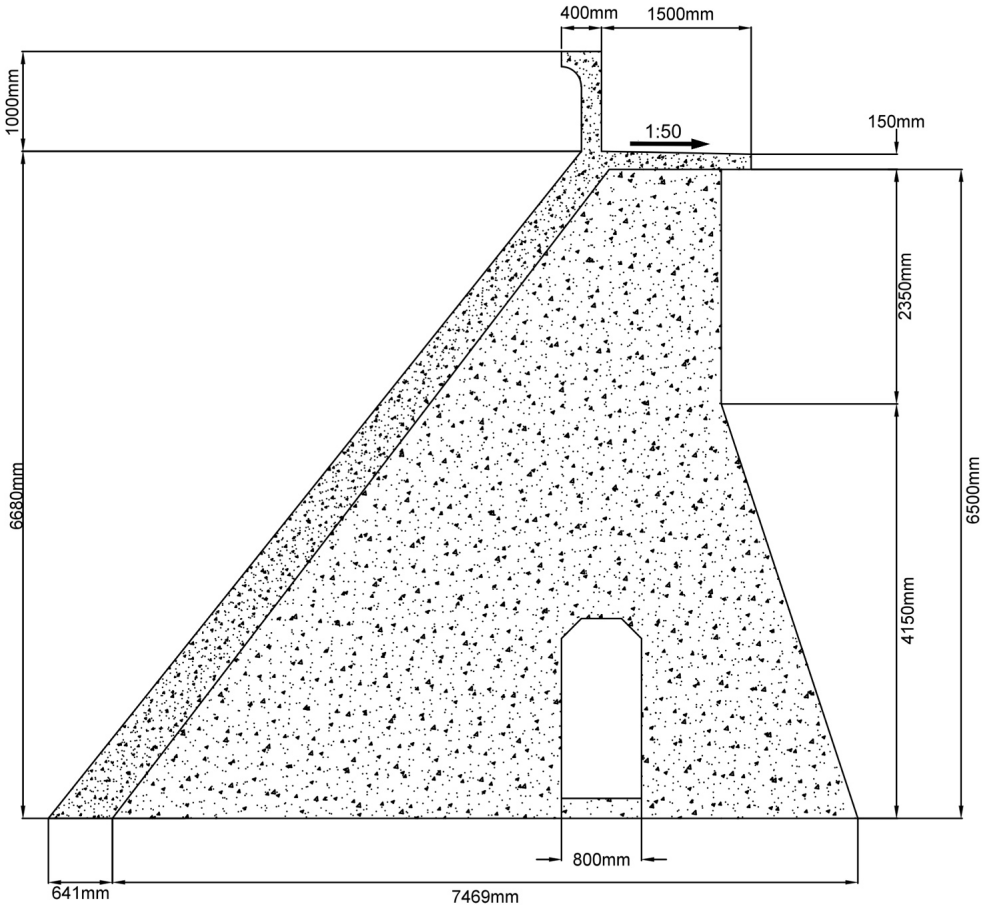

Figure 31: Approximately geometry of buttress number 8 at dam Kalhovd

Figure 31 shows the approximately geometry of buttress number 8 at Kalhovd dam. The highest regulated water level (HRWL) lays 0.29 *m* under the top of the walkway, which gives a maximum water depth of 6.39 *m*. The geometry of the buttress is based on the construction drawings found in Appendix G.

6.4 Finite element analysis

In order to find the normal stresses acting on the interface of the dam, a 2D finite element analysis was performed on the selected buttress. The finite element analysis was conducted with the software ATENA by Gabriel Sas at NORUT/LTU.

A model with simplified geometry was used in the analysis. In addition, the door opening in the buttress was disregarded. The reason for this is that this will ease up the meshing and analysis, but will not affect the result significantly. The thickness of the buttress varies with depth, from 0.3 *m* at top to 0. 44 *m* at bottom. In the model, the real thickness at the base, 0.44 *m*, is used over a height of approximately 1.0 *m* from the bottom, while the rest of the buttress has a thickness of 0.3 *m*. The reason for this is to get the real thickness of the buttress in the interface where sliding is assumed to occur.

The density of the unreinforced concrete from Kalhovd dam corresponds to 23.5 kN/m^3 (see Table 8). However, the density was measured on dry samples in the lab. Concrete at the dam site will be moist and have higher density, usually about 24.0 kN/m^3. The density of reinforced concrete was used in the analysis, and this is assumed to be 24.5 kN/m^3, since the dam is not heavily reinforced. The distance between the buttresses is 5.0 *m* from center to center, so loads from 5.0 *m* of flat slab, ice, water, uplift forces and pathway will act on the buttress. There is a concrete wall on top of the pathway that serves as a protection against waves, and this is not included in the model. As a result, the dead load from the wave protection is not included in the analysis. 5.0 *m* of wave protection corresponds to a gravitational force of approximately 29.0 *kN,* but this is negligible in relation to the other forces acting on the dam.

The material parameters from the rock and concrete extracted from Kalhovd dam were used as input parameters in the model. Since there was no bonding between the interfaces of the samples used for shear tests, and bonding is not documented at Kalhovd, the cohesive forces were assumed to be zero. The highest regulated water level (HRWL) gives a maximum water depth of 6.4 *m* in the model, which is 1.0 *cm* more than the maximum depth found from the construction drawings. This is due to simplification of the model, but 1.0 *cm* of extra depth will not affect the result. Uplift with maximum hydrostatic water pressure under the whole flat slab is assumed. Ice load of 100 *kN/m* is assumed, and the load is applied as a point load 0.25 *m* under HRWL.

The load case for the model was HRWL + ice load, including uplift under the flat slab. When running the model, the loads were applied in four steps; dead load, hydrostatic pressure, uplift and ice load, respectively.

Table 21: A summary of some of the input parameters in ATENA

Input parameter	Value
Water depth (*m*)	6.4
Ice load (*kN/m*)	100
Density reinforced concrete (kg/m^3)	2450
Density water (kg/m^3)	1000
Coefficient of friction (-) (for $\sigma_n=0$)	2.83
Rock bolts (*MPa*)	0
Cohesion (*MPa*)	0
Surface inclination (°)	0

Table 21 shows the input parameters used when modelling the normal stresses in ATENA.

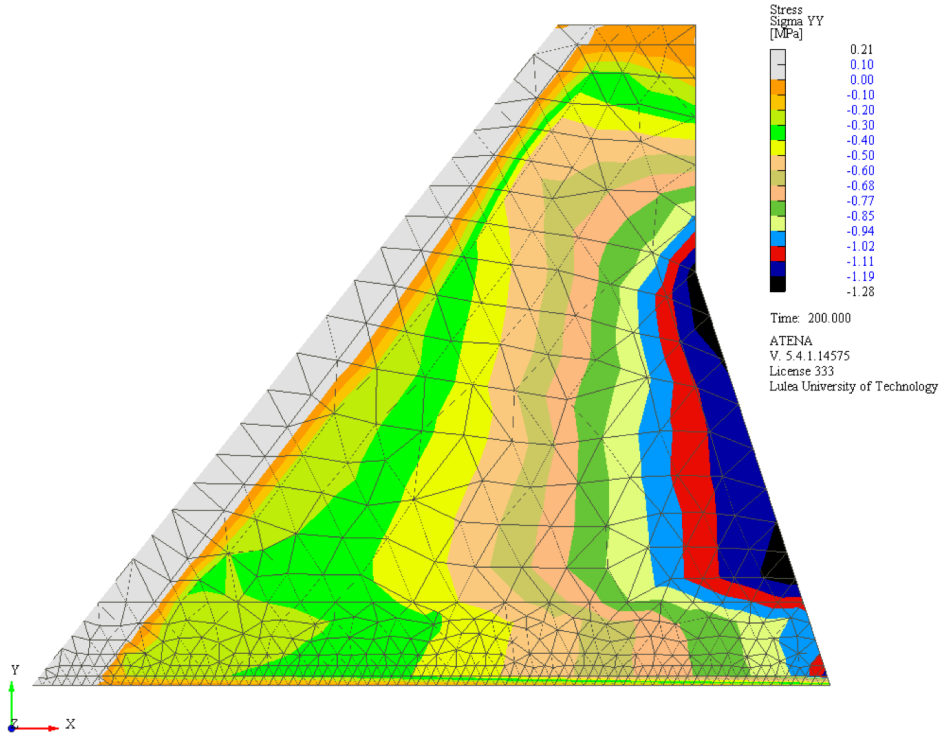

Figure 32: The result from the modelling of normal stresses in the interface conducted in the software ATENA

Figure 32 shows the result from the simulation of normal stresses in the buttress when all loads were applied. The rock-concrete interface lays above the first layer of triangles at the bottom of the model. The different colors represent different ranges of normal stress. The color bar to the right of the model shows the colors with corresponding values of normal stresses. The normal stress is assumed to increase linearly within each color section. Positive values of normal stresses correspond to tensile stress, while negative values correspond to compressive stress.

6.5 Stability analysis

Three stability analysis were performed. One analysis was based on the results obtained from the shear tests and the finite element analysis, while the other analysis were performed in accordance with the guidelines from NVE (NVE, 2005). Possible loads from earthquake, sediments and downstream water level were disregarded in all analysis. Since bonding in the interface and rock bolts are not documented, the value of cohesion and the strength from rock bolts will be set to zero.

6.5.1 Stability analysis based on results from shear tests and finite element analysis

The coefficient of friction, $tan\phi$, is dependent on the normal stress. Generally, the coefficient of friction will decrease with increasing normal stress, since the surface roughness will be smoothed out due to asperity degradation when the normal stress is increasing. To find a connection between the coefficient of friction and the normal stress, shear tests conducted with different normal stresses must be studied. Since the Kalhovd shear tests were only conducted with one normal stress, previous conducted shear tests were used to find the connection. In this thesis, the shear tests conducted by Grasselli (2001) were used for this purpose. The coefficient of friction was calculated by using Mohr-Coulomb and dividing the peak shear strength, τ_p, with the applied normal stress, σ_n, as seen in Equation 63.

$$tan\phi = \frac{\tau_p}{\sigma_n} \tag{63}$$

Grasselli (2001) conducted 37 direct shear tests on rock joints with natural surface roughness and a size of 140 mm by 140 mm. Seven different rock types were used, among them both soft and hard rock types. By using test results from different types of rock, the average decrease in the coefficient of friction with normal stress can be determined by fitting a linear trend line to the data. The rock at Kalhovd dam looks like gneiss, and in addition, the rock has similar material properties as the gneiss samples used by Grasselli in his tests. When plotting the coefficient of friction against normal stress for the shear tests conducted by Grasselli, the trend line for all the samples have approximately the same slope as the trend line for gneiss only.

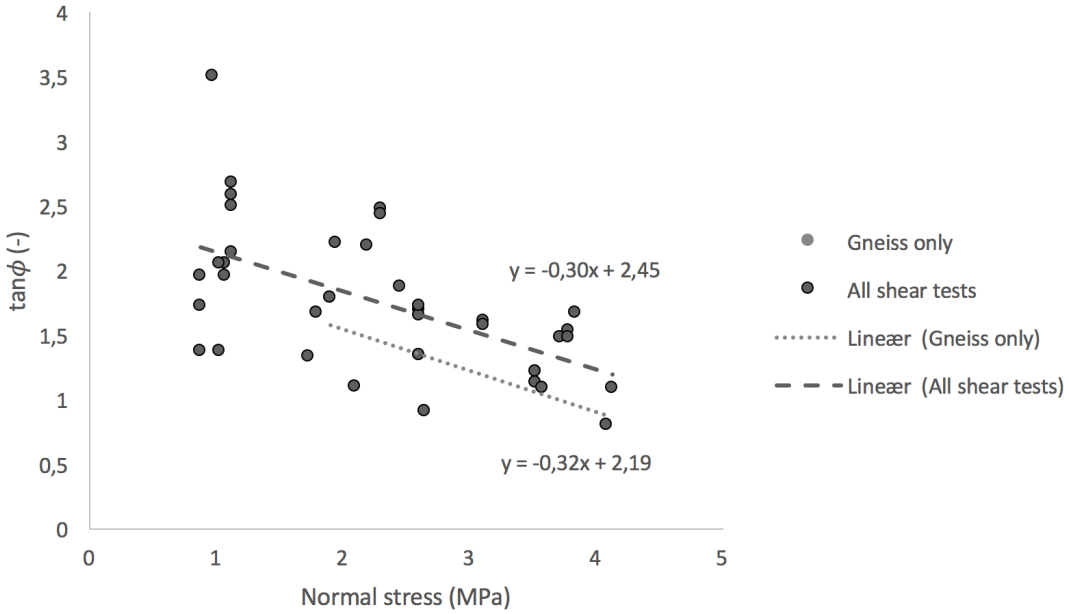

Figure 33: Coefficient of friction vs normal stress for shear tests conducted by Grasselli and linear trend lines

As seen in the linear trend lines in Figure 33, the coefficient of frictions decreases with 0.3 when the normal stress increases with 1.0 *MPa* for both lines. Therefore, it is reasonable to assume the same decrease in coefficient of friction for the foundation at dam Kalhovd.

This trend line must then be adjusted to fit the results from the Kalhovd shear tests. The coefficient of friction obtained from the shear tests at Kalhovd was found to be 2.68 for a normal stress of 0.5 *MPa*, as seen in Table 22.

Table 22: Average value of peak shear strength and corresponding coefficient of friction

Sample	σ_n (MPa)	τ_{peak} (MPa)	tanϕ (-)
Average of 1-3	0.5	1.34	2.68

The coefficient of friction for Kalhovd was calculated with Equation 63 by using the average peak shear strength of Sample 1 to 3. Sample 4 is not included, as this shear test did not give reliable results since the surface was not in contact.

The trend line must then be adjusted to fit the coefficient of friction obtained from the Kalhovd shear tests. As seen in Figure 33, the trend line for all the shear tests lay closest to the point where the coefficient of friction equals 2.68 for a normal stress of 0.5 MPa. Therefore, the trend line for all the shear tests will be used further in this thesis. The function of the trend line has the form of a straight line $y = ax + b$, where *a* is the slope, *b* is where the line intercepts the y-axis and *x* is the independent variable, which in this case is the normal stress. To fit the linear trend line to the point obtained from the Kalhovd shear tests without changing the slope, the value of *b* must be adjusted. The readjusted function can be seen in Equation 64.

$$y = -0.30x + 2.83 \tag{64}$$

By substituting *y* with the coefficient of friction, $tan\phi$, and *x* with the normal stress, σ_n, the relationship between normal stress and coefficient of friction can be expressed as shown in Equation 65.

$$tan\phi = -0.30 \cdot \sigma_n + 2.83 \tag{65}$$

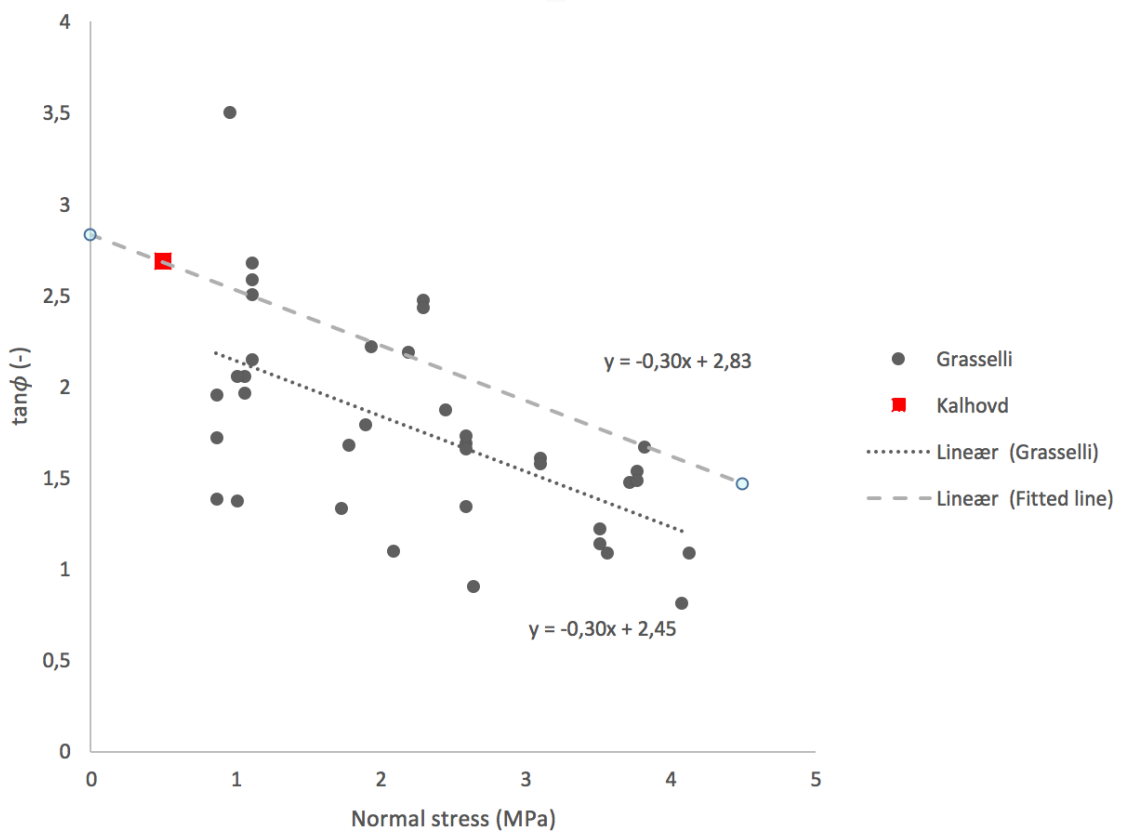

Figure 34: The trend line was adjusted to fit the point obtained from the Kalhovd shear tests

Figure 34 shows how the trend line was adjusted to fit the coefficient of friction obtained from the shear tests conducted on samples from Kalhovd. The adjusted trend line is further up than the trend line obtained from the shear test conducted by Grasselli. This may indicate that the surface roughness at Kalhovd is rougher than the surfaces on the samples used by Grasselli. Another reason could be that scale effects increased the shear strength of the Kalhovd samples, thus, increased the coefficient of friction. The samples tested by Grasselli measured 140 *mm* by 140 *mm*, while the core samples from Kalhovd had a diameter of 94 *mm.* A scale effect could therefore be the reason that the coefficient of friction is higher for the Kalhovd samples.

By combining the normal stress distribution in the interface obtained from the finite element analysis and the relationship between normal stress and coefficient of friction, a stability analysis of the buttress can be conducted. This was done by calculating a factor of safety. Based on the finite element analysis, the distribution of the normal stresses acting on the interface was found by studying Figure 32. The normal stress was found for every 10 *cm* in the interface and plotted against the length of the buttress, as shown in Figure 35.

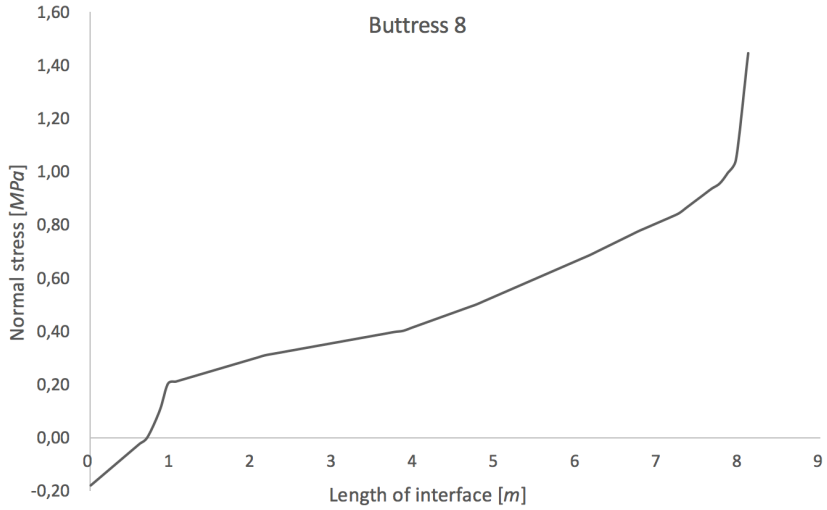

Figure 35: Normal stress in the interface plotted against the length of the interface. Negative values indicate tensile stress, positive values indicate compressive stress.

The interface includes the interfaces from both the flat slab and the buttress. Tensile stresses are mainly found in the flat slab, while the compressive stresses occur in the buttress. Only the interface that is exposed to compressive stress was considered in the sliding stability analysis, since the interface which is exposed to tensile stress will not contribute to shear resistance.

Next, the interface of the buttress with compressive stresses was divided into 15 sections of 0.5 *m*, except the first and last section which has a length of 0.55 *m* and 0.35 *m*, respectively. Since the normal stress can change within the sections, the average normal stress, $\sigma_{n,\,average}$, is used to find the corresponding normal force acting on the interface, as shown in Equation 66.

$$V'_{section} = \frac{\sigma_{n,average}}{A_{section}} \tag{66}$$

Where $V'_{section}$ is the effective vertical forces acting on the interface in the considered section and $A_{section}$ is the area of the interface in the considered section.

The average normal stress within the section can be expressed as shown in Equation 67.

$$\sigma_{n,average} = \frac{\sigma_{n1} + \sigma_{n2}}{2} \tag{67}$$

Where σ_{n1} and σ_{n2} are the normal stresses in the start and end of the considered section, respectively.

The coefficient of friction varies with normal stress, so the coefficient of friction was calculated for every section by inserting the average normal stress for the considered section in Equation 65. The stabilizing frictional forces acting on the interface can then be calculated by multiplying the effective vertical force with the corresponding coefficient of friction.

The sum of horizontal forces acting on the dam, ΣH, were found by adding up the load from horizontal water pressure and the ice load.

The factor of safety for the considered buttress was calculated by dividing the stabilizing forces over the driving forces, as seen in Equation 68.

$$FS = \frac{\sum V'_{section} \cdot \tan \phi_{,section}}{\sum H} \tag{68}$$

Where FS is the factor of safety, $tan\phi_{,section}$ is the coefficient of friction for the considered section and ΣH is the sum of horizontal forces acting on the buttress.

By using Equation 68, the factor of safety for buttress number 8 was calculated to be 2.96, see Appendix H for calculations. According to NVE, the factor of safety must be equal or greater than 1.4 to fulfill the requirements for sliding stability (see subsection 2.2.1). Hence, the buttress is stable according the requirements for sliding stability given by NVE.

6.5.2 Stability analysis based on NVE's guideline

Based on the geometry of buttress number 8, showed in Figure 31, and NVE's guidelines for concrete dams (NVE, 2005), two stability analysis of the buttress were performed. The load case was HRWL + ice load, including full uplift under the flat slab. Both the maximum allowed friction angle according to NVE's guidelines and the friction angle obtained from shear tests were used.

Loads corresponding to 5.0 *m* of flat slab, pathway, ice load, hydrostatic pressure and uplift were assumed to act on the dam. Table 23 shows the input parameters used in the analysis.

Table 23: Parameters used as input parameters in the stability analysis based on NVE

Input parameter	Value
Water depth (*m*)	6.39
Ice load (*kN/m*)	100
Density reinforced concrete (kg/m^3)	2450
Density water (kg/m^3)	1000
Peak friction angle (°)	50 and 69
Rock bolts (*MPa*)	0
Cohesion (*MPa*)	0
Surface inclination (°)	0

The factor of safety should according to the guidelines be calculated by using the shear friction method, as shown in Equation 5. The horizontal forces acting on the dam are calculated by summing up the forces from horizontal hydrostatic water pressure and ice load acting on the dam. The effective vertical force was calculated by summing up the self-load from the dam and the vertical hydrostatic pressure and subtracting the uplift force. The factor of safety was found to be 1.18 by using NVE´s maximum allowable friction angle and 2.57 when using the friction angle obtained from shear tests. See Appendix H for calculations.

6.6 Discussion about the results

When using the maximum allowable friction angle according to NVE (Method 2), the factor of safety is underestimated compared to the method were the sliding stability were analyzed by using a combination of finite element analysis and shear test results (Method 1), or if using the friction angle obtained from shear tests in the shear friction method (Method 3). The requirement for safety factor, $FS \geq 1.4$, is fulfilled with good margin if using Method 1 or 3. However, if using Method 2, the calculated factor of safety is smaller than the required one, and the buttress is not stable according to the requirements. Table 24 shows a summary of the calculated factors of safety.

Table 24: Results from sliding stability analysis

Method	Factor of safety	Requirement
1: FE-analysis + shear tests	2.96	1.4
2: NVE: ϕ_p maximum allowable	1.18	1.4
3: NVE: ϕ_p obtained from tests	2.57	1.4

The factor of safety calculated by Method 1 is 2.5 times higher than the factor of safety calculated based on NVE's guidelines and a friction angle of 50 °. The main reason for this is the different peak friction angles used in the calculations. Method 2 uses a constant peak friction angle of 50 °. In the calculations from Method 1, the coefficient of friction ranged from 2.8 to 2.47, depending on the normal stress, which corresponds to peak friction angles from 68.0 ° to 70.3 °. These values were based on the coefficient of friction obtained from the shear tests and the relationship between normal stress and coefficient of friction. These high values of coefficients of friction, indicates that the interface at Kalhovd is rougher than what can be assume in the calculations based on NVE´s guidelines. Method 2 and 3 are both based on the shear friction method, the only difference is the value of peak friction angle. If using the peak friction angle obtained from the shear tests, the factor of safety doubles compared to the safety of factor calculated with the maximum allowable friction angle. This indicates that the maximum allowable friction angle is too low to represent the roughness in rock-concrete interfaces found at dam Kalhovd. It is unclear what is the basis for the decision of maximum allowable friction angle. It may seem like NVE has added an additionally safety by choosing a maximum allowable friction angle that is conservative. Typical friction angle values for rock types like gneiss, granite and sandstone varies from 59 to 62 degrees for sound conditions (Novák, 2007), which is significantly higher than maximum allowable friction angle of 50 °. It is therefore reason to believe that the maximum allowable friction angle should be increased, at least if the friction angle can be documented with shear tests.

If either Method 1 or Method 3 could be approved by NVE, buttress number 8 can be considered stable according to the required safety factor. The original calculations were calculated with the shear friction method, and the maximum allowable friction angle of 50 ° was used (Method 2). The factor of safety is significantly larger for Method 1 and 3, compared to the factor of safety

for Method 2. It is therefore reasonable to assume that many of the other buttresses that were considered unstable could be considered stable if Method 1 or 3 can be used to assess the sliding stability.

The shear friction method is based on the average normal stress acting on the dam foundation and will therefore not consider the fact that the rock-concrete interface will have different coefficient of frictions due to non-uniform normal stresses. A finite element analysis is therefore preferred, as the changes in shear strength through the interface can be included in the stability analysis. None of the existing shear strength criteria are developed to consider the non-uniform normal stress and will therefore not be able to describe the varying shear capacity in the rock-concrete interface. As a result, the calculated factor of safety could be either overestimated or underestimated when using an average normal stress.

There was no bonding between the rock-concrete interface of the samples when conducting the shear test. Any potential contribution on shear strength from the bonding was therefore not considered in this stability analysis. When extracting the core samples, it could be seen that the interface had been “glued” together and bonding was present. However, it is hard to keep the bonding intact when extracting samples, and the bond in the interface will often break. Most likely, there will be bonding between the rock-concrete interface of the dam which will increase the shear capacity. The degree of bonding in the interface and the strength of the bond should be investigated if included in the stability analysis, but there are currently no non-destructive methods developed to do this.

The effect on shear strength from interlocking of the flat slab was not included in the case study. As a result, the shear capacity of the dam will be underestimated. If rock bolts and cohesive forces could be documented and included in the stability analysis, the factor of safety would be even higher. However, the scale effects could have resulted in a too high friction angle which can overestimate the factor of safety. The potential scale effects might in this case be compensated for by any extra strength from rock bolts and cohesion.

7 Summary and discussion

Grasselli's model turned out to be the most suitable model to estimate the peak shear strength of the samples, while Mohr-Coulomb was the least suitable method due to the largest estimation errors. If using the maximum allowed peak friction angle according to NVE's guidelines, Mohr-Coulomb underestimates the peak shear strength and the estimated values were only half of the measured peak shear strength obtained from shear tests. Since the estimated values were 50 % less than the measured peak shear strengths, it is reasonable to assume that the factor of safety calculated by using the shear friction method, which are based on Mohr-Coulomb, will underestimate the factor of safety. When the sliding stability of the considered buttress were assessed by using Mohr-Coulomb and the maximum allowed friction angle of 50 °, the obtained safety factor was more than 50 % less than the safety factors obtained when using the results from the shear tests. This verifies the assumption that Mohr-Coulomb underestimates the safety factor when the sliding stability is assessed according to NVE's guideline. The considered buttress will therefore have higher safety factor than what is calculated when using this method.

There are great advantages of using finite element modelling when assessing the sliding stability of concrete dams, as it makes it possible to consider the effect from a non-uniform normal stress distribution on the shear capacity. In addition, the obtained distribution of normal stresses can be used to determine the compressive zone of the interface, which is important if cohesion is present. Preferable, the finite element analysis should be combined with shear tests on drilled cores from the dam site to calculate the shear capacity. This will give the more realistic values of the shear capacity than if the shear capacity is calculated with a shear strength criteria developed for uniform normal stresses. Todays practice for direct shear tests are often considered to be unreliable, as there are no standard tests procedure. There is therefore a need for a standard test method that can be used to obtain reliable shear strength and friction angle values based on shear tests, that can be used along with finite element analysis to estimate the shear capacity of dams.

However, finite element analysis is time consuming, especially when it comes to including the topography of the foundation. Many concrete dams are located without road access, and extracting drilled cores from the dam site can therefore be expensive and time consuming as well. The shear strength models will then be a cheaper option to determine the shear capacity of the dam, but at the cost at simplifications. The non-uniform stress distribution can be

incorporated when estimating the shear strength with existing shear strength criteria by dividing the buttress into sections with different average normal stresses. The models can then be applied on each section, which will have different normal stresses. Grasselli's model has proved to be able to estimate the shear capacity of shear tests with good accuracy. The model considers important aspects like the surface roughness and shear direction. If the accuracy of the model could be verified with a full-scale test, the model could be applied on Ambursen dams, where the surface is available for scanning. The surface can then be scanned along both sides of the buttress, and the average 3D roughness parameters may be assumed to represent the surface roughness under the buttress. However, the interface in gravity dams are not available for scanning, so models which are based on surface scanning's will not be applicable on gravity dams.

8 Conclusion

8.1 Results

The results from the shear tests on core samples from Kalhovd dam gave an average peak shear strength of 1.34 *MPa,* which corresponds to a peak friction angle of 69.5 °. The difference between the lowest and highest measured peak shear strength was 0.5 *MPa*, which can be related to the difference in surface roughness between the samples. Grasselli's shear strength criterion was best suited to estimate the peak shear strength of the conducted shear tests. Mohr-Coulomb's shear strength criterion underestimated the peak shear strength from the shear tests more than 50 %, and was the least suitable model due to high estimation errors.

A case study was performed on a 6.5 *m* high buttress from Kalhovd dam. By using a combination of finite element analysis and the result from shear tests, the factor of safety was found to be 2.96, which makes the dam "stable". When using the shear friction method along with the peak friction angle obtained from shear tests, the factor of safety was found to be 2.57, and the buttress is considered stable. However, when using the maximum allowable peak friction angle according to NVE's guidelines, the factor of safety was calculated to be 1.18, and the buttress is not considered stable. Both methods that are based on the results from the shear tests gives a factor of safety which are significantly higher than the factor of safety calculated based on NVE's guidelines where the peak friction angle will have to be assumed. If the peak friction angle obtained from the shear tests can be approved as documentation of the friction angle, the considered buttress will be stable according to the Norwegian requirements for factor of safety against sliding.

Today's challenge is to find cost-efficiency methods that can be used to estimate the shear capacity of the rock-concrete interface of dams more accurate than the Mohr-Coulomb's criterion. A combination of finite element modelling and shear tests on drilled cores from the dam site would be preferable, but this is costly and shear tests are often considered as unreliable. It is important to know if the dam interface is bonded or not, since a bonded interface will increase the shear capacity of the dam significantly. However, it is hard to determine how much of the interface that is bonded, as the interface is not visible to inspect. Non-destructive mapping of the bonding is preferable, but no universal method to do this is developed yet.

8.2 Further work

For further work, the author recommends making a guideline for how to determine the input parameters in the considered shear strength models when applying the models on rock-concrete interfaces. The guideline should include how to determine the basic friction angle and material properties like tensile strength and compressive strength when the interface consists of two different materials.

It is also recommended to preform full-scale tests to verify if the combination of finite element analysis and shear tests results from the rock-concrete interface can be used to determine the shear capacity of a buttress. The full-scale tests should also be used to study the accuracy of newly developed methods like Grasselli's shear strength criterion and investigate possible scale effects for the shear strength models and shear tests conducted at small samples.

A standard method for conducting shear tests that can be considered good enough to be used in sliding stability analysis should be developed. The test method should include requirements for sample size for both drilled cores and bigger samples, and a test procedure.

9 References

ALEJANO, L. R., GONZÁLEZ, J. & MURALHA, J. 2012. Comparison of different techniques of tilt testing and basic friction angle variability assessment. *Rock mechanics and rock engineering,* 45**,** 1023-1035.

ASTM, S. 2002. Standard Test Method for Elastic Moduli of Intact Rock Core Specimens in Uniaxial Compression. *D3148-02.*

ASTM, S. 2003. Standard test method for compressive strength of cylindrical concrete specimens. *C39/C39M - 03.*

ASTM, S. 2016. Standard Test Method for Splitting Tensile Strength of Intact Rock Core Specimens. *D3967-16.*

BALLIVY, G., GRAVEL, C. & EL MALKI, T. 2006. Development of a new experimental protocol to estimate the shear strength of concrete-rock joints. *Proceedings of EUROCK´06.* Belgium.

BARTON, N. & BANDIS, S. Effects of block size on the shear behavior of jointed rock. The 23rd US Symposium on Rock Mechanics (USRMS), 1982. American Rock Mechanics Association, 739-760.

BARTON, N. & CHOUBEY, V. 1977. The shear strength of rock joints in theory and practice. *Rock mechanics,* 10**,** 1-54.

CDA 2013. Dam safety guidelines 2007 (2013 edition).

COLIO GUTIÉRREZ, M. 2013. *Shear resistance for concrete dams: Laboratory tests.* Master thesis, NTNU.

DAWSON, R. V., CURTIS, D. D. & DONNELLY, C. R. 1998. Sliding resistance of concrete gravity dams. *CEA No. 9331 G 2002.* Montreal: CEATI (Canadian Electricity Assosoation Technologies Inc).

DONNELLY, C. R. & RIGBEY, S. J. 2003. The Assessment of Sliding Resistance Beneath Concrete Structures. *WaterPower XIII, July*.

FERC 2016. Engineering Guidelines for Evaluation of Hydropower Projects, Chapter III, Gravity dams. .

FISHMAN, Y. A. 2009. Stability of concrete retaining structures and their interface with rock foundations. *International Journal of Rock Mechanics and Mining Sciences,* 46**,** 957-966.

GRASSELLI, G. 2001. Shear strength of rock joints based on quantified surface description. EPFL (Lausanne).

GRASSELLI, G. 2006. Manuel Rocha Medal Recipient Shear Strength of Rock Joints Based on Quantified Surface Description. *Rock Mechanics and Rock Engineering,* 39**,** 295-314.

GRASSELLI, G. & EGGER, P. 2003. Constitutive law for the shear strength of rock joints based on three-dimensional surface parameters. *International Journal of Rock Mechanics and Mining Sciences,* 40**,** 25-40.

GRASSELLI, G., WIRTH, J. & EGGER, P. 2002a. Quantitative three-dimensional description of a rough surface and parameter evolution with shearing. *International Journal of Rock Mechanics and Mining Sciences,* 39**,** 789-800.

GRASSELLI, G., WIRTH, J. & ZIMMERMAN, R. W. Functional parameters for quantifying the surface anisotropy of rock discontinuities. ISRM International Symposium-EUROCK 2002, 2002b. International Society for Rock Mechanics.

GRØNENG, G. & NILSEN, B. 2009. Procedurec for determining input parameters for Barton-Bandis joint shear strength formulation. Trondheim.

HONG, E. S., LEE, J. S. & LEE, I. M. 2008. Underestimation of roughness in rough rock joints. *International Journal for Numerical and Analytical Methods in Geomechanics,* 32**,** 1385-1403.

HOU, D., RONG, G., YANG, J., ZHOU, C., PENG, J. & WANG, X. 2015. A new shear strength criterion of rock joints based on cyclic shear experiment. *European Journal of Environmental and Civil Engineering*, 1-19.

JOHANSSON, F. 2009. *Shear Strength of Unfilled and Rough Rock Joints in Sliding Stability Analyses of Concrete Dams*.

JOHANSSON, F. 2016. Influence of scale and matedness on the peak shear strength of fresh, unweathered rock joints. *International Journal of Rock Mechanics and Mining Sciences,* 82, 36-47.

JOHANSSON, F. & STILLE, H. 2014. A conceptual model for the peak shear strength of fresh and unweathered rock joints. *International Journal of Rock Mechanics and Mining Sciences,* 69, 31-38.

KROUNIS, A., JOHANSSON, F. & LARSSON, S. 2016. Shear Strength of Partially Bonded Concrete–Rock Interfaces for Application in Dam Stability Analyses. *Rock Mechanics and Rock Engineering,* 49, 2711-2722.

LADANYI, B. & ARCHAMBAULY, G. 1970. Simulation of the shear behaviour of a jointed rock mass. *The 11th U.S Symposium on Rock Mechanics* 7, 105-125.

LIAHAGEN, S. A. 2012. *Stabilitet av betongdammer-Ruhetens påvirkning på skjærkapasiteten mellom betong og berg*.

LO, K., OGAWA, T., LUKAJIC, B., TSUI, K. & WANG, S. 1990. Evaluation of strength parameters of concrete-rock interface for dam safety assessment.

MAKSIMOVIĆ, M. 1992. New description of the shear strength for rock joints. *Rock mechanics and rock engineering,* 25, 275-284.

MAKSIMOVIĆ, M. 1996. The shear strength components of a rough rock joint. *International Journal of Rock Mechanics and Mining Sciences and Geomechanics Abstracts,* 33, 769-783.

MORADIAN, Z. A., BALLIVY, G. & RIVARD, P. 2012. Application of acoustic emission for monitoring shear behavior of bonded concrete–rock joints under direct shear test. *Canadian Journal of Civil Engineering,* 39, 887-896.

MOUZANNAR, H. 2016. *Characterization of shear strength and behavior of interfaces between concrete and rock foundation of hydraulic structures.* . PhD, UNIVERSITÉ DE LYON.

NGU. 2017. *Bedrock data base* [Online]. NGU. Available: http://geo.ngu.no/kart/berggrunn_mobil/ [Accessed].

NICHOLSON, G. A. 1983. Design of gravity dams on rock fundations: Sliding stability assessment by limit equilibrium analysis and selection of shear strength parameters Geotechnical Laboratory, U.S Army Corps of Engineers, Waterways Experiment station.

NILSEN, B. 2016. *Ingeniørgeologi-berg, grunnkurskompendium,* Trondheim Institutt for geologi og bergteknikk.

NOVÁK, P. 2007. *Hydraulic structures,* London, Taylor & Francis.

NVE 2005. Retningslinjer for betongdammer til forskrift § 4.8 om sikkerhet og tilsyn med vassdragsanlegg.

PATTON, F. D. 1966. *Multiple modes of shear failure in rock and related materials.* University of Illinois.

SINTEF. Materialdata for naturstein. Typiske verdier. . Available: https://sintef.no/globalassets/upload/teknologi_og_samfunn/berg-og-geoteknikk/lister/typiske-materialdata-for-naturstein.pdf.

SWEDENERGY AB 2012. RIDAS 2012 - Kraftföretagens riktlinjer för dammsäkerhet.

TANG, Z. & WONG, L. 2015. New Criterion for Evaluating the Peak Shear Strength of Rock Joints Under Different Contact States. *Rock Mechanics and Rock Engineering,* 49, 1191-1199.

TATONE, B. S. A. & GRASSELLI, G. 2009. A method to evaluate the three-dimensional roughness of fracture surfaces in brittle geomaterials. *Review of Scientific Instruments,* 80.

THE MATHWORKS INC. 2016. MATLAB.

TIAN, H., CHEN, W., YANG, D. & YANG, J. 2015. Experimental and Numerical Analysis of the Shear Behaviour of Cemented Concrete–Rock Joints. *Rock Mechanics and Rock Engineering,* 48, 213-222.

WESTBERG, M. W. & JOHANSSON, F. 2016. Probalistic model code for concrete dams. Stockholm: Energiforsk.
XIA, C.-C., TANG, Z.-C., XIAO, W.-M. & SONG, Y.-L. 2014. New Peak Shear Strength Criterion of Rock Joints Based on Quantified Surface Description. *Rock Mechanics and Rock Engineering,* 47**,** 387-400.
ZHANG, X., JIANG, Q., CHEN, N., WEI, W. & FENG, X. 2016. Laboratory Investigation on Shear Behavior of Rock Joints and a New Peak Shear Strength Criterion. *Rock Mechanics and Rock Engineering,* 49**,** 3495-3512.

Appendix A - Material properties of Kalhovd samples

Splitting test:

Table 25: Results from splitting test in Narvik

S.N.	Sample		Diameter (mm)				Length			Rate of loading (Mpa/sec)	Max load (N)	Tensile strength (Mpa)	Notes
			Top	Middle	Bottom	Average	Axis 1	Axis 2	Average				
1	Kalhovd Concrete	SC-K-1				94,20			108		46250	2,89	High rate of application of load because the machine was not set before test.
2		SC-K-2	94,2	94,2	94,2	**94,20**	108,2	107,8	**108**	0,0167	64620	4,04	
3		SC-K-3	94,2	94,2	94,2	**94,20**	106	106,3	**106,15**	0,0233	45780	2,91	The wooden piece slipped so have to reload. Force reached before slipping 49.430 kN
4	Kalhovd Rock	SR-K-1	94,5	94,5	94,5	**94,50**	55,8	55,5	**55,65**	0,35	80230	9,71	
5		SR-K-2	94,1	94,1	94,1	**94,10**	53	53,4	**53,2**	0,35	120990	15,39	
6		SR-K-3	93,7	93,7	93,8	**93,73**	50,7	50,5	**50,6**	0,35	50670	6,80	donot look like tensile failure. Failure on one edge (see photos)
7		SR-K-4	93,7	93,7	93,6	**93,67**	52,7	52,8	**52,75**	0,35	44210	5,70	
8		SR-K-5	94,1	94,1	93,9	**94,03**	52,8	52,8	**52,8**	0,35	79450	10,19	
9		SR-K-6	93,7	93,6	93,6	**93,63**	50,2	50,6	**50,4**	0,35	94670	12,77	
10		SR-K-7	94,5	94,6	94,6	**94,57**	50,2	50,6	**50,4**	0,35	87890	11,74	
11		SR-K-8	94,1	94,1	94	**94,07**	50,7	51	**50,85**	0,35	73980	9,85	
12		SR-K-9	94,3	94,3	94,3	**94,30**	53,9	53,9	**53,9**	0,35	61240	7,67	

Figure 36: Test apparatus and set up for splitting tests

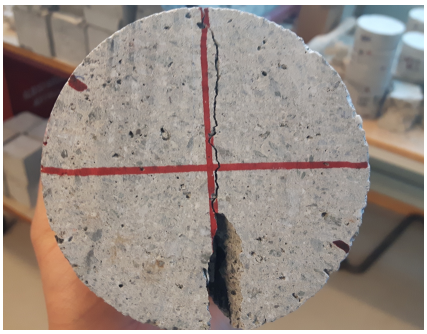

Figure 37: Sample SC-K-2

Figure 38: Sample SR-K-2

Figure 39: Sample SR-K-2

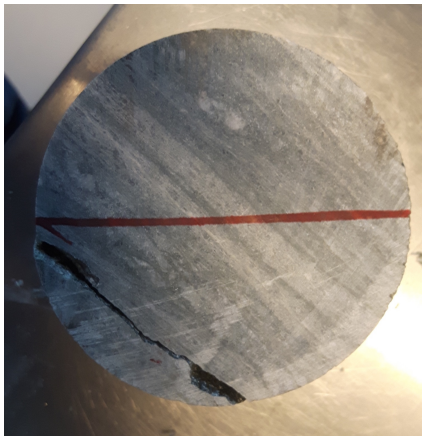

Figure 40: Sample SR-K-3

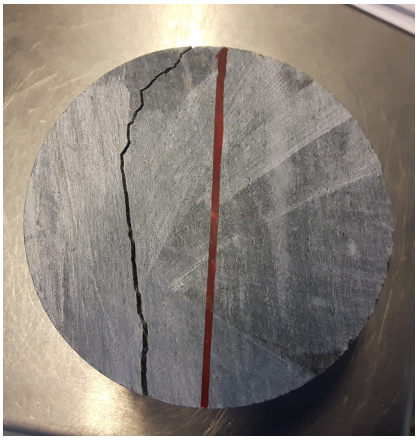

Figure 41: Sample SR-K-4

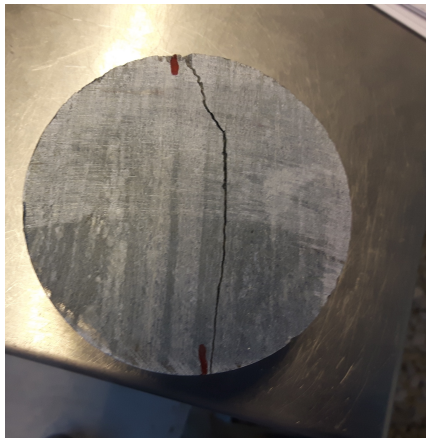

Figure 42: Sample SR-K-4

Figure 43: Sample SR-K-5

Figure 44: Sample SR-K-5

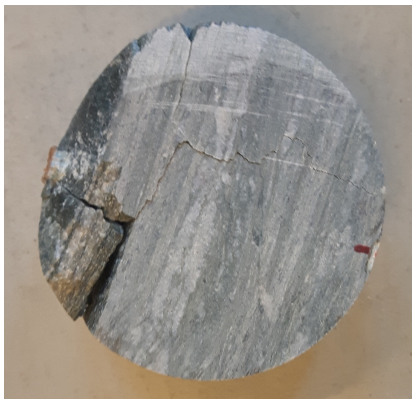

Figure 45: Sample SR-K-6

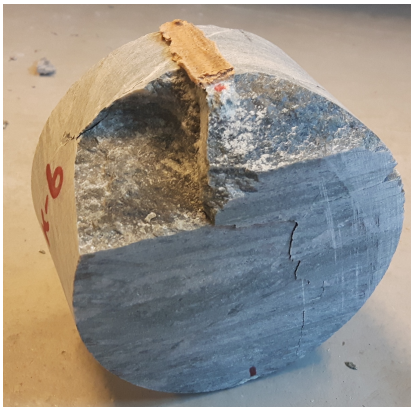

Figure 46: Sample SR-K-6

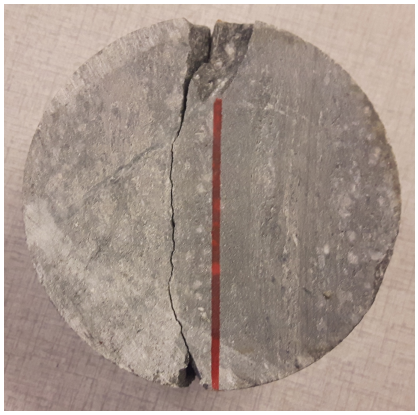

Figure 47: Sample SR-K-7

Figure 48: Sample SR-K-7

Figure 49: Sample SR-K-8

Figure 50: Sample SR-K-8

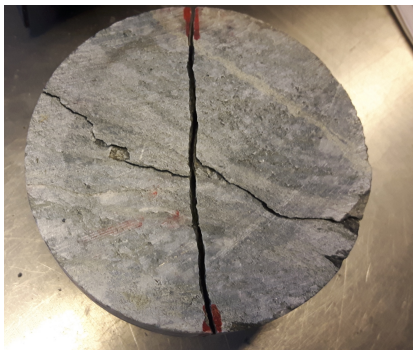

Figure 51: Sample SR-K-8

Figure 52: Sample SR-K-9

Figure 53: Sample SR-K-9

Uniaxial compressive test:

Table 26: Test results from uniaxial compressive tests

PROV	beteckn.	Betong	Betong	Betong	Berg	Berg	Berg
	nummer	5_1	5_2	8_1	4_2	6_2	7_2
Borrdjup	m						
Provningsdag	datum	170511	170511	170511	170511	170511	170511
Bergart	-						
Höjd *H*	mm	182,92	188,49	188,42	200,26	199,92	199,32
Diameter ϕ	mm	94,12	94,14	94,08	94,27	94,22	94,25
Vikt *m*	gram	3120,0	3006,5	3039,0	3730,0	3776,0	3764,0
Area *A*	mm²	6958	6960	6952	6980	6972	6977
Volym *V*	dm³	1272667	1311978	1309820	1397755	1393902	1390604
Densitet ρ	kg/m³	2451,54	2291,58	2320,17	2668,56	2708,94	2706,74
Brottlast F_{max}	kN	204,7	316,0	167,7	871,6	337,9	-
Tryckhållf. σ_c	MPa	**29,4**	**45,4**	**24,1**	**124,9**	**48,5**	**#VERDI!**
Belastn.hast	mm/s	0,002	0,002	0,002	0,002	0,002	0,050
Average density	kg/m³		2354,4		2694,7		
E modulus	GPa	26,42	29,99	18,41	59,52	33,55	-
Cube strength concrete	MPa	**36,8**	**56,7**	**30,2**			
Average cube strength	MPa		**41,2**		Average rock strength [MPa]		**86,7**

Sample 7_2 failed prematurely because it was loaded along the natural planes, and is therefore not relevant for compressive strength estimates. In addition, the loading rate was too high. The compressive strength is calculated with $\sigma_c = P/A$, where P is the maximum load and A is the area. The elastic modulus is found from stress-strain curves from the second loading cycle for concrete, and from the stress-strain curve from the whole test for rock. The elastic modulus, *E* are calculated with $E = \Delta\sigma/\Delta\varepsilon$.

Figure 54: Concrete 5_1

Figure 55: Concrete 5_2

Figure 56: Concrete 8_1

Figure 57: Rock 4_2

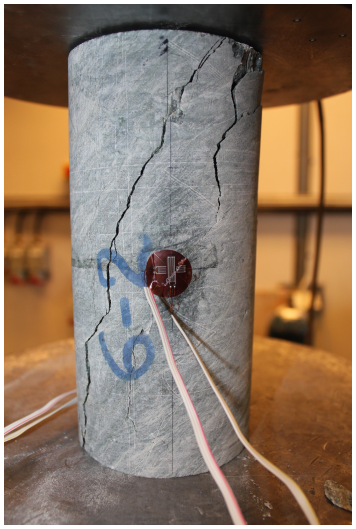

Figure 58: Rock 6_2

Figure 59: Rock 7_2

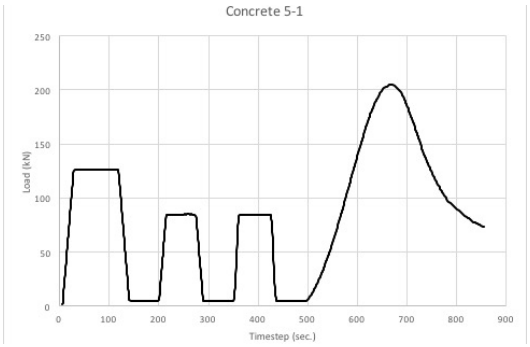

Figure 60: Load vs time diagram for compressive tests

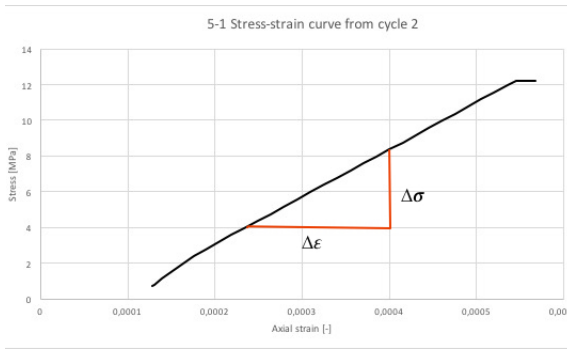

Figure 61: E modulus from stress-strain curve from cycle 2

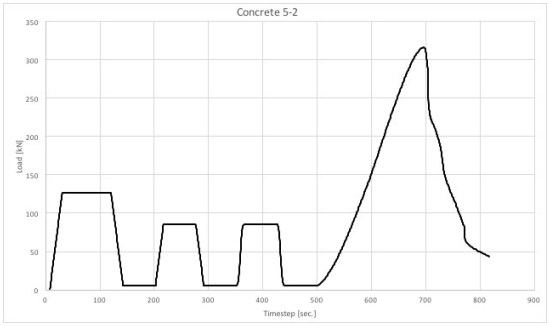

Figure 62: Load vs. time diagram for compressive test

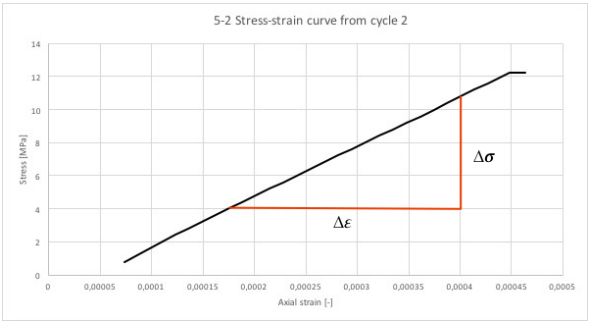

Figure 63: E modulus from stress-strain curve from cycle 2

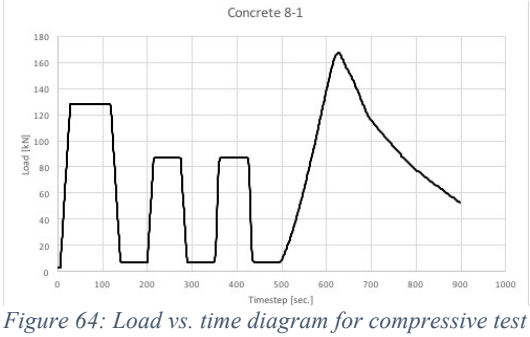

Figure 64: Load vs. time diagram for compressive test

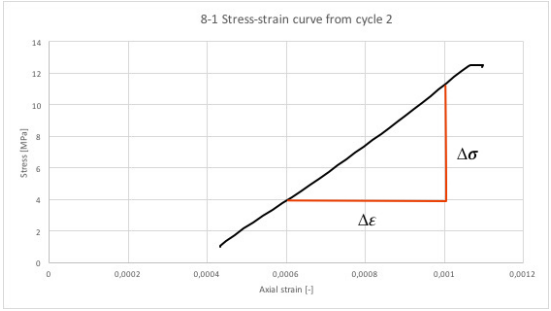

Figure 65: E modulus from stress-strain curve from cycle 2

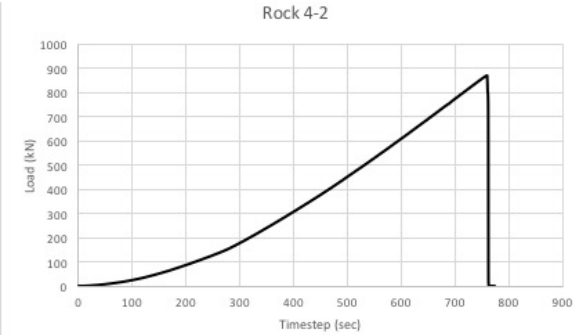

Figure 66: Load vs. time diagram for compressive test

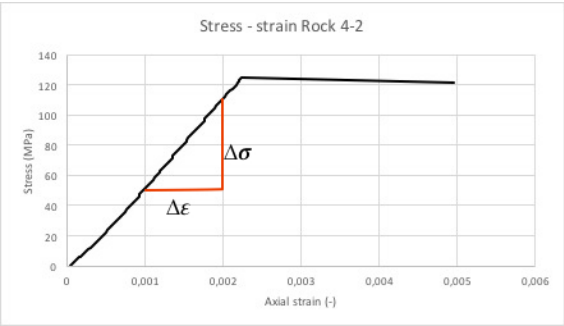

Figure 67: E modulus from stress-strain curve

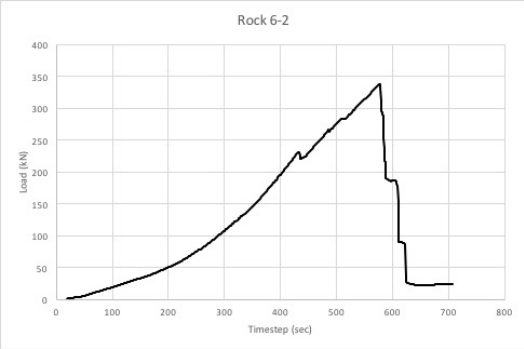

Figure 68: Load vs. time diagram for compressive test

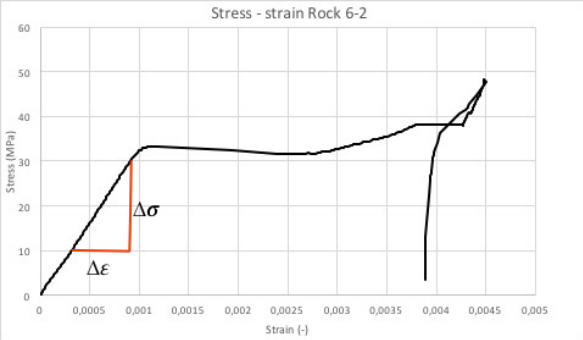

Figure 69: E modulus from stress-strain curve

Basic friction angle:

Table 27: Results from tilt test for basic friction angle

Sample		Concrete	Concrete	Rock
Number		5	8	
Height (mm)	*H*	50,00	50,00	47,00
Diameter (mm)	ϕ	94,00	94,00	94,00
On top	*Times*	Angle (deg.)	Angle (deg.)	Angle (deg.)
1	*1*	38	36,5	27
	2	36	32	32
	3	36,5	37	29
	4	35	35	29
	5	40	36	24
	6	36	34,5	28
2	*1*	37,5	39	28,5
	2	36,5	30	30
	3		38	29,5
	4		34,5	30,5
	5		37	25
	6		37,5	30
Average:		**36,9**	**35,6**	**28,5**
Average concrete:		**36,3**		

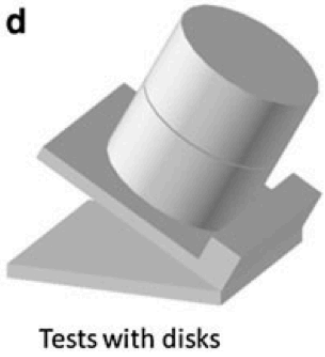

The basic friction angles were found by performing tilt tests on disks. The tests were performed according to the procedure for test with disks described by Alejano et al. (2012). The test was repeated six times with each disk on top. Sample 5 were cut skewed, and was therefore just tested with one side in top. This test was repeated eight times to obtain better accuracy.

Appendix B - Results from shear tests at LTU

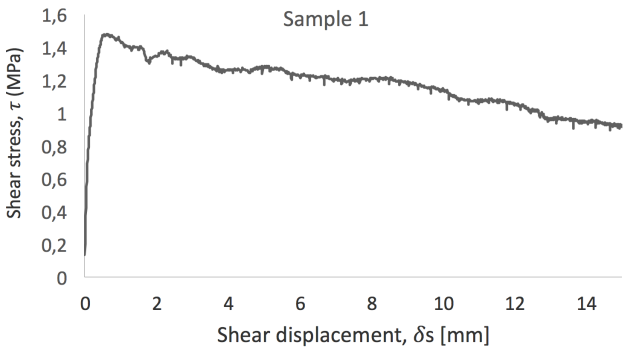

Figure 70: Shear stress vs shear displacement for Sample 1

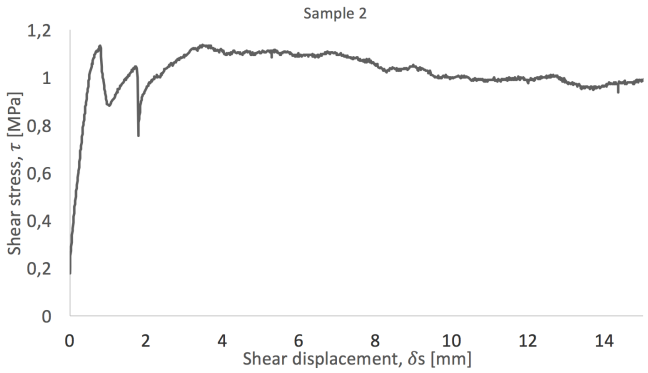

Figure 71: Shear stress vs shear displacement for Sample 2

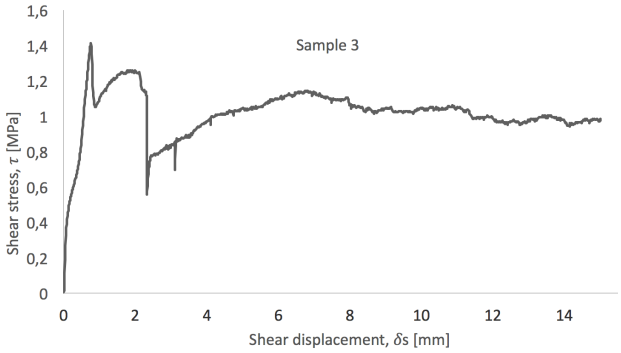

Figure 72: Shear stress vs shear displacement for Sample 3

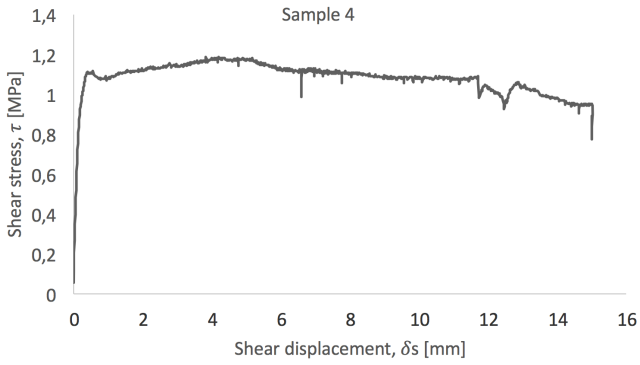

Figure 73: Shear stress vs shear displacement for Sample 4

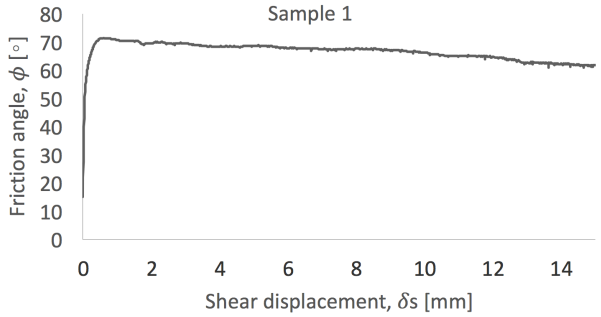

Figure 74: Friction angle vs shear displacement for Sample 1

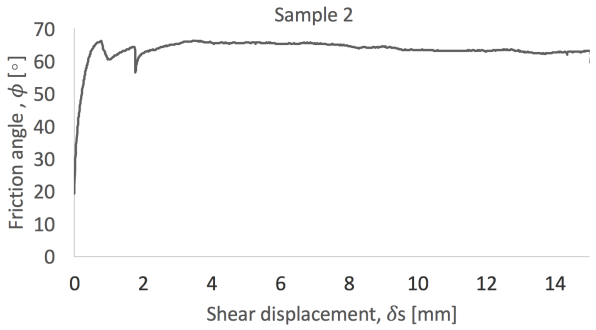

Figure 75: Friction angle vs shear displacement for Sample 2

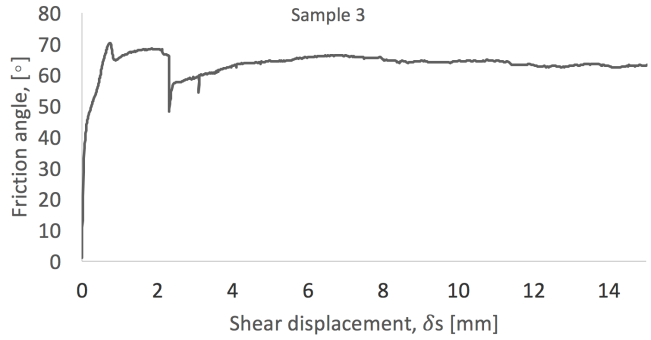

Figure 76: Friction angle vs shear displacement for Sample 3

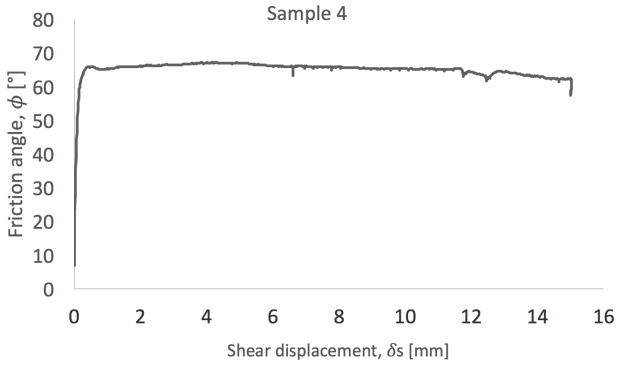

Figure 77: Friction angle vs shear displacement for Sample 4

Appendix C – Photos from shear tests at LTU

Figure 78: The interface of the samples was aligned horizontally

Figure 79: The rock and concrete were glued together to keep them mated when casting the samples

Figure 80: Casting the samples into forms

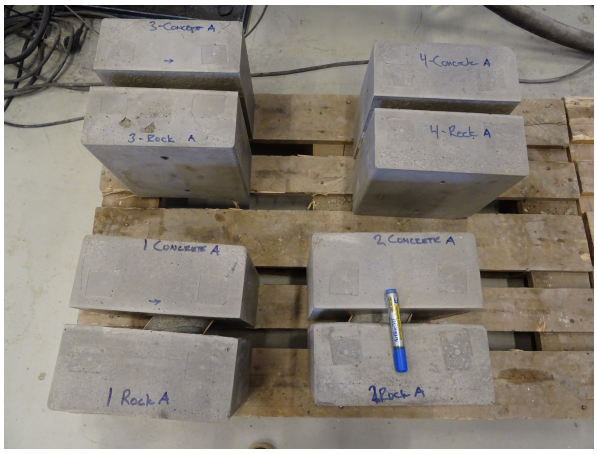

Figure 81: Samples ready for testing

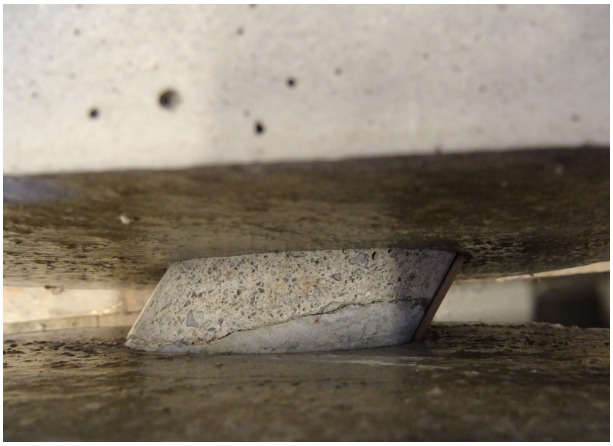

Figure 82: Sample 1 before shear test

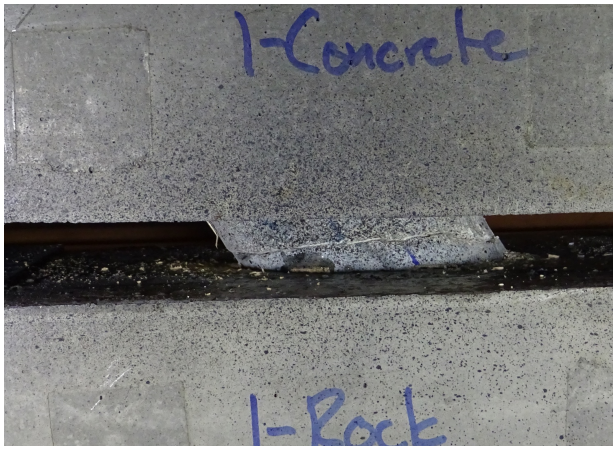

Figure 83: Other side of Sample 2, during shear testing

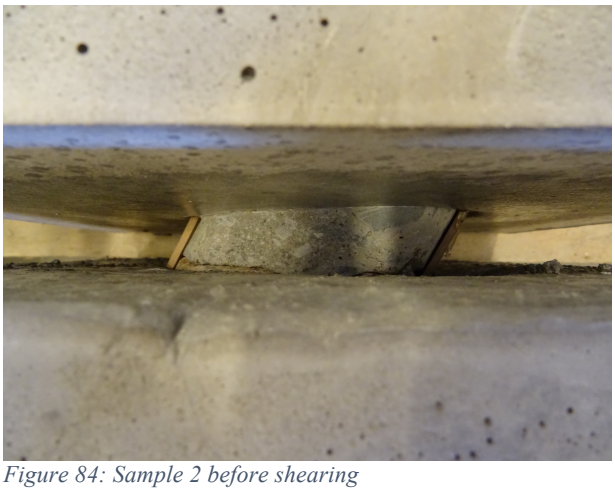

Figure 84: Sample 2 before shearing

Figure 85: Other side of Sample 2, during shear test

Figure 86: Sample 3 before shearing

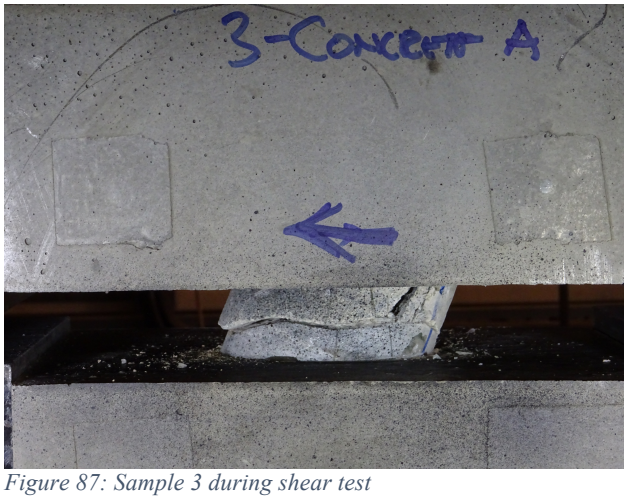

Figure 87: Sample 3 during shear test

Figure 88: Sample 4 before shearing

Figure 89: Other side of Sample 4, before shear test

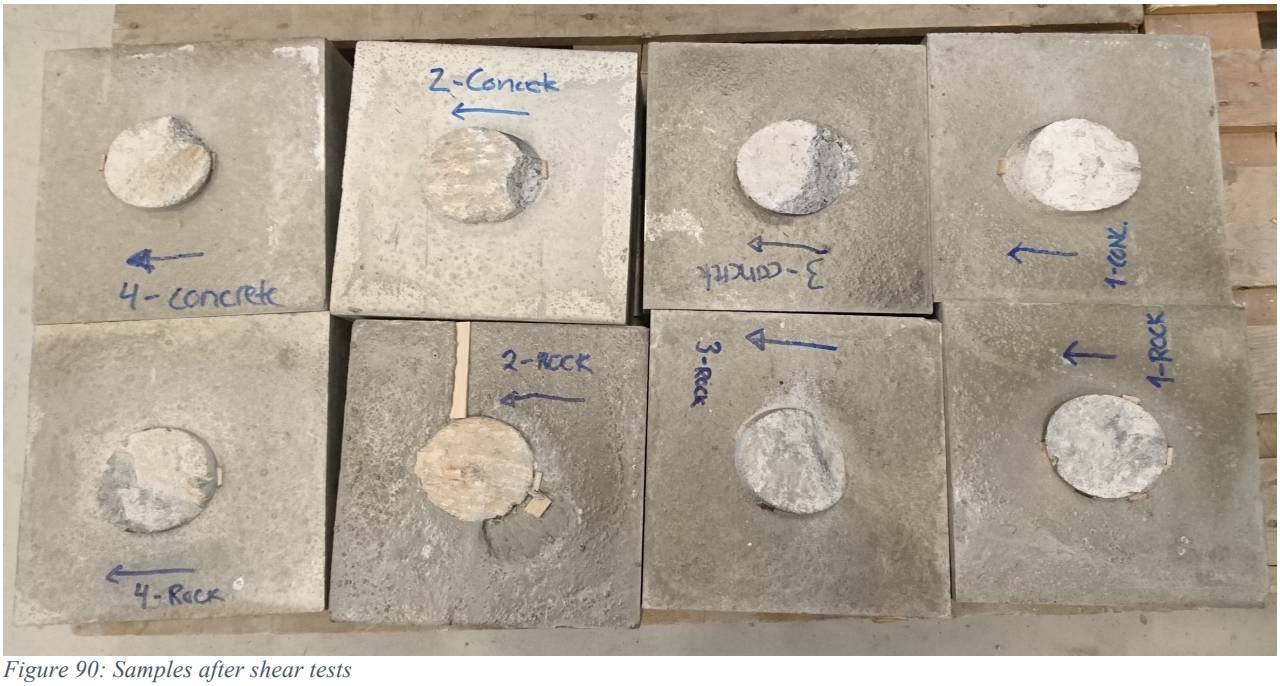

Figure 90: Samples after shear tests

Appendix D – Illustrations generated based on scanning´s of Kalhovd samples

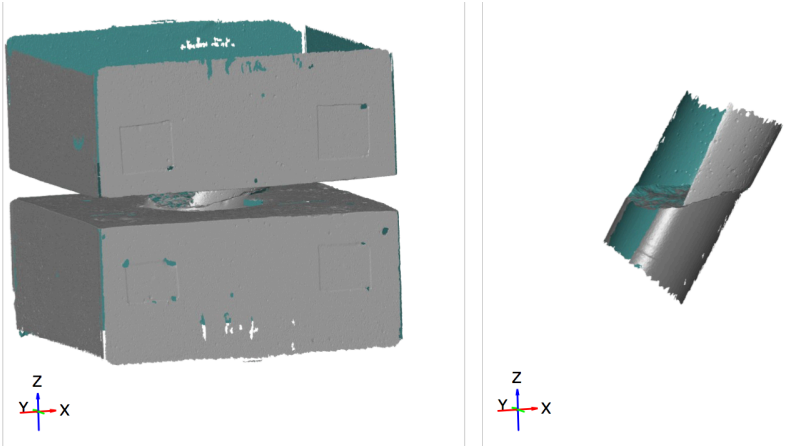

Figure 91: Sample 1 – coordinate system generated by Swerea Seacomp

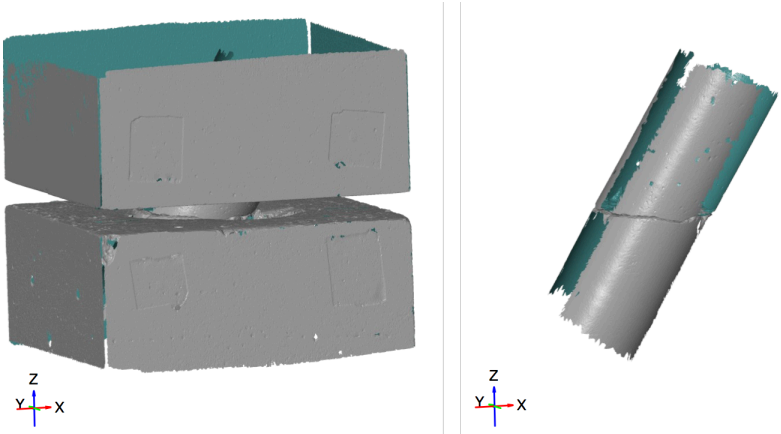

Figure 92: Sample 2 – coordinate system generated by Swerea Seacomp

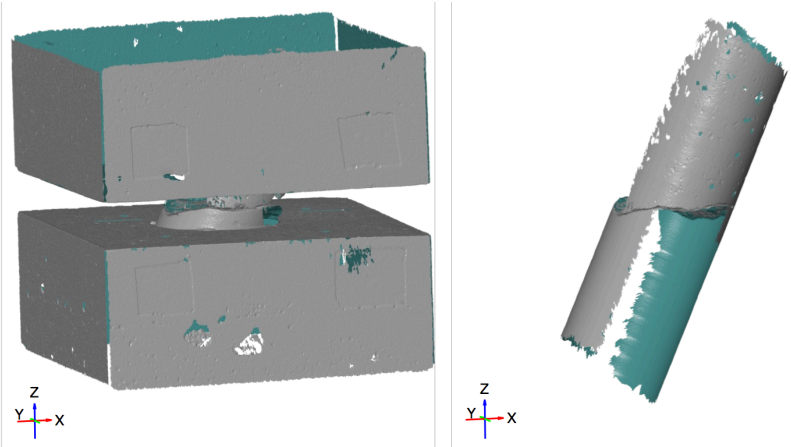

Figure 93: Sample 3 – coordinate system generated by Swerea Seacomp

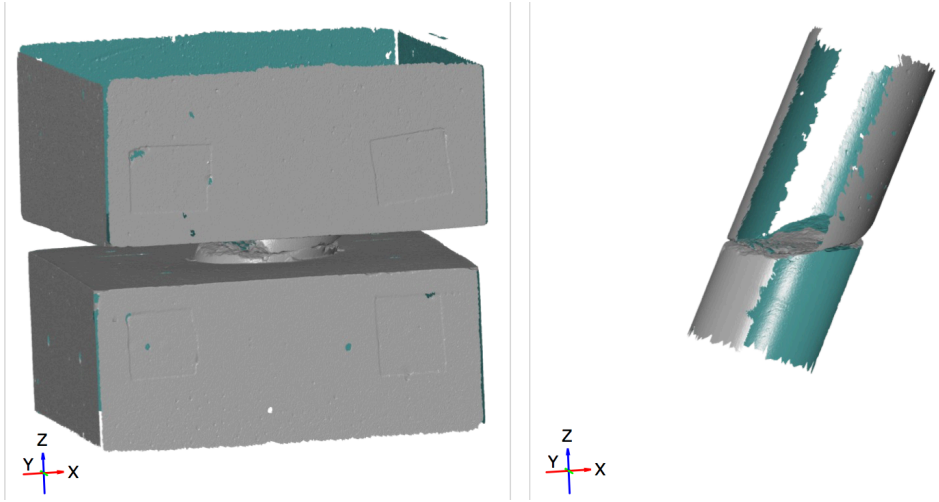

Figure 94: Sample 4 – coordinate system generated by Swerea Seacomp

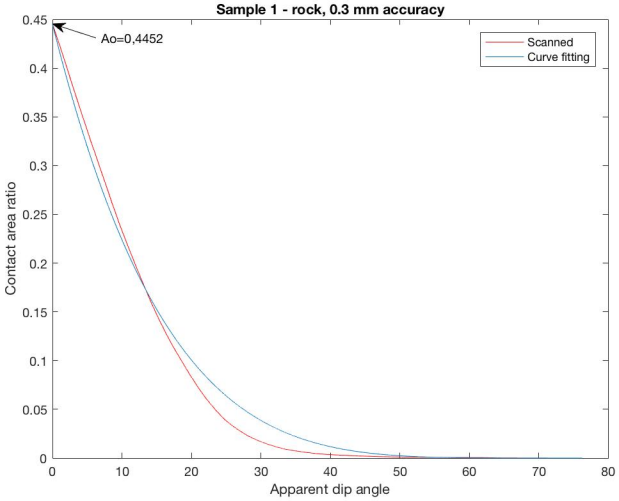

Figure 95: Apparent dip angle vs contact area ratio for Sample 1 - rock

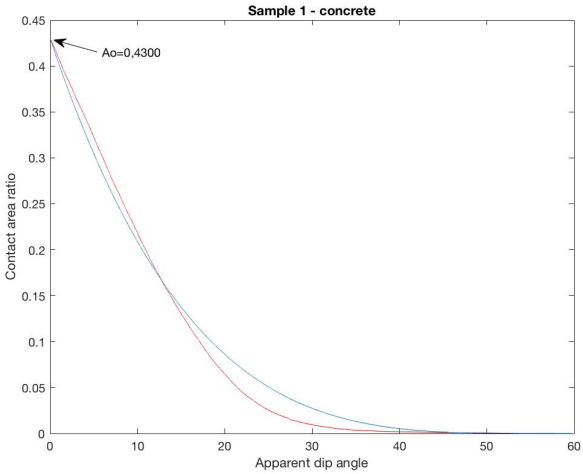

Figure 96: Apparent dip angle vs contact area ratio for Sample 1 - concrete

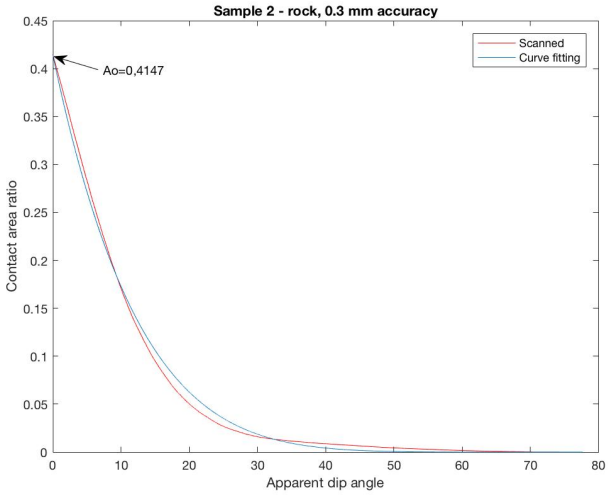

Figure 97: Apparent dip angle vs contact area ratio for Sample 2 - rock

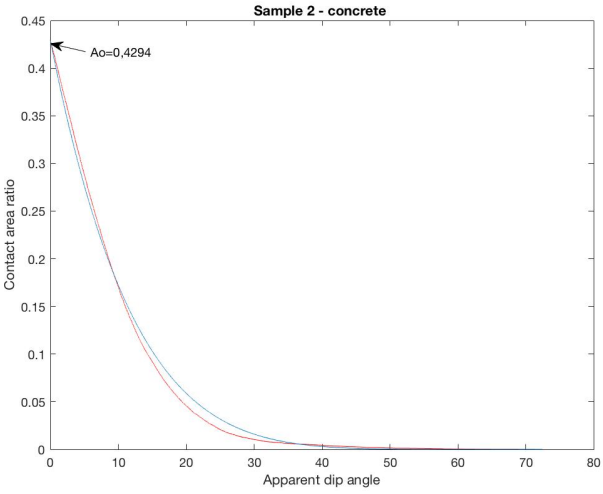

Figure 98: Apparent dip angle vs contact area ratio for Sample 2 - concrete

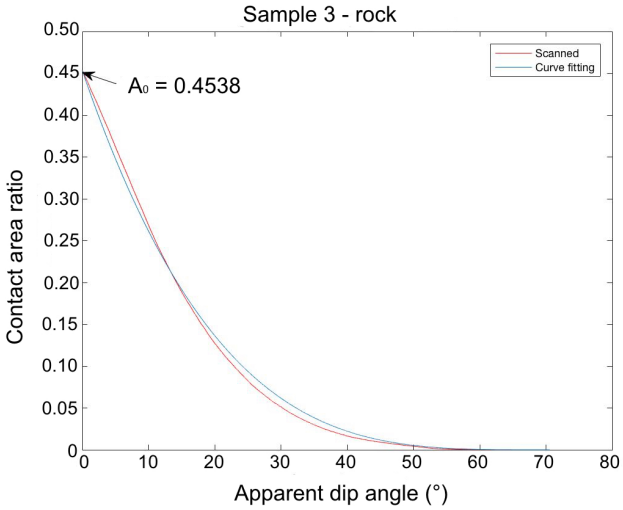

Figure 99: Apparent dip angle vs contact area ratio for Sample 3 - rock

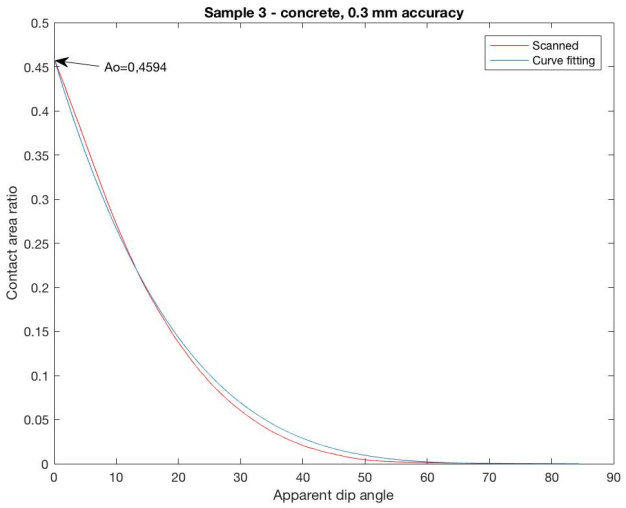

Figure 100: Apparent dip angle vs contact area ratio for Sample 3 - concrete

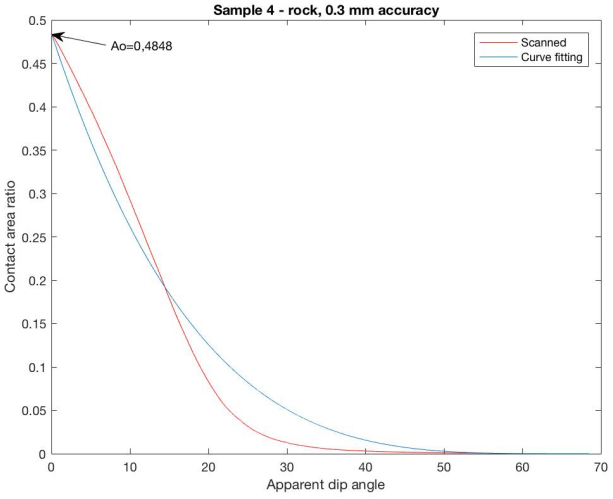

Figure 101: Apparent dip angle vs contact area ratio for Sample 4 - rock

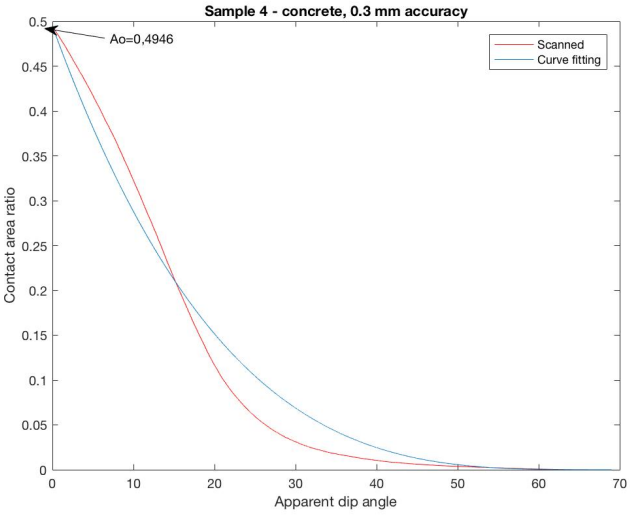

Figure 102: Apparent dip angle vs contact area ratio for Sample 4 - concrete

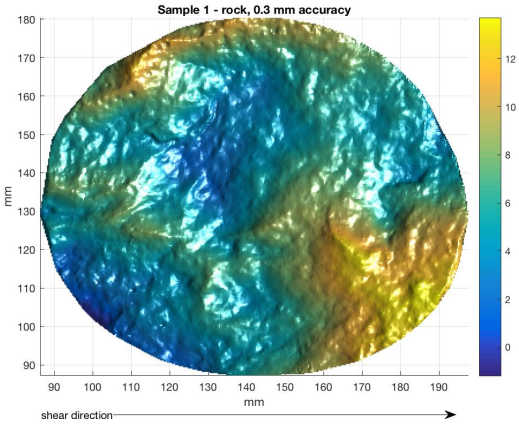

Figure 103: Sample 1-R: Regenerated surface from the data cloud

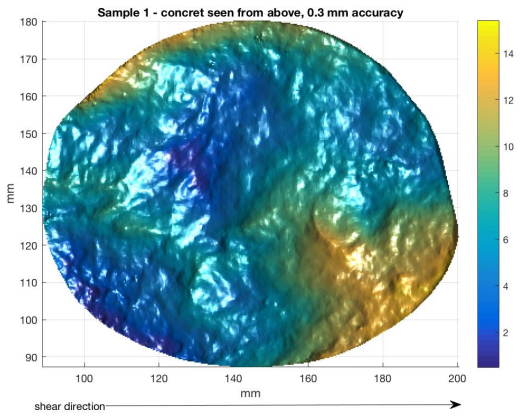

Figure 104: Sample 1-C: Regenerated surface from the data cloud

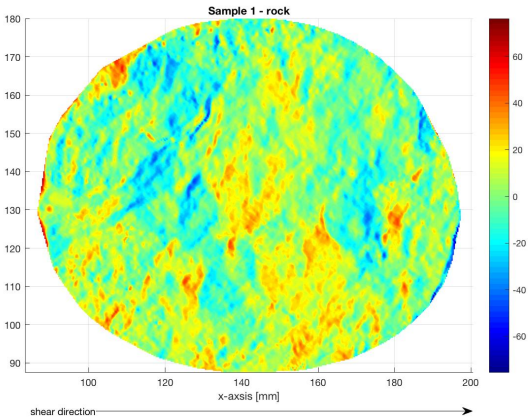

Figure 105: Sample 1-R: Measured apparent dip angles (degrees) against the shear direction

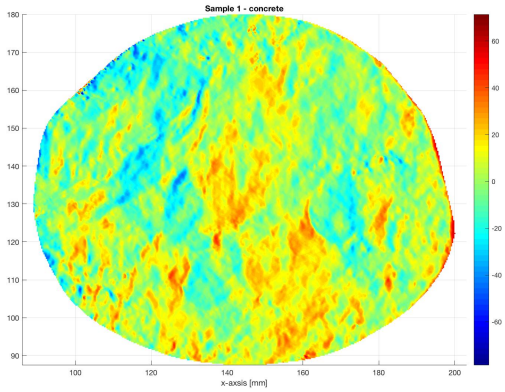

Figure 106: Sample 1-C: Measured apparent dip angles (degrees) against the shear direction

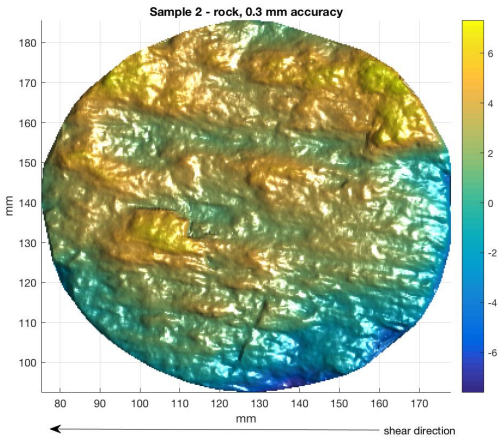

Figure 107: Sample 2-R: Regenerated surface from the data cloud

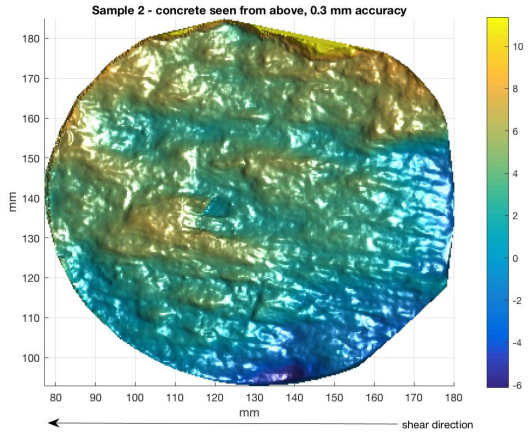

Figure 108: Sample 2-C: Regenerated surface from the data cloud

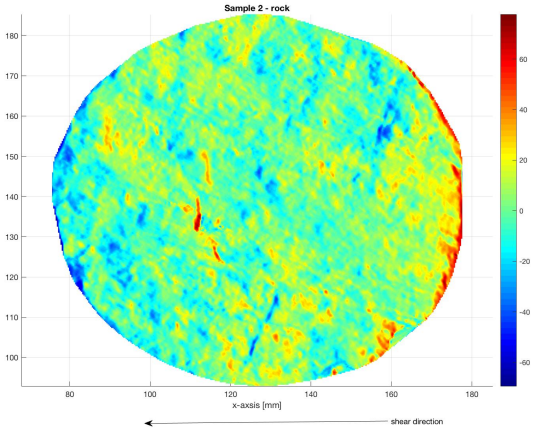

Figure 109: Sample 2-R: Measured apparent dip angles (degrees) against the shear direction

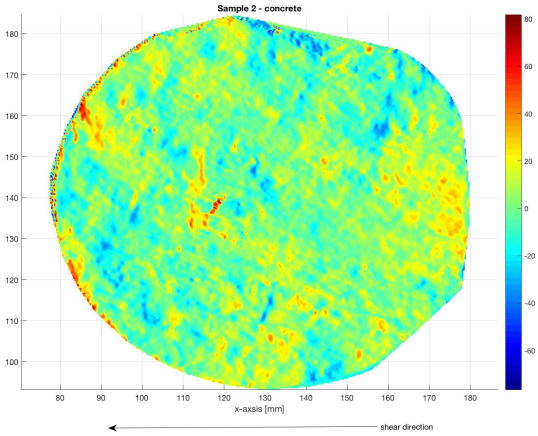

Figure 110: Sample 2-C: Measured apparent dip angles (degrees) against the shear direction

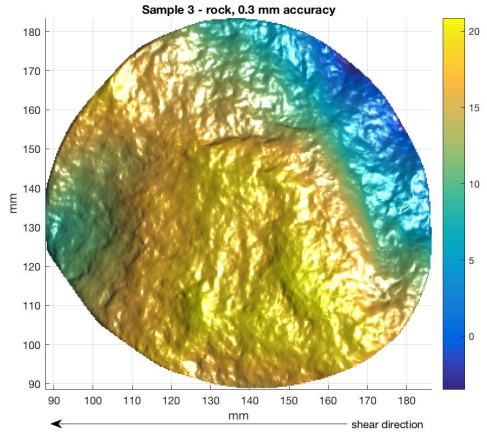

Figure 111: Sample 3-R: Regenerated surface from the data cloud

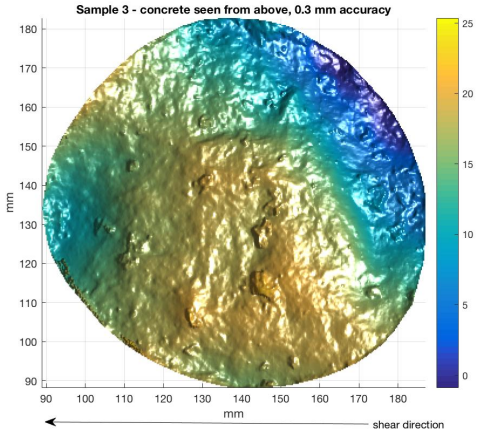

Figure 112: Sample 3-C: Regenerated surface from the data cloud

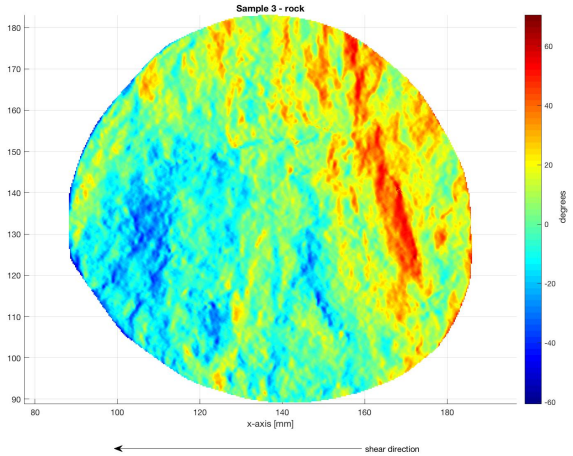

Figure 113: Sample 3-R: Measured apparent dip angles (degrees) against the shear direction

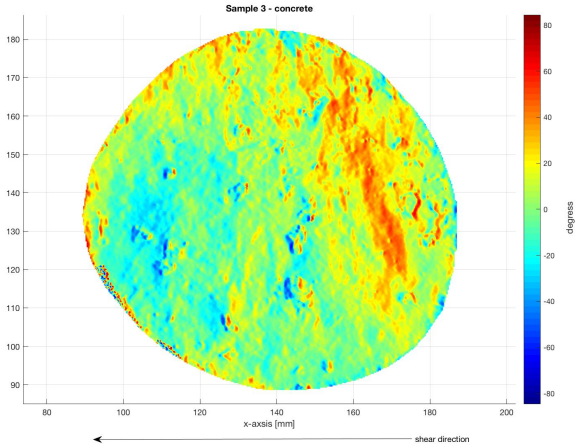

Figure 114: Sample 3-C: Measured apparent dip angles (degrees) against the shear direction

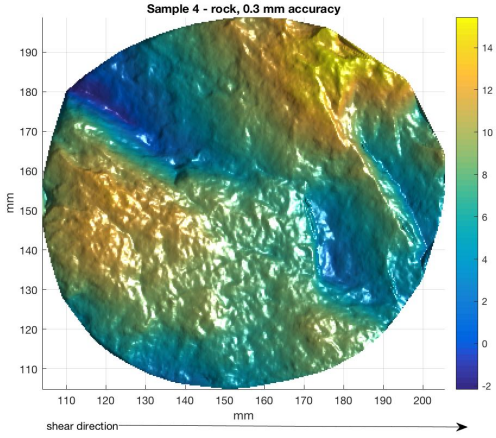

Figure 115: Sample 4-R: Regenerated surface from the data cloud

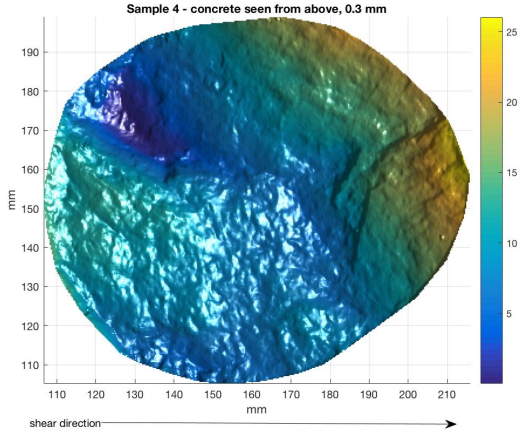

Figure 116: Sample 4-C: Regenerated surface from the data cloud

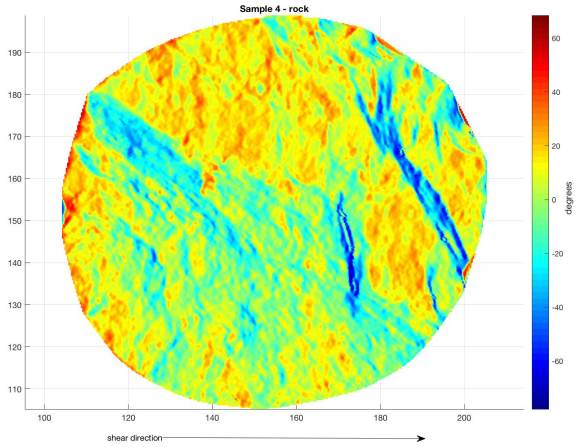

Figure 117: Sample 4-R: Measured apparent dip angles (degrees) against the shear direction

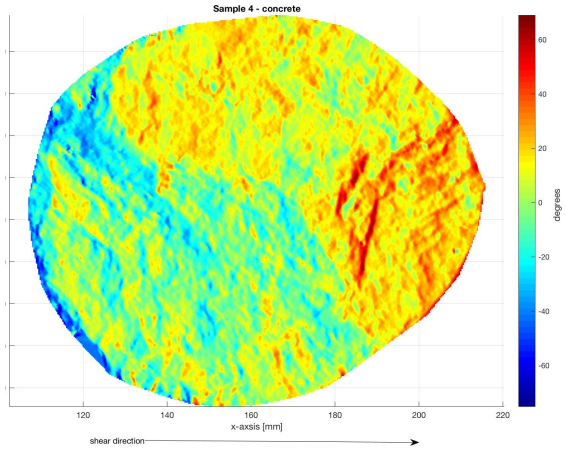

Figure 118: Sample 4-C: Measured apparent dip angles (degrees) against the shear direction

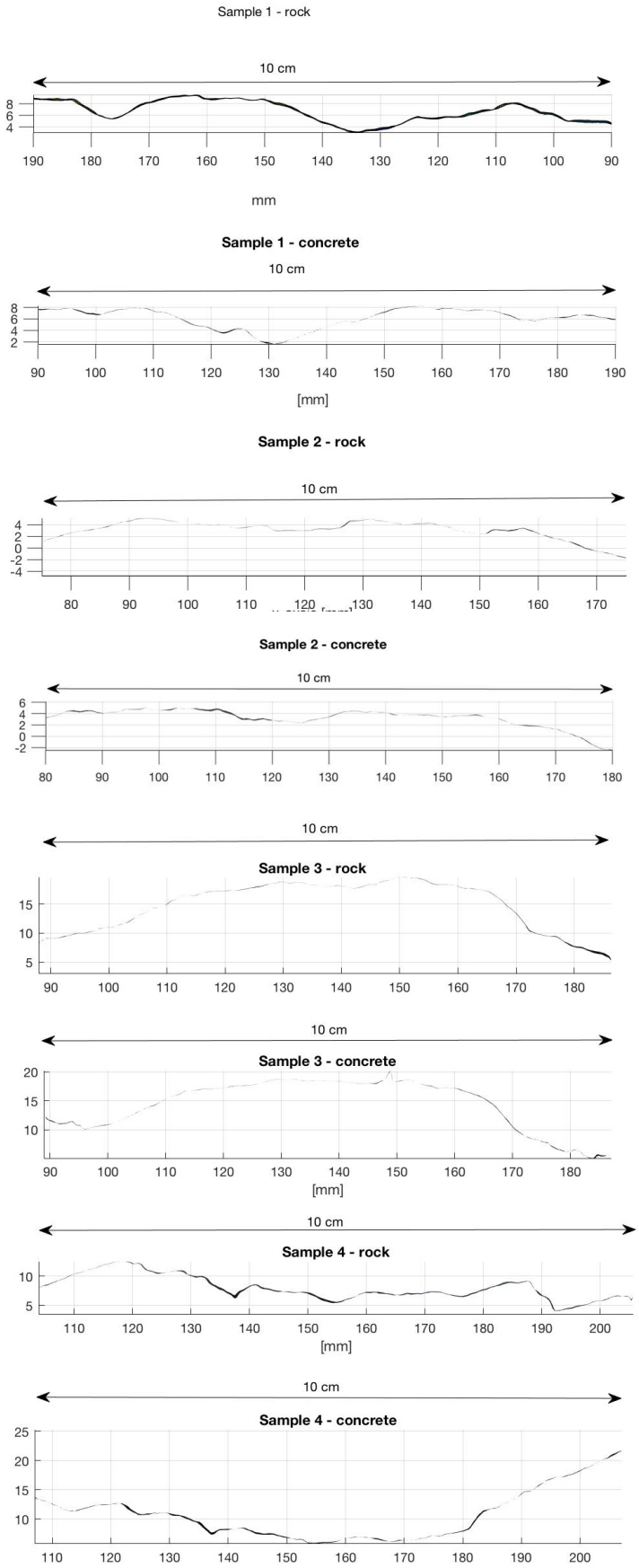

Figure 119: JRC profiles extracted from the regenerated surfaces

Appendix E – MATLAB code used to obtain 3D roughness parameters

Original MATLAB codes provided by Fredrik Johansson. The codes were adjusted to fit the data clouds from the scanning of Kalhovd samples.

Code used to plot the surfaces:

```
%Skapar rutnät för punkter
tx=-35:0.5:21;
ty=-25:0.5:31;

%Genererar x och y vektorer i rutnätet
[XI,YI]=meshgrid(tx,ty);

%Genererar höjdata efter angivet rutnät
ZI=griddata(X,Y,Z,XI,YI);
[Nx,Ny,Nz]=surfnorm(XI,YI,ZI);
t=[1 0 0];


%Plottar sprickytan
surf(XI,YI,ZI), hold;
%surf(Nx,Ny,Nz),hold
axis equal
view(2)
light
shading interp
```

Code used to obtain the parameters A_o and θ^*_{max}, and the input data for regression analysis to obtain C:

```
%Skapar rutnät för punkter
tx=-35:0.5:21;
ty=-25:0.5:31;

%Genererar x och y vektorer i rutnätet
[XI,YI]=meshgrid(tx,ty);

%Genererar höjdata efter angivet rutnät
ZI=griddata(X,Y,Z,XI,YI);
[Nx,Ny,Nz]=surfnorm(XI,YI,ZI);

%Skapar vektorer för normalen där Nx oxh Ny och Nz läggs i separata
%kolumner.
LL=length(tx)*length(ty)
LLL=(length(tx)-1)*(length(ty)-1)
Nxx=reshape(Nx,LL,1);
Nyy=reshape(Ny,LL,1);
Nzz=reshape(Nz,LL,1);
Ntot=[Nxx,Nyy,Nzz];

%Bestämmer potenitell kontaktarea.
t=[0 -1 0];                 %Vektor för skjuvriktning
%t=[-1 0 0];
A=Ntot*t';                    %Produkten ger vinkeln cos(90-fi) mellan vektor för
skjuvriktning och plan på asperity.
```

```
M=(mean(A));                    %Bestämmer medellutning av provet mot skjuvriktning.
Kontrollera om abs ska med!!!
B=A;%-M;                        %Korrigerar för medellutning.
C=find(B<0);                   %Lokaliserar alla positioner för element som lutar mot
skjuvriktning.
D=B(C,1);                     %Hittar lutningsvinkel för element i C och lägger dessa
i separat vektor.
G=ones(length(D),1)*1/LLL;   %Beräkningar area för varje element mot skjuvriktning
och lägger dessa i en vektor.
GG=cumsum(G);                 %Summerar cumulativt total area mot skjuvriktning.
U=90-acosd(D);                %Beräkningar vinkeln mellan skjuvvektor och plan för
aspertiy.
UU=abs(sort(U));           %Sorterar vinklarna efter storlek och tar absolutbeloppet
på dem (eftersom de var negativa)
plot(UU,GG,'r'),hold on     %Plottar potentiell kontaktarea.

WW=0;
W=0;
for s=1:length(UU)-1
W=0.533*((max(UU)-(UU(s,1)))/max(UU))^3.874;
WW=[WW,W];
end
plot(UU,WW);hold
%Denna del plottar lutningsvinklarna
H=90-acosd(A);
HH=reshape(H,1341,1341);
surf(XI,YI,HH),hold;
view(2)
axis equal
shading interp
```

Adjustments done in the codes:

1. The grid generated by *tx* and *ty* was changed for each sample, where *tx=min(X):0.3:max(X)* and ty=min(Y):0.3:max(Y). The minimum values were rounded down to the closest whole integer, while the maximum values were rounded up, as seen in Table 28.

Table 28: tx and ty values used to generate the grids

Sample	Max X	Min X	Max Y	Min Y	**tx**	**ty**
1-r	197.69	86.15	180.53	87.08	86:0.3:198	87:0.3:181
1-c	200.54	88.39	180.51	87.11	88:0.3:201	87:0.3:181
2-r	178.16	75.22	185.78	92.43	75:0.3:179	92:0.3:186
2-c	180.27	76.92	185.01	92.81	76:0.3:181	92:0.3:186
3-r	186.42	87.60	183.48	88.59	87:0.3:187	88:0.3:184
3-c	187.36	88.83	182.93	88.03	88:0.3:187	88:0.3:183
4-r	205.80	103.78	198.94	104.79	103:0.3:206	104:0.3:199
4-c	215.95	106.34	199.12	105.15	106:0.3:216	105:0.3:200

2. The shear direction vectors were changed to either [1 0 0] or [-1 0 0] depending on the how the x-axis was orientated on the sample compared to the shear direction. The scanned surfaces and its coordinate systems were compared with photos of the samples in the shear test machine to see if the shear direction was in the positive or negative direction along the x-axis. An example is given in Figure 120.

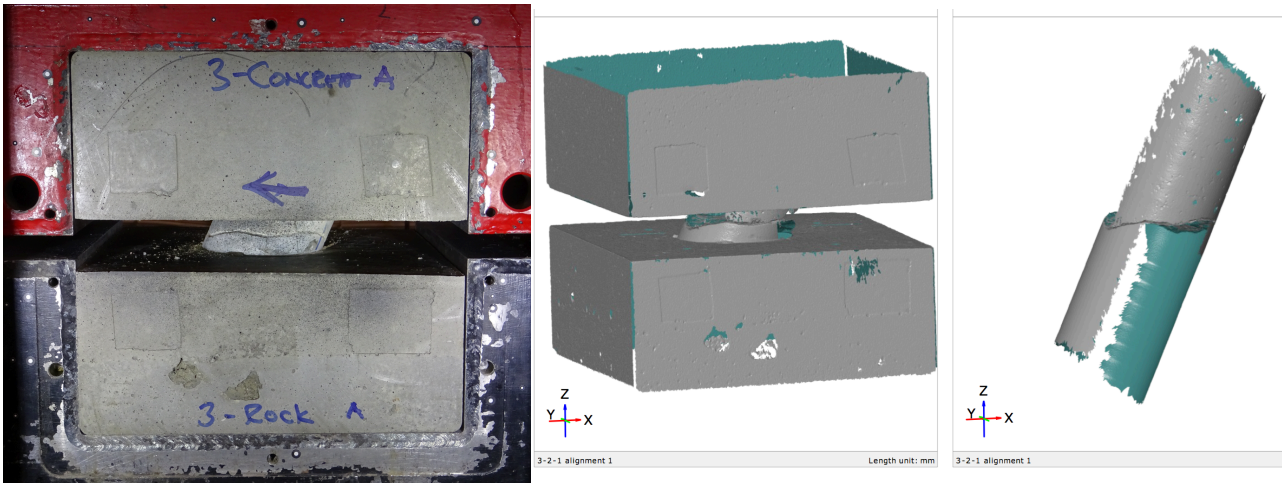

Figure 120: Shear direction in negative direction along the x-axis for Sample 3

Figure 120 shows that the shear direction is in negative direction along the x-axis, hence, **t**= [-1 0 0]. If the sample had been rotated 180 degrees around the z-axis before it was scanned, the shear direction would have been [1 0 0], since the shear direction would have been along the positive direction along the x-axis. Table 29 shows the shear direction vectors for all the samples.

Table 29: Shear direction vectors

Sample	Shear direction vector, **t**
1	[1 0 0]
2	[-1 0 0]
3	[-1 0 0]
4	[1 0 0]

3. When plotting the apparent dip angles against the shear direction, the size of the x-y grid must be changed for each sample, as the coordinate system is different for every sample. The size of the grid was found by looking at the size of the XI or YI vector in MATLAB, and then inserted in the reshape function.

Appendix F – Estimated shear strengths on Grasselli's samples

Table 30: Estimated shear strengths on Grasselli's samples

Sample	Rock type	β (°)	A_0 (-)	C (-)	θ^*_{max} (°)	ϕ_b (°)	σ_t *(MPa)*	σ_n *(MPa)*	Peak shear strength (*MPa*)			
									Measured	Grasselli	Xia	Johansson
C1	Limestone	0	0.491	7.03	80	36	2.4	1.07	2.20	1.9	2.1	1.8
C2	Limestone	0	0.462	5.64	80	36	2.4	1.07	2.10	2.2	2.2	2.1
C3	Limestone	0	0.460	4.60	57	36	2.4	3.72	5.50	5.5	5.3	4.2
C4	Limestone	0	0.508	4.74	65	36	2.4	2.45	4.60	4.1	4.4	3.5
C5	Limestone	0	0.495	5.26	74	36	2.4	3.11	5.00	5.2	5.4	4.1
C6	Limestone	0	0.546	5.19	68	36	2.4	1.02	2.10	2.1	2.7	2.0
C8	Limestone	0	0.555	5.71	74	36	2.4	3.11	4.90	4.9	5.8	4.1
G1	Granite	0	0.493	7.17	90	34	8.8	2.30	5.70	4.6	5.4	6.2
G2	Granite	0	0.498	5.60	80	34	8.8	2.30	5.60	5.1	6.3	7.1
G4	Granite	0	0.498	5.48	65	34	8.8	2.19	4.80	4.3	4.8	4.9
G5	Granite	0	0.460	5.33	57	34	8.8	1.12	2.40	2.3	2.2	2.4
G6	Granite	0	0.477	7.39	84	34	8.8	1.12	2.90	2.4	2.7	3.3
G7	Granite	0	0.470	7.15	81	34	8.8	1.12	2.80	2.4	2.6	3.2
G9	Granite	0	0.508	5.85	75	34	8.8	1.12	3.00	2.6	3.6	3.8
Gn3	Gneiss	90	0.492	8.11	65	36	9.5	2.65	2.40	3.1	4.4	4.4
Gn6	Gneiss	0	0.522	4.91	63	36	3.5	1.90	3.40	3.5	4.0	5.2
Gn9	Gneiss	90	0.488	8.12	63	36	9.5	3.52	4.00	3.9	5.4	5.4
Gn10	Gneiss	90	0.500	8.18	70	36	9.5	3.57	3.90	3.9	6.0	5.9
Gn11	Gneiss	90	0.432	10.28	74	36	9.5	3.52	4.30	3.9	4.7	5.1
Gn12	Gneiss	90	0.506	11.12	85	36	9.5	4.08	3.30	4.5	6.4	6.2
Gn13	Gneiss	90	0.503	9.17	74	36	9.5	2.60	3.50	3.1	4.5	4.5
M1	Marble	0	0.513	9.64	76	37	9.2	0.87	1.70	1.8	1.8	1.7
M2	Marble	0	0.492	5.60	39	37	9.2	1.73	2.30	3.2	2.7	2.7
M3	Marble	0	0.471	10.50	65	37	9.2	0.87	1.20	1.7	1.3	1.3
M4	Marble	0	0.513	8.12	61	37	9.2	3.78	5.80	6.3	6.1	5.0
M5	Marble	0	0.533	8.92	59	37	9.2	2.60	4.40	4.6	4.3	3.5
M6	Marble	0	0.450	10.18	68	37	9.2	2.60	4.30	4.4	3.7	3.4
M7	Marble	0	0.502	13.33	86	37	9.2	3.78	5.60	6.1	5.6	4.7
M8	Marble	0	0.459	10.52	72	37	9.2	3.83	6.40	6.1	5.4	4.8
M9	Marble	0	0.494	10.36	59	37	9.2	2.60	4.50	4.4	3.7	3.2
M10	Marble	0	0.515	10.79	67	37	9.2	0.87	1.50	1.7	1.5	1.4
M12	Marble	0	0.429	7.28	55	37	9.2	1.79	3.00	3.3	2.7	2.6
ML1	Sandstone	0	0.573	7.25	66	37	0.7	1.02	1.40	1.3	1.6	1.3
ML2	Sandstone	0	0.505	5.44	45	37	0.7	4.13	4.50	4.8	5.1	3.3
ML3	Sandstone	0	0.523	7.81	66	37	0.7	2.09	2.30	2.5	2.8	2.0
S1	Serpentine	0	0.504	4.80	79	39	6.0	1.94	4.30	5.8	8.3	13.7
S2	Serpentine	0	0.466	4.44	75	39	6.0	0.97	3.40	3.5	5.4	14.0
Average estimation error (%)										11.2	20.3	35.2
Average estimation error if not considering the samples with β=90. (%)										10.5	14.4	32.2

Appendix G – Construction drawings from Kalhovd dam

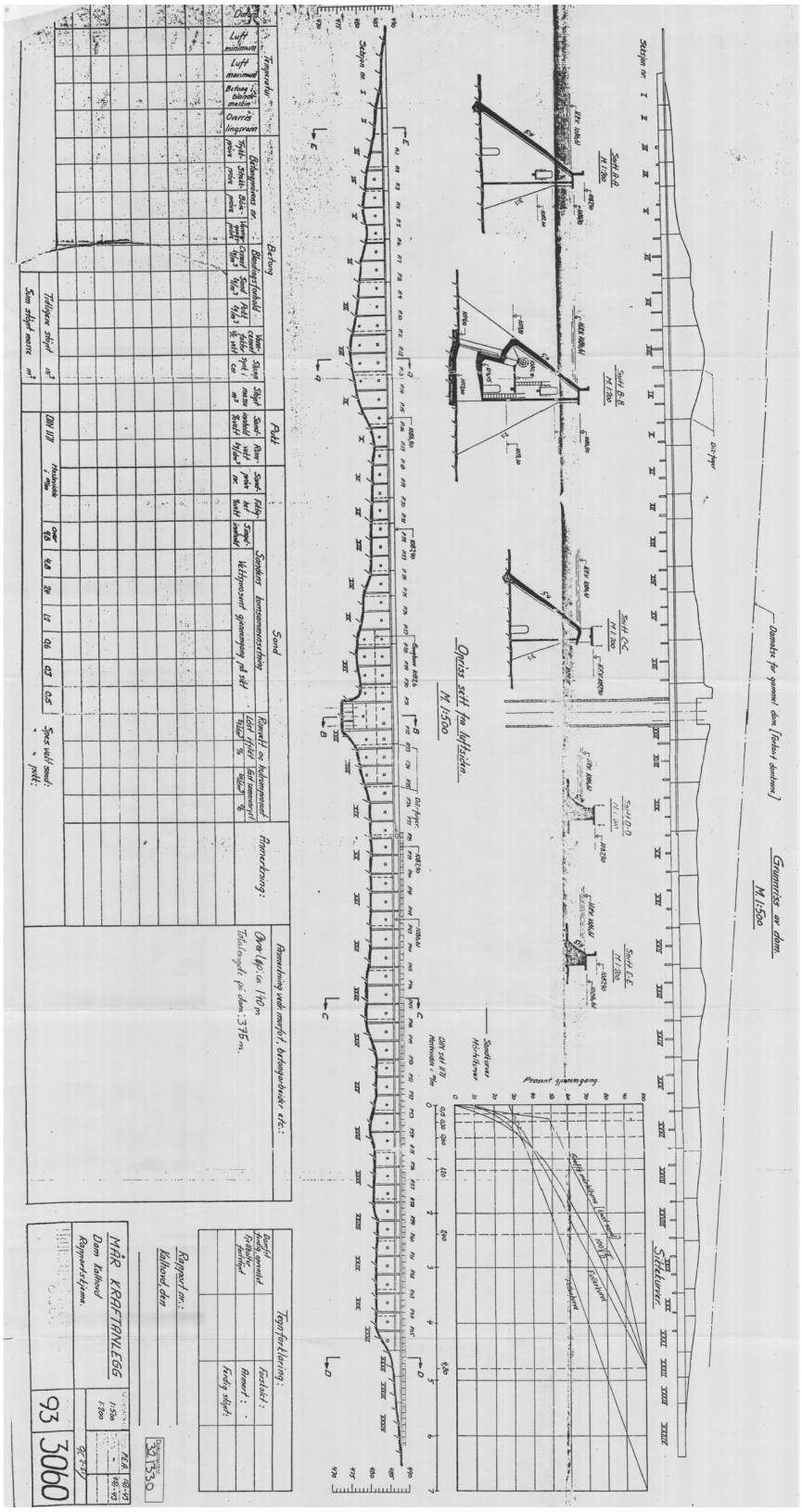

Figure 121: Kalhovd dam – overview, plan and cross sections. Buttress 1 to 65 from left to right, seen from downstream

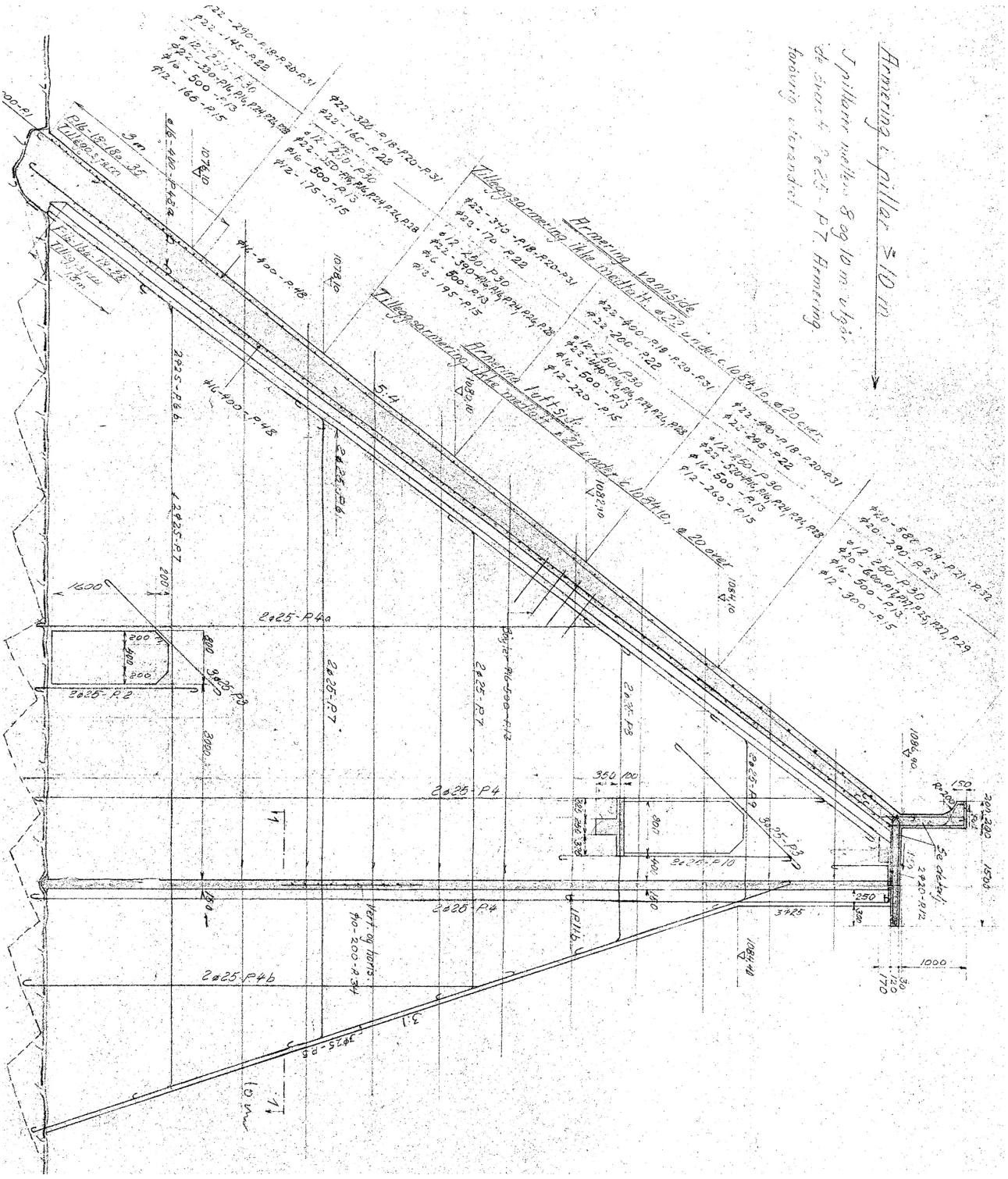

Figure 122: General cross sections of buttress without free spillway at dam Kalhovd

Appendix H – Calculations from sliding stability analysis

METHOD 1: FEM + shear tests

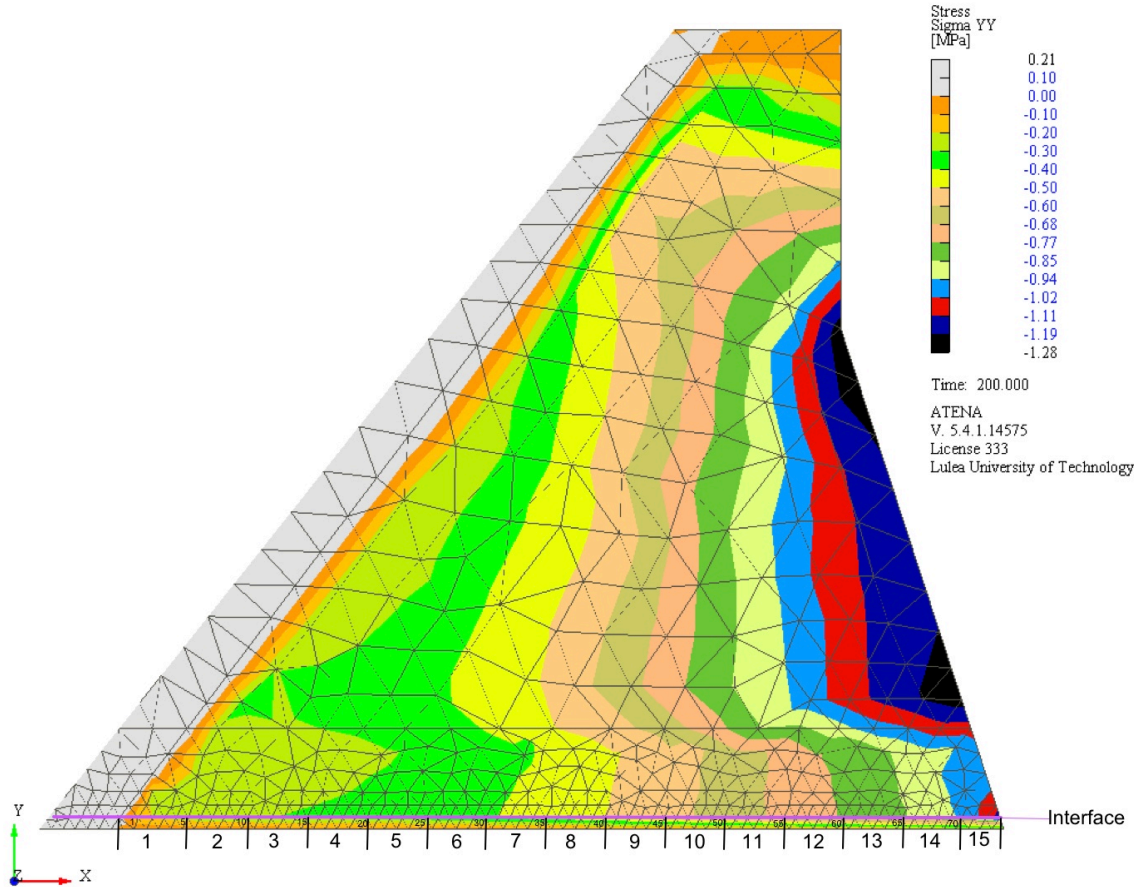

Figure 123: The interface exposed for compressive stress consist of 73 triangles/steps with a length of approximately 0.1 m. The interface was divided into 15 sections a length of approximately 0.5 m each.

Table 31: Calculations of horizontal stabilizing forces in the interface

		(MPa)			(m)	(m2)	(kN)		
Section	Step a to b	Normal stress a	Normal stress b	Ave. normal stress	Length section	Area section	V force	coeff. Friction	tan(phi)*Fv
1	0-5	0	0,227	0,1135	0,55	0,24365	27,654275	2,79595	77,3199702
2	5-10	0,227	0,272	0,2495	0,5	0,2215	55,26425	2,75515	152,261298
3	10-15	0,272	0,3135	0,29275	0,5	0,2215	64,844125	2,742175	177,813938
4	15-20	0,3135	0,341	0,32725	0,5	0,2215	72,485875	2,731825	198,018725
5	20-25	0,341	0,3685	0,35475	0,5	0,2215	78,577125	2,723575	214,010693
6	25-30	0,3685	0,396	0,38225	0,5	0,2215	84,668375	2,715325	229,902155
7	30-35	0,396	0,444	0,42	0,5	0,2215	93,03	2,704	251,55312
8	35-40	0,444	0,499	0,4715	0,5	0,2215	104,43725	2,68855	280,784768
9	40-45	0,499	0,5655	0,53225	0,5	0,2215	117,893375	2,670325	314,813627
10	45-50	0,5655	0,632	0,59875	0,5	0,2215	132,623125	2,650375	351,501015
11	50-55	0,632	0,7002	0,6661	0,5	0,2215	147,54115	2,63017	388,058306
1	55-60	0,7002	0,7752	0,7377	0,5	0,2215	163,40055	2,60869	426,261381
13	60-65	0,7752	0,843	0,8091	0,5	0,2215	179,21565	2,58727	463,679275
14	65-70	0,843	0,955	0,899	0,5	0,2215	199,1285	2,5603	509,828699
15	70-73	0,955	1,445	1,2	0,35	0,15505	186,06	2,47	459,5682
	SUM:				**7,4**				4495,37517 kN

Table 32: Calculations of horizontal driving forces

Load				
Ice load		100 kN/m*5 m		500 kN
Horizontal water pressure		10 kN/m3*(6,39 m)^2 *0,5*5m		1020,8 KN
Sum horizontal:				1520,8 kN

Calculation of the factor of safety for buttress number 8:

$$FS = \frac{\sum V'_{section} \cdot \tan \phi_{,section}}{\sum H} = \frac{4495.4\ kN}{1520.8\ kN} = \mathbf{2.96}$$

METHOD 2 and 3 – NVE:

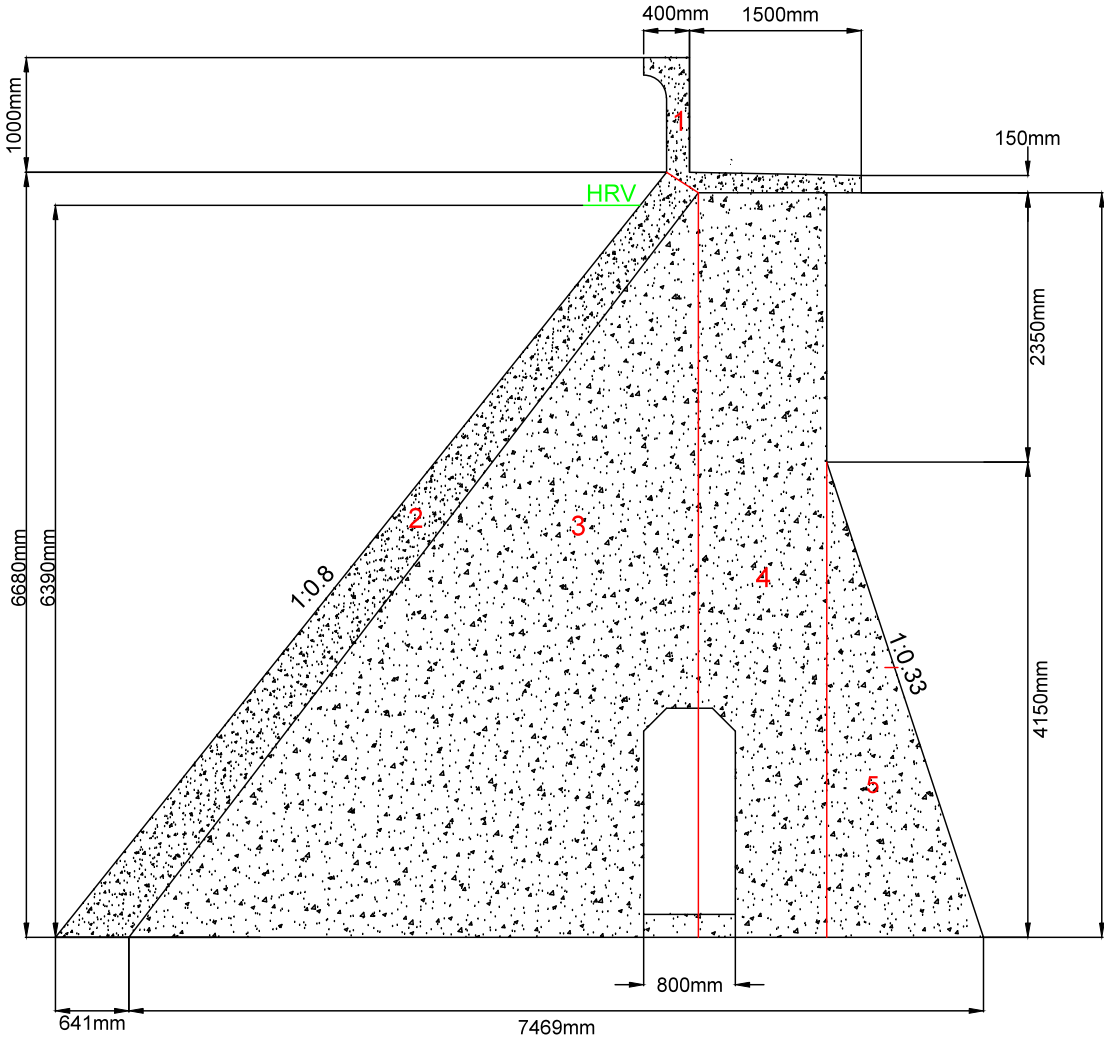

Figure 124: Division of sections used to calculate the self-load from the dam

Table 33: Sliding stability calculations, NVE method

Self-weight water	10 kN/m3			
Self-weight concrete	24,5 kN/m3			
Ice load	100 kN/m			
ϕ,shear test	69°			
ϕ,NVE	50°			
Water depth at HRV	6,39 m			
Horizontal loads		Calculation		Load (kN)
Horizontal water pressure		10 kN/m^3*(6,39 m)^2*0,5*5 m		1020,8
Ice load		100 kN/m*5 m		500
Sum horizontal:				1520,8
Vertical loads		Calculation		Load (kN)
Vertical water pressure		10 kN*(6,39m)^2*0,8*0,5*5m		816,64
Uplift		10 kN/m3*6,39 m*0,64 m* 5 m		-204,48
Self load 1 (walkway):		24,5 kN/m3*(0,15*1,7+0,2*0,6+0,4*0,4-0,25*0,2^2*pi)m2*5m		61,69
Self load 2 (flat slab):		24,5 kN/m3*(((6,68m)^2-(0,8*6,68m)^2)^0,5*(0,3m+0,03*6,68m/2)*5 m		419,38
Self load 3 (buttress)		25,5 kN/m3*(6,68 m)^2*0,8*0,5*(0,3 m +0,022 m*6,5/2)		324,91
Self load 4 (buttress)		24,5 kN/m3*1,2 m*6,5m*(0,3 m + 0,022 m*6,5/2)		70,99
Self load 5 (buttress)		24,5 kN/m3*(4,15m)^2*0,33*0,5*(0,3 m + 0,022 m*(2,35+(4,15/2))		27,66
Door opening		24,5 kN/m3*(0,8 m*1,8m-0,2m*0,2m)*(0,3 m + 0,022 m*(4,5 m+(1,8m/2))		-14,36
Sum vertical:				1502,43
∑V*tanϕ,NVE		1502,43 kN*tan(50°)		1790,53
∑V*tanϕ,test		1502,43 kN*tan(69°)		3913,96
Factor of safety, NVE		1790,53 kN/1520,8 kN		**1,18**
Factor of safety,test		3913,96 kN/1520,8 kN		2,57